NASA TECHNICAL MEMORANDUM

NASA TM X-72672

COPY NO.

NASA TM X- 72672

(NASA-TM-X-72672) AN OPERATIONAL SATELLITE SCATTEROMETER FOR WIND VECTOR MEASUREMENTS OVER THE OCEAN (NASA) 169 p HC $6.25

N75-25400

CSCL 14B

Unclas

G3/47 24204

AN OPERATIONAL SATELLITE SCATTEROMETER
FOR
WIND VECTOR MEASUREMENTS OVER THE OCEAN

W. L. Grantham
E. M. Bracalente
W. L. Jones
J. H. Schrader
L. C. Schroeder
J. L. Mitchell*

* LTV Aerospace Corp.

NATIONAL AERONAUTICS AND SPACE ADMINISTRATION
LANGLEY RESEARCH CENTER, HAMPTON, VIRGINIA 23665

1. Report No. NASA TMX 72672	2. Government Accession No.	3. Recipient's Catalog No.

4. Title and Subtitle An Operational Satellite Scatterometer for Wind Vector Measurements Over the Ocean	5. Report Date March 18, 1975 6. Performing Organization Code
7. Author(s) W. L. Grantham, E. M. Bracalente, W. L Jones, J. H. Schrader, L. J. Schroeder, J. L. Mitchell* *LTV Aerospace Corporation	8. Performing Organization Report No. NASA TMX-72672
9. Performing Organization Name and Address NASA Langley Research Center Hampton, Virginia 23665	10. Work Unit No. 11. Contract or Grant No.
12. Sponsoring Agency Name and Address NASA Langley Research Center Hampton, Virginia 23665	13. Type of Report and Period Covered Topical 14. Sponsoring Agency Code 161-05-07-01

15. Supplementary Notes

16. Abstract

This document describes performance requirements and design characteristics of a microwave scatterometer wind sensor for measuring surface winds over the oceans on a global basis. The wind sensor will be used on the SeaSat-A satellite along with several other oceanographic remote sensors. The scatterometer specifications are developed from User requirements of wind vector measurement range and accuracy, swath width, resolution cell size and measurement grid spacing. A detailed analysis is performed for a baseline fan-beam scatterometer design, and its performance capabilities for meeting the SeaSat-A User requirements. Various modes of operation are discussed which will allow the resolution of questions concerning the effects of sea state on the scatterometer wind sensing ability and to verify design boundaries of the instrument.

17. Key Words (Suggested by Author(s)) (STAR category underlined) Microwave Scatterometer Ocean Wind Vector SeaSat-A Remote Sensing Meteorology Oceanography	18. Distribution Statement Unclassified - Unlimited

19. Security Classif. (of this report) Unclassified	20. Security Classif. (of this page) Unclassified	21. No. of Pages 169	22. Price* $6.25

*Available from { The National Technical Information Service, Springfield, Virginia 22151
STIF/NASA Scientific and Technical Information Facility, P.O. Box 33, College Park, MD 20740

SCATTEROMETER REPORT OUTLINE

TITLE

AUTHORS

SUMMARY

INTRODUCTION

SYMBOLS

HISTORY AND BACKGROUND

PERFORMANCE REQUIREMENTS

A FAN BEAM SCATTEROMETER DESIGN
    Mode I
    Mode II
    Earth Rotational Effects
HARDWARE SYSTEM DESCRIPTION

CONCLUDING REMARKS

APPENDICES

REFERENCES

TABLES

FIGURES

SUMMARY

This document describes performance requirements and design characteristics of a microwave scatterometer wind sensor for measuring surface winds over the oceans on a global basis. A review of microwave scatterometer aircraft and satellite measurements on the ocean is included, showing the sensitivity of this instrument as a remote wind sensor. This wind sensor will be used on the SeaSat A satellite along with several other remote sensors: a radar altimeter, an imaging radar, and an optical radiometer. Together, this complement of instruments will provide the SeaSat A User community with scientific and operational type data in the areas of oceanography, meteorology and geodesy.

The scatterometer specifications are developed from User requirements of wind vector measurement range and accuracy, swath width, resolution cell size and measurement grid spacing. The manner of transforming wind speed accuracy into instrument accuracy requirements is described in detail. Since the scatterometer is sensitive to both wind direction and wind speed, special techniques are developed to determine both parameters.

From several options available, the fan beam scatterometer design has been chosen by the SeaSat study teams as the one most suitable when considering attitude control, spacecraft interface problems, and performance characteristics. A detailed analysis is performed for a baseline scatterometer design. The analysis includes derivation of the instrument design and its performance capabilities for meeting the SeaSat A User requirements. Various modes of operation are discussed which will allow the resolution of questions concerning the effects of sea state on the scatterometer wind sensing ability and to verify design boundaries of the instrument.

INTRODUCTION

Global measurement of ocean winds has been established by the SeaSat A User panel as one requirement of the oceanographic satellite program. Surface winds are required as inputs to wave forecast models and can also be helpful in weather forecasting. The lack of sufficient wind and pressure data over the oceans has thus far precluded better long range weather forecasting for continental areas.

The remote sensor selected for this surface wind measurement is the microwave scatterometer. Aircraft and satellite scatterometer data show that, for windspeeds less than 20 m/sec and incidence angles beyond 25°, the ocean radar scattering coefficient (σ^o) changes about one-half dB per 10 log m/sec change in wind speed. While some authors argue whether the rate is 1/2 or 1/4 dB/10 log m/sec, the sensitivity of σ^o to wind speed is still sufficient (even to gale-force winds) to make the scatterometer a viable remote sensor of wind speed and direction if proper attention is given to instrument accuracy.

During the SeaSat Phase A feasibility studies, several instrument designs were considered so that the payload could be optimally configured. The total instrument complement included not only a scatterometer but a radar altimeter, an imaging radar, and both optical and microwave radiometers.

As scatterometer sponsor, Langley submitted to the study teams several candidate designs for the scatterometer which would satisfy the requirements set forth by the User panel (ref. 1). During the August 1973-August 1974 time period the Phase B Study Team, User Working Group and Instrument Working Group considered these options, their inpact on the spacecraft configuration, and their effect on User requirements. From this effort came the final recommended payload design which included the fan beam concept for the scatterometer.

The scatterometer characteristics developed in this report are based on User requirements established by the SeaSat User Working Group (ref. 1). In an effort to obtain further insight, a specific scatterometer design with supporting analysis is presented. Certain design options using the fan beam concept are pointed out such as a high resolution mode for areas where strong wind speed gradients exist.

SYMBOLS

A	arbitrary constant
A_c	ground area of doppler cell, km^2
B_c	doppler bandwidth across doppler cell, Hz
C	speed of light, 2.998×10^8 m/s
C_n	element excitation distribution
d	horn spacing
D	variable controlled by wind speed
$E(\Phi)$	electric field intensity
f_D	doppler shift at center of doppler cell, Hz
f_t	transmitter frequency, GHz
F	receiver preamplifier noise figure
$F(\Phi)$	element pattern
G	gain of antenna to center of doppler cell
G_o	peak antenna gain
$H(f)$	transfer function of a gated mean integrator
k	wave number of ocean
K	Boltzman's constant 1.38×10^{-23} $j/^oK$
K_P	ratio of standard deviation (σ_M) of σ^o measurement to true value of σ^o
K_{pa}	normalized standard deviation after averaging measurements from multiple data cells
K_t	ratio of noise integration period to signal plus noise integration period
l_c	distance on Earth's surface from center to center of adjacent doppler cells along the antenna beam, km

L	length of doppler cell base, km
L_s	miscellaneous system loss (2 way)
L_R	receiver loss
m	integer 0, ±1, ±2
n	integer
N	receiver noise power, watts
N_{el}	number of antenna elements
No_A	number of antennas used to make measurements
No_P	number of polarizations used per antenna
P_D	power spectral density of a random signal in bandwidth B_c (one sided)
P_d	power density of the transmitted signal at the surface of the earth
$\hat{P}_N$	estimate of the mean noise power
P_R	true value of return signal power, watts
$\hat{P}_{SN}$	estimate of the mean signal plus noise power
$\hat{P}_R$	estimate of return signal power, watts
P_T	transmitter power, watts
r	equivalent resolution size, km
R	radius of the Earth, km
R_A	distance from Earth center to satellite, km
R_c	slant range from satellite to center of doppler cell, km
R_g	ground range from sub-satellite point to center of doppler cell, km
s	slot spacing
S	received signal power, watts
S_c	ground spacing between center of doppler cell of front antenna beam and the corresponding doppler cell center of the aft antenna beam, km

S_m	surface distance separating the two orthogonal data cell measurements of the same incidence angle
$S_N(f)$	spectrum at the low pass filter (LPF) output
S_s	spacing along satellite subtrack between successive scans of the same antenna
$S(k)$	wave number spectrum
t_m	time gate during each repetition period for data readout, sec
t_p	measurement period per antenna per polarization, sec
T	pulse repetition period of transmit pulses, sec
T_a	antenna brightness temperature, ^oK
T_o	reference temperature, ^oK
T_s	system noise temperature, ^oK
v_e	earth's surface velocity at any latitude
V_e	earth's surface velocity at the equator
v_s	satellite orbit velocity, km/s
v_g	satellite ground velocity, km/s
v_2	component of earth's surface velocity in the plane of the antenna beam
v_3	vector sum of satellite velocity component and earth's velocity component in the plane of the antenna beam
U	wind speed, m/s
X	coordinates
Y	
Z	
α_i	inclination of the satellite orbit
β	3 dB beamwidth of fan beam antenna in wide dimension

γ	earth center angle measured from subsatellite to center of doppler cell, degrees
δ	angle between constant doppler line and line normal to satellite track (doppler line rotation angle), degrees
Δ	amount of spacecraft or antenna rotation to compensate for earth's velocity
p	phase between adjacent antenna elements
ε	antenna efficiency
θ	nadir angle from satellite to center of doppler cell, degrees
θ_i	incidence angle of center of doppler cell, degrees
θ_p	nadir angle from satellite to direction of peak antenna gain, degrees
λ	wavelength of transmitter frequency
Λ	ocean wavelength
λ_g	waveguide wavelength
ν	wind speed power coefficient
σ^o	normalized radar scattering coefficient
$\hat{\sigma}^o$	estimate of σ^o
σ_M	standard deviation of σ^o measurement
σ_N	standard deviation of noise measurement
σ_{SN}	standard deviation of signal plus noise measurement
τ	integration period
τ_p	transmit pulse length, sec.
τ_{SN}	integration period for signal plus noise, sec.
τ_N	integration time for noise only, sec.
ϕ	3 dB fan beam antenna beamwidth (narrow dimension)

ϕ_L	latitude of the satellite
ϕ_{Ln}	latitude of doppler cell n
$\Delta\phi_{Ln}$	latitude difference between the satellite and a doppler cell
ϕ_m	angular direction front antenna data cell measurement moves at the time orthogonal measurement by the aft antenna is made - angle measured from satellite subtrack
ϕ'	surface angle from satellite track to center of antenna beam, degrees
Φ	polar angular coordinate
ψ_A	angle between the earth's velocity and the plane of the antenna beam - ascending portion of the orbit
ψ_D	angle between the earth's velocity and the plane of the antenna beam - descending portion of the orbit
ω_i	angle between the earth's surface velocity and the satellite negative velocity - measured in the plane of the antennas parallel to the surface of the earth
Ω_L	longitude of the satellite
Ω_{Ln}	longitude of doppler cell n
$\Delta\Omega_{Ln}$	longitude difference between the satellite and a doppler cell

General Subscripts

HH	1st letter is transmit polarization and
HV	2nd letter is receive polarization
l	lower edge of doppler cell
m	integer
n	integer
u	upper edge of doppler cell
VV	1st letter is transmit polarization and
VH	2nd letter is receive polarization

BACKGROUND

Backscatter Theories - A Prospectus

The theory of radar backscatter from rough surfaces, and particularly from the sea, has been the subject of much recent research.[2] Most modern theories describe the ocean surface by a model that involves two scales, one for that portion of the ocean spectrum having wavelengths much larger than the radar wavelength (gravity waves) and the other for the part of the ocean spectrum comparable with the radar wavelength (capillary waves). Wright[3] and Bass and Bocharov[4] used the small perturbation method to describe the backscatter; later, Wright[5] considered the effect of the perturbed surface lying on tilted planes caused by the larger structures. A similar approach was used by Valenzuela.[6] Chia[7] developed the backscatter using the Kirchhoff tangent-plane approximation, but real autocorrelations based on wave spectra were used rather than the usual mathematically convenient function. Jackson[8] also used this method, but took into account the curvature, thus permitting extension of the range of validity of the Kirchoff method. Semyonov,[9] Barrick and Peake,[10] and Krishen[11] used the Kirchoff method for part of the spectrum and added in the contribution, mostly important over a different angular range, of the small perturbation theory; later Semyonov[12] added a correction factor for interrelations between the two parts of his solution. Fung and Chan[13,14] developed a method for modifying the Kirchoff method in terms of the small perturbation solution for the undulating surface, thereby coupling the results from the two methods applicable to different parts of the wave spectrum and angular range.

Regardless of the theory used, for incidence angles greater than about 25° the primary factor governing ocean radar backscatter is the amplitude of the capillary portion of the sea spectrum. In the small perturbation theory, these components are readily related to the radar wavelength by the Bragg scattering condition that the radar return from adjacent crests of the most important ocean component adds in phase. This leads to the condition:

$$\Lambda \sin \theta_i = n \lambda/2$$

where Λ = ocean wavelength (component of spectrum)

λ = radar wavelength

θ_i = angle of incidence (from local vertical).

The first order perturbation theory shows results only for $n = 1$, although intuitively one might expect higher order "Bragg resonances" also to be important. At an incident angle of 30° this means that the "Bragg wavelength" for the ocean is the same as the probing radar wavelength. Consequently, the Bragg wavelengths at that angle are, for the frequencies considered here , in the capillary region of the ocean wave spectrum.

Measurements of capillary waves on the open sea are extremely difficult, for the capillary waves usually are superimposed on other sea components many orders of magnitude larger. Consequently, our knowledge of capillary waves is based on theory and on measurements in wind-wave tanks. Recent work at NYU[15,16] has combined the data from several investigators so that the variation in the capillary spectrum with wind speed can be determined. The data from three different sources correlate well.

The wave spectrum in the capillary region can be expressed in terms of

$$S(k) = \frac{(4.05 \times 10^{-3})\ D}{k^3}$$

where k is the wave number in cm^{-1} and
D is a variable depending on wind speed .

Experimental data indicate that $S(k)$ continues to grow with increasing wind speed above about 3 m/sec. Below that speed, the capillary waves die away extremely rapidly. Thus, it is felt that the radar measurements will be invalid because the signals received will be dominated by returns from small patches where gusts are above the 3 m/sec. critical wind speed.

Although preliminary analysis indicates an increase of backscatter with wind and wave development, none of the theories of electromagnetic backscatter presently account for breaking waves, sea foam, whitecaps and flying drops of spray. Under these conditions, sea surface is no longer a single valued function of position and time. The development of an adequate theory to account for these effects is difficult. Good observations of sea return are rare for high winds although the available data show an increase in backscatter up to 20 meters/sec. or so.

Measurements of Radar Backscatter

Radar backscatter has been measured both in the laboratory and over the open ocean for a range of wind speed. Wright of the Naval Research Laboratory (NRL) has performed backscatter measurements at X-Band in a water tank with wind-driven waves as a function of wind speed and fetch. Preliminary results (as reported by Pierson and Stacy[16]) indicate that the scattering coefficient σ^o at 60° incidence and vertical polarization increases with wind speed. Furthermore, Pierson claims that these results are quantitatively consistent with the growth of the capillary portion of the wave spectrum as a function of increasing wind speed. The range of wind speeds in Wright's experiment corresponds to ocean winds at 20 meter height of approximately 3m/s to 30 m/s.

Perhaps the most extensive effort for measuring the radar sea return from aircraft was carried out by NRL.[17-20] Measurements were obtained as a function of polarization (vertical and horizontal), incidence angle, and azimuth angle using four pulse radars operating at 428, 1228, 4455, and 8910 MHz. Other aircraft measurements[21,22] taken by NASA-JSC at 13.3 GHz used a fan-beam doppler radar technique to obtain σ^o_{VV} for incidence angles between ±60°. Near nadir data were excluded. Recently measurements have also been obtained by NASA-LaRC, using a long pulse (beam limited) 13.9 GHz scatterometer[23,24] (AAFE RADSCAT) installed in a NASA-JSC aircraft.

An analysis of NRL and NASA-JSC data has been performed by Apel[25] to determine the dependence of scattering coefficient on ocean surface wind speed. In an attempt to remove instrument biases in absolute cross section, he normalized the value of σ^o at a given incidence angle to the value of σ^o at $\theta_i = 10^\circ$. A semilogarithmic presentation of the normalized differential scattering coefficient $\sigma^o(35^\circ)/\sigma^o(10^\circ)$ versus wind speed is given in figure 1. This type of data presentation has led to considerable controversy concerning whether or not the scattering coefficient saturates at the higher wind speeds. When these data are plotted on log-log paper (cross section in dB versus $10 \log_{10}$(wind speed)) as in figure 2, the result suggests a power law relationship such that

$$\sigma^o = A\,U^{\nu}$$

$$10 \log \sigma^{o} = 10 \log A + \nu(10 \log U)$$

$$\sigma^{o}(dB) = A(dB) + \nu(10 \log U)$$

where

A - is a constant
U - wind speed
ν - is the wind speed power coefficient

However, because of instrument biases and differences in operating frequency, it is better to consider each instrument data set separately. Daley[20] has curve-fitted power law response to NRL scattering coefficient versus wind speed data (wind speeds approximately 5 to 25 meters/second) for constant incidence angles. These power law curves for vertical and horizontal polarization are shown for upwind and downwind conditions in figures 3 and 4 respectively. The ν's for upwind and downwind observations for several incidence angles are given in the following table.

Freq.	Direction	Polarization	Exponent	Incidence Angle				
				20°	25°	30°	40°	50°
8.9 GHz	Upwind	VV	ν	0.20	0.25	0.37	0.66	0.73
	Downwind	VV	ν	0.20	0.29	0.36	0.80	0.80
	Upwind	HH	ν	0.00	0.33	0.58	0.87	1.03
	Downwind	HH	ν	0.00	0.29	0.52	1.04	1.30

Typical results from the NASA-JSC 13.3 GHz scatterometer (as analyzed by Bradley[21] and Claassen[22] of The University of Kansas) are shown in figure 5 for the upwind case. The normalized differential scattering coefficient ($\sigma^{o}(35^{o})/\sigma^{o}(10^{o})$) indicates a power law response of wind speed to the 1.44 power. The average exponents inferred from these data are given in the following table.

Freq.	Direction	Polarization	Exponent	Incidence Angle, θ_i	
				25°	35°
13.3 GHz	Upwind	VV	ν	1.12	1.49
	Downwind	VV	ν	1.15	1.60
	Crosswind	VV	ν	1.00	1.40

Recently, preliminary results[23,24] have been reduced from three aircraft flights of the AAFE RADSCAT. Upwind, downwind and crosswind observations of σ^o_{VV} and σ^o_{HH} are presented versus wind speed for 0°, 10°, 20°, 25°, 30°, 40°, 50°, and 55° in figures 6 and 7. The inferred wind speed exponents are given in the following table.

Freq.	Exponent	Polarization	Direction	Incidence Angle, θ_i				
				20°	25°	30°	40°	50°
13.9 GHz	ν	VV	Upwind	1.0	1.53	1.9	1.9	1.9
			Downwind	.99	1.51	1.9	1.89	1.9
			Crosswind	.99	1.54	1.9	1.9	1.9
13.9 GHz	ν	HH	Upwind	.94	1.48	1.9	2.0	2.0
			Downwind	.94	1.48	1.85	1.98	1.98
			Crosswind	.76	1.24	1.69	1.95	1.95

Previous observations indicated an azimuthal variation of cross section at the large incidence angles; i.e.: a wind direction dependence. To examine this effect the RADSCAT antenna was pointed to the nadir and then the aircraft flown in high banked circles. This maneuver simulated a conical scan of the ocean's surface. The results for three flights are shown in figure 8. Maxima were obtained in the upwind and downwind directions with the upwind value being the greater. Minima were obtained for crosswind observations. The shape of the curve is in qualitative agreement with Bragg scattering from the anisotropic capillary waves.[26] These results imply that both wind speed and direction may be inferred from multilook radar observations. Satellite measurements of scattering coefficient have been recently obtained during the NASA-JSC Skylab program. The S-193 RADSCAT experiment was a mechanically scanned pencil-beam 13.9 GHz scatterometer (similar to AAFE RADSCAT). Preliminary results[27] of ocean scattering coefficient versus wind speed are shown in figure 9 for horizontal polarization at 50° incidence angle. These data seem to verify the power law response to wind speed as do the measurements at other angles and polarizations.

During several Skylab S-193 passes, simultaneous measurements were obtained with the AAFE aircraft instrument. The Skylab and AAFE RADSCAT had nearly identical antenna characteristics, but because of the large altitude difference the footprint for the satellite sensor was larger by greater than 2 decades. Results from a pass on June 5, 1973, in the Gulf of Mexico are shown in figure 10a, b, for vertical and horizontal polarizations respectively. The scattering coefficients for S-193 are approximately 2.5 dB greater than those for AAFE RADSCAT for incidence angles between nadir and 30°. Beyond 30° the Skylab measurements fall off more rapidly than do the aircraft data which results in a crossing of the two curves around 40° incidence angle. While neither the AAFE or Skylab data are in final form the agreement is considered good.

PERFORMANCE REQUIREMENTS

During Phase A studies and in the early part of Phase B, the SeaSat study teams considered many candidate sensors to provide the User community with scientific and operational data in the areas of oceanography, meteorology, and geodesy. As a result of these studies, the microwave scatterometer was selected as the prime wind vector sensor. Several configurations of each instrument were considered so that trade-offs could be made in designing the overall payload. The scatterometer options included fan beam antenna systems, scanning pencil beams and mixtures of the two. Decisions have now been made which narrow the scatterometer options to a fixed fan beam antenna design.

Scatterometer specs have been developed for a prototype quasi-operational instrument to provide wind speed and direction measurements (Mode I). A research mode is included to resolve uncertainties about the effects of sea state on wind sensing ability and to verify instrument design boundaries, such as optimum incidence angles and wind speed measurement range. In the development of these specs only wind speed measurement error due to instrument errors in scattering coefficient were considered.

Frequency selection for the scatterometer has two conflicting directives. To minimize weather effects low frequencies (X-Band) are best while higher frequencies (Ku-Band) are preferred for maximum sensitivity to local wind speed. Skylab data taken at 13.9 GHz (Ku-Band) show favorable wind speed sensitivity which compares well with aircraft data also taken at 13.9 GHz. Less wind speed sensitivity is generally shown by NRL data taken at 8.9 GHz. Both of these points were discussed in detail in an earlier section. Recent wave tank data[28] confirm that Ku-Band should be more sensitive to surface winds than are lower band frequencies. Another factor concerning frequency selection is hardware development under AAFE RADSCAT, Skylab, and other programs which also leads one to favor operation in the Ku-Band.

Frequency allocation and RFI have been considered jointly with other onboard radars and application has been made for a scatterometer frequency between 14.5 and 14.9 GHz. The SeaSat altimeter frequency allocation request is for the 13.4 to 13.9 GHz band.

Mode I

The scatterometer specs for Mode I were established from User requirements (ref. 1) of wind vector measurement range and accuracy, swath width, resolution cell size, and grid spacing (fig. 11). Orbit altitude, which is dictated by several factors, affects the scatterometer performance primarily by controlling swath width. The impact of other User requirements on the instrument specs will be seen in the discussion developed below.

The manner of transforming wind speed requirements to σ^o accuracy (thus SCAT specs) can be seen by examining the σ^o_{VV} data in figure 12.[*1] These data are from the AAFE RADSCAT aircraft instrument and correlate well with S-193 Skylab data as shown in an earlier section. The allowable User wind speed error bar of ±2 m/sec or ±10 percent (whichever is greater) is projected on the σ^o curves for different incidence angles. By translating this error bar to the σ^o axis, as shown, the corresponding instrument error in σ^o is thus determined for each incidence angle and wind speed. These data are tabulated in fig. 13. At small incidence angles (less than 25°) the dependence of σ^o on wind speed is much less and the σ_M exceeds the state of the art in measurement accuracy of scattering cross section (±0.5 dB) $\sigma_M/\sigma^o = K_p$ = .12[*2]). In addition, for these incidence angles, σ^o is also a function of sea state. For these reasons, earth incidence angles below about 25° are thereby excluded defining the inner edge of the measurement swath at 201 km from satellite subtrack for an altitude of 808 km (fig. 14). The outer edge of the main swath is set at about 55° earth incidence which is approximately the outer angle of present aircraft and S-193 data.

An additional high wind measurement zone (fig. 14) between 55° and 65° is specified since returned signals should be large enough to measure for high winds and it is expected that σ^o will remain wind sensitive. The total swath width for high wind measurements is 761 km on each side of the satellite subtrack giving a total swath width of 1522 km, with an edge-to-edge sensitivity of 1924 km.

Although the σ^o sensitivity to wind speed variation is about the same for upwind, downwind, or crosswind conditions, the magnitude of σ^o for crosswind is less; hence, the crosswind design used here is a worst case design. In addition, since the instrument design is controlled by the expected σ^o levels for low wind speeds, its performance as a wind sensor will generally exceed requirements for moderate and high wind speeds over the entire swath.

[*1] Vertical polarization σ^o characteristics are used throughout this spec development whenever User requirements are involved directly. Horizontal polarization is also an instrument requirement.

[*2] See link analysis section for definition of K_p.

The scatterometer's ability to measure wind speed does not cut off sharply[+] at low wind values but simply becomes less accurate. This is in keeping with User requirements since interest in wind speed begins to wane in the 3 to 5 m/sec zone; the scatterometer is specified to measure wind speeds at least as accurate as ±2 m/sec down to 4 m/sec with decreased accuracy below that. The required K_p values to accomplish this are shown in figure 15, along with their respective σ^o values.

The lower boundary of scatterometer dynamic range (figure 15) is based on measured σ^o_{VV} crosswind values for 4 m/sec (fig. 16a). σ^o_{HH} values are shown in figure 16b for comparison. It should be reemphasized that the instrument will measure winds below 4 m/sec for the inner swath section but with reduced accuracy. The upper end of scatterometer dynamic range is based on a maximum upwind σ^o_{VV} value of +10 dB determined by extrapolating curves in figure 6 to 50 m/sec. For incidence angles below 15°, σ^o_{VV} occurs at low wind speeds.

Since scatterometer calibration is achieved for σ^o vs wind speed after orbiting the satellite, absolute σ^o measurements are not required. A fixed bias error in the absolute value of σ^o would not affect wind speed accuracy because that bias would be calibrated out. Serious errors in σ^o would however affect instrument measurement range and a ±2 dB accuracy has been selected to avoid this problem. The incremental system resolution of σ^o needs to be ±.25 dB so that variations in σ^o can be measured down to 10 percent without interference due to system limitations. This 10 percent standard deviation in σ^o is considered to be the lowest reasonable error for relative σ^o based on present satellite scatterometer designs capability.

Since the ocean radar scattering coefficient is a function of wind direction as well as wind speed[*], both a forward and an aft looking beam are required to obtain data at two azimuth angles for each resolution cell. An optimum implementation is forward and aft beam, each squinted 45° off the subsatellite track to provide measurements which are separated in azimuth by 90°. In this configuration, the mean of the two measurements for a given resolution cell is nearly independent of wind direction. The quadrant of wind direction can be determined from conventional meteorological data and satellite obtained

---

[*] The dependence of σ^o on wind direction has been clearly demonstrated (figure 10) in the AAFE RADSCAT program and must be accounted for.

[+] Capillary wave generation does cease abruptly at still lower wind speeds.

cloud mosaics[+] and thereby improve the accuracy of the wind speed determination. AAFE RADSCAT data have been processed in this manner to demonstrate feasibility (figure 8 and 17); however, there still are substantial amounts of experimental measurements required to define σ^o wind direction dependence for a wide range of wind speeds and sea states. At present it is difficult to theoretically model this azimuth angle effect with any degree of confidence. A first effort has been made by Pierson (ref. 26) based on available aircraft data (figure 18a and b). Having determined wind speed from σ^o values taken at orthogonal azimuth angles, individual forward and aft beam data can be used to determine wind direction. This is done by matching these two data points for a given resolution cell, fig. 19, to a previously determined experimental curve for that wind speed and incidence angle. This wind direction information can be used if necessary to iterate to an improved wind speed accuracy.

A review of wind direction measurement errors using this two-azimuth angle technique is given by Pierson[26]. Generally, it shows the scatterometer can easily make ±20° accuracy measurements in wind direction for the higher wind speeds, but is less accurate for the lower wind speeds. There is no need for alarm, however, since certain mode options to be discussed in later sections of this report give improved accuracy.

In principle then, each resolution cell must be viewed from two azimuth angles to remove the wind direction effect and the best angular separation appears to be 90° in azimuth. The time between illumination of a given resolution cell by the forward and aft beams depends on the cells position along the fan beam illumination. Thus, the scatterometer must be designed properly in order to make the forward and aft beam cells cross. Each 50 km resolution cell must always have two footprints in it, thus, giving σ^o data at azimuth angles 90° apart as shown in fig. 19, and discussed in the subsequent design section. The doppler cell spacing along the fan beam is picked so that the cross track grid spacing for scat measurements are 100 km center-to-center and the along track grid spacing should be set at 100 km by the scat controller to comply with User requirements. In a high resolution mode the number of doppler cells along the fan beam could be increased to give 25 km resolution

---

[+] Private communication with W. J. Pierson, CUNY.

with essentially contiguous coverage. This is an option not presently planned for SeaSat A since it is more costly and User requirements do not specify the higher resolution.

It should be pointed out, as shown in figure 11, that both the resolution cell size and grid spacing requirement impact the allowable scatterometer integration time and signal to noise requirements.

Both σ^o_{VV} and σ^o_{HH} measurements are specifically required although present data indicate either one polarization or the other could satisfy User wind field measurement needs. In order to establish which polarization is best as a function of incidence angle and wind speed, both polarizations are included. Another aspect of dual polarization is that differential measurements may prove to be valuable for sensing ocean parameters.

Polarization purity of the wave incident on the Earth's surface is required to avoid interference due to returns at the opposite polarization. This requires attention not only to spacecraft attitude and antenna alignment, but also to polarization purity as well. According to aircraft data, σ^o_{VV} values can be as much as 10dB higher than σ^o_{HH} values for large incidence angles. In order to maintain the interferring vertically polarized signal 30 dB below the horizontally polarized signal during the σ^o_{HH} measurement, a polarization purity of 99 percent at the Earth's surface was chosen along with a cross polarization antenna requirement of 20 dB. This combination assures the 30 dB separation required between the two signals which limits that error source to about .25 dB ($\Delta \sigma^o/\sigma^o \times 100 \simeq 6$ percent).

Mode II

The scatterometer specifications for the research mode have been established based primarily on instrument sponsor requirements. These requirements fall into two categories: One is concerned with studying parameters other than local winds (for example, sea state) which might affect the scatterometer performance and the other concerns data collection so that more definitive scatterometer design boundaries can be established (such as optimizing incidence angle and wind speed measurement range). Secondary requirements for Mode II includes the measurement of wind speed (not direction) along the satellite subtrack to supplement Mode I wind speed measurements. Wind direction would have to be derived from other sources such as synoptic wind fields developed from Mode I data taken concurrently or from ground truth data.

Performance specifications of the scatterometer for Mode II are given in Fig. 20. The σ^o measurement range for Mode II is extended beyond Mode I specs to allow data taking from 0° to 65°. The fan beam is required to be oriented along the satellite subtrack so that σ^o data can be taken (0° to 65°) for a given patch of ocean. Highly instrumented test sites would be used whenever possible to give quality ground truth data. The actual angles are selected so that a smooth curve can be drawn to show the σ^o dependence on angle for a given set of surface conditions. The steepness of the curve (ref. 29) warrants smaller angular steps near nadir. Scatterometer dynamic range and σ^o accuracy required for mode II was determined in the same manner as was used for Mode I. The σ^o_{max} values listed near nadir are compatible with data taken with the Skylab S-193 altimeter (ref. 30). Since Mode II required σ^o data for the full set of incidence angles from the same patch of ocean, the only azimuth angles that are allowed are 0 and 180°; i.e., either a forward or aft antenna looking along the satellite subtrack.

Polarization purity (99.7 percent) of the wave incident on the Earth's surface is specified for Mode II due to the cross polarization measurement requirement. The high polarization purity requirement was included to improve the accuracy for the σ^o_{HH} and σ^o_{HV} measurements, where the return is lower than σ^o_{VV} at higher incidence angles. There is no reliable data to indicate how much depolarization can occur at the ocean surface so the antenna cross polarization spec is dictated by present antenna capability rather than by a rigid error analysis. It is hoped that Skylab S-193 data will improve our knowledge in this area prior to the SeaSat launch but it is unlikely that such knowledge would warrant a major antenna development to improve the SeaSat A scatterometer polarization purity.

The geometric separation between measurements along the satellite subtrack is controlled by specific incidence angle selected and the timing of transmission from the Mode II antennas. If Mode II is being used to provide wind speed at 100 km grid points (for a specific incidence angle) then timing of the Mode II transmissions must be adjusted accordingly. Data taken to provide wind speed should be restricted to incidence angles between approximately 25° and 55°.

The resolution cell size for Mode II (50 km) assures compatibility with Users requirements when taking wind speed data and is small enough to allow ground truth data taken at the instrumented test sites to be representative of the general conditions over the 50 km footprint (i.e., no significant wind vector gradients across the footprint).

Other Modes

Other operational modes are indicated in Figure 21. The actual modes of the scatterometer instrument will depend on the instrument design and it is not intended that all modes listed in figure 21 be considered as absolute requirements, nor to limit the potential modes; in fact, some of these modes may not be achievable. What is intended is that the instrument have some mode flexibility beyond basic Modes I and II so that information derived from the early part of the SeaSat mission can be used to improve operation of the instrument after launch of SeaSat A.

The operational and scientific value of scatterometer data can be enhanced by judiciously using the instrument in various combinations of Modes I and II. For example, if only one polarization is used for Mode I, then portions of Mode II data could be taken in the time slot normally used for the other polarization. This still provides the User with wind speed and direction over the full design swath on both sides of the subtrack and gives wind speed along the satellite subtrack as well.

Other combinations of Modes I and II have been selected (fig. 21) which will give flexibility to use of the instrument after launch. Either Modes III or IV can be used after it is clear from early mission data which polarization is best for operational use. This then leaves more instrument time to be given to data collection in the research mode (antenna 5, figure 14). Modes V through VIII allow improved σ^0 measurement accuracy, with increased resolution cell size for one 500 km swath on either side of the satellite subtrack (but not both). Mode IX and X allow maximum operational data taking for all five antennas and one polarization.

A FAN BEAM SCATTEROMETER DESIGN

Mode I Analysis and Design

To meet the specifications and design requirements discussed in the previous section a fan beam design was chosen. This design incorporates four "stick" antennas for Mode I which produce a star-like illumination pattern on the surface of the earth. See Fig. 14. Backscatter data are sampled by each antenna with both vertical and horizontal polarization. With each polarization of each antenna following in turn, a scatterometer measurement is made from one antenna at a time. The data are obtained by transmitting a short pulse (5 msec) of CW signal then receiving, detecting, and integrating the return signal reflected from the ocean surface. Doppler filtering and range gating are used to divide the return signal along the fan beam into separate data cells at different incidence angles. An illumination pattern is produced which results in measurements over a wide range of incidence angles, with the forward looking and aft looking beams occurring at 90° azimuth with respect to each other. A half power beamwidth antenna of .5° x 25° was chosen as a compromise between antenna size and gain, swath coverage, and resolution capability. Figure 14 illustrates the coverage geometry produced by the fan beam design for incidence angles of approximately 25° to 65° in Mode I.

Figure 22 shows the side view geometry of one fan beam along with applicable equations defining the various geometric parameters, and figure 23 shows a plan view. Included in this figure are a few representative diagrams of resolution data cells along one antenna beam illumination. Figure 24 shows an enlarged view of the geometry of a resolution cell.

The instantaneous field of view (IFOV) or doppler cell is determined by the antenna beamwidth (narrow dimension), and doppler frequency line spacing (doppler bandwidth). The radar scattering coefficient (σ^o) is determined from the radar return signal for each doppler cell averaged for a specified measurement period, (t_p). The resolution data cell on the surface of the earth is then determined by the area generated by the doppler cell as a result of satellite motion during the measurement period. The equivalent resolution cell is defined by the square whose dimensions are the average of the dimensions of a rectangle within which the area generated by the moving doppler cell (IFOV) fits diagonally, as illustrated in figure 24.

The orientation of the doppler lines within the beam illumination varies along the total beam as illustrated in figure 23. For the inner cells (low incidence angles) the doppler line is oriented approximately 45° to the central beam axis. For the outer cells (high incidence angles), the orientation is about 13° with respect to the beam central axis. In addition the width of the beam illumination increases as a function of slant range from the satellite (see figure 23). Figure 25 is a plot of a few constant doppler lines created by the satellite motion. Two beam illumination patterns are included in this figure to illustrate the orientation of the doppler lines with the antenna beam. In figure 24 the constant doppler lines forming a doppler cell are shown as straight parallel line approximations. In actuality, as seen in figure 25 the constant doppler lines are approximately hyperbolas on the surface of the earth and are not exactly parallel. Also it is assumed that the edges of the beam illumination are parallel inside a doppler cell, when actually they diverge slightly as pointed out previously. These approximations are made to simplify the calculation of the cell area (A_c), and the parameter L. These approximations should have negligible error effects on the overall system design.

To establish a particular fan beam scatterometer instrument design, certain parameters and constraints must be fixed. The parameters that are fixed include satellite altitude, resolution (r), spacing between successive scans of the same antenna beam (S_s), number of antennas and polarizations to be sampled per scan, approximate range of incidence angles (θ_i) to be sampled, transmitter frequency (f_t), antenna half power beamwidths (β,ϕ), minimum and maximum σ^o to be measured, and the maximum error allowable on the radar scattering coefficient (σ^o) measurement. In addition the center of each resolution cell of the aft antenna must overlap the data from the center of the corresponding resolution cell of the forward antenna. Using these parameters the remaining parameters which establish the resolution data cell geometry and the instrument characteristics can be determined.

Once the antenna beamwidth is established the choice of doppler offset frequency of the IF and the corresponding bandwidths must be determined. These frequencies along with the data sample period (t_p) establish the resolution and geometric location of the doppler cells on the surface of the earth. To determine these frequencies the parameters l_c (distance on earth surface from center to center of doppler cells along antenna beam) and L (length of base of doppler cell) must be calculated (see figures 23 and 24). The following equations, derived in appendix 1, define these parameters.

$$l_c = \frac{\pi}{180} R \cos^{-1} \left[\cos\left(\frac{180\ S_s}{\pi R}\right)\right]^{1/2} \approx \frac{\sqrt{2}}{2} S_s \qquad (1)$$

$$L = \sqrt{2}\, r - \frac{v_g t_p}{\sqrt{2}} - R_c\, \phi - \frac{\sqrt{2}\ R_c\, \phi \sin \delta}{\sin\,(135 + \delta)} \qquad (2)$$

where:

R = radius of the earth, km

S_s = spacing along direction of satellite track between successive scans of the same antenna, km

r = equivalent resolution size, km

v_g = satellite ground velocity, km/sec.

t_p = data measurement period, seconds

R_c = slant range to center of cell, km

ϕ = narrow 3 dB beamwidth of fan beam antenna, radians

δ = angle between doppler line and line normal to satellite track, (doppler line rotation angle), degrees

The dimension l_c is only a function of the antenna scan spacing (S_s). This spacing of the resolution data cells must be picked to give cross track spacing equal to along track cell spacing. By choosing the proper earth angle (γ_1) to the first doppler cell the corresponding resolution data cells of the forward and aft antenna can be made to overlap at the center of the cell.* As noted in Appendix I, the earth angle γ for any cell is a function of the instantaneous spacing (S_c) between corresponding forward and aft antenna doppler cells, and S_c is a function of the beam scan spacing (S_s). Using

*With earth rotation effects neglected

the following equation, which is derived in Appendix 1, the proper value of the earth angle to the first doppler cell (γ_1) can be calculated.

$$\gamma_1 = \cos^{-1}\left[\cos \frac{810\ S_s}{\pi\ R}\right]^{1/2} \approx \frac{810\ S_s}{2\pi R} \qquad (3)$$

The variable L is a more complex parameter which varies in length along the beam illumination. Since the width of the beam illumination increases with incidence angle and the doppler line orientation changes, the value of L is made smaller for higher incidence angles in order to maintain the equivalent resolution cell constant along the beam illumination. If the parameter L is made a constant, then the equivalent resolution cell for higher incidence angles increases considerably. As seen from equation (2), L is a function of many parameters which include the equivalent resolution cell size, antenna beamwidth, slant range to the doppler cell, satellite ground velocity, data measurement period and doppler line rotation angle (see figure 24). Once l_c and L for each cell are determined, the remaining geometric parameters, doppler frequencies and doppler cell bandwidths for each resolution data cell can be determined using the equations derived in Appendix 1.

Measurement Timing

There are two categories of timing sequences that must be considered: (1) the measurement-to-measurement timing and (2) the transmit/receive/processing timing during each measurement.

Measurement-to-Measurement Timing.- The time between the start of successive measurements from each beam scan is equal to S_s/v_g. Since there are four antenna beams in Mode I, each requiring two polarization measurements, then $S_s/8v_g$ seconds is available per measurement period (t_p). For the baseline design, which is discussed later in more detail, S_s = 100 km, and v_g = 6.61 km/sec. for an altitude of 808 km giving a t_p of 1.89 seconds. Using a t_p of 1.9 seconds, figure 26 shows one complete measurement sequence. Periodically this sequence would be interrupted for calibration measurements. Note in figure 26 that the beam sequence is 1, 4, 2, 3, so that data scans alternate between antennas on opposite sides of the satellite sub-track. This sequence is the best timing to allow center overlap of corresponding forward and aft data scans, and to allow the incidence angle of the first doppler cell to fall at approximately 25°.

Intra-Measurement Timing.- The following are the parameters of intra-measurement timing which must be determined for each doppler cell in the fan beam pattern.

1. Transmit pulse length, τ_p
2. Range gate "ON" time
3. Range gate "OFF" time
4. Noise gate "ON" time
5. Noise gate "OFF" time
6. Time between successive transmit pulses, T

Figure 27 shows conceptually the timing for the transmit pulses, range gates for each cell, and noise gate times. The range gates are the periods when the signal plus noise from a particular doppler cell is filtered, square law detected, and integrated. The range gate time for each doppler cell is adjusted to match the two-way propagation time for each doppler cell. The noise gate is the period for filtering, detecting and integrating the mean noise level component with no signal present. The mean noise level is subtracted from the signal plus noise level measurement. This could be done by using a bi-polar integrator whose polarity is reversed during the noise integration period or by storing the noise level measurement for subtraction at a later time. To maximize the integration time, the transmit pulse length, τ_p, should be picked as long as possible. However, the sum of τ_p plus the transmit fall time, plus the i.f. relaxation time must be less than the two-way propagation time of the nearest point of the closest doppler cell.

Once τ_p has been chosen the range gate on and off times can be determined. The range gate on time is determined by the two-way range to the nearest point of a particular doppler cell. The range gate off time is determined by the sum of the two-way propagation time to the farthest point of that same doppler cell and the transmit pulse length τ_p. The noise gate period is chosen to minimize the required signal-to-noise ratio (SNR) needed to obtain a specified measurement accuracy. As shown in Appendix 2, the minimum SNR occurs when the noise integration period is approximately twice the signal plus noise integration period. The noise on-and-off gate times are chosen to occur after all signal from a particular doppler cell has been received.

The time, T, between successive transmit pulses is determined by the transmit pulse length, the two-way range to the farthest point of the outer doppler cell, the length of the noise integration period, and an additional small period of time to allow for data readout and pulse rise and fall times. The transmit pulses are repeated every T seconds throughout the measurement period, t_p. The total effective integration period, τ_{SN}, as indicated in figure 27, is equal to the duty factor $\left(\frac{\tau_p}{T}\right)$ times the measurement period, t_p.

Link Analysis

To perform link calculations the following equations, which are derived in Appendix 2, are used.

$$SNR_{in} = \frac{P_R}{K\ T_S\ B_c} \tag{4}$$

$$P_R = \frac{P_T (G/G_o)^2 \sigma^o L \epsilon^2 \lambda^2 L_s}{R_c^3 4\ \pi\ \phi\ \beta^2} \tag{5}$$

SNR_{in} = signal-to-noise ratio in the i.f. filter prior to the square law detector.

P_R = true value of the radar return signal power, watts

K = Boltzmann's constant

T_s = system noise temperature, degrees Kelvin

B_c = i.f. bandwidth of the filter preceding the square law detector, nominally set equal to the doppler spread over a cell, Hz

P_T = peak transmitter power, watts

G = gain of antenna to center of doppler cell

G_o = peak antenna gain

ϕ = narrow 3 dB beamwidth of fan beam antenna, radians

β = wide 3 dB beamwidth of fan beam antenna, radians

σ^o = normalized radar scattering coefficient

R_c = slant range to center of doppler cell, km

L = length of doppler cell along fan beam illumination, km

ε = antenna efficiency

λ = wavelength of transmitted frequency, km

L_s = miscellaneous system losses

In equation (5) all parameters are essentially known except σ^o. Therefore, the equation

$$\sigma^o = C\,P_R \tag{6}$$

can be written, where C = the value of all constants in equation (5). The true value of all the nonrandom parameters which make up C will not be known exactly, as well as the exact gains in the scatterometer receiver. Bias errors on the measurement of σ^o will occur as a result of not knowing these parameters exactly. Fluctuation or random errors will occur because the radar return signal from the surface of the earth is a Gaussian random process which is corrupted by system noise which is also a Gaussian random process. Both the bias and random errors will limit the absolute accuracy of the σ^o measurement. However, the minimum change in σ^o measurement that can be resolved will be limited only by the random errors. The minimum resolution of a measurement is generally accepted as the standard deviation σ_M of the measurement, i.e.,

$$\sigma_M = (\mathrm{Var}\ \hat{\sigma}^o)^{1/2} \tag{7}$$

where Var $\hat{\sigma}^o$ is the variance of the measurement of σ^o. Equation (6) can be written as,

$$\hat{\sigma}^o = C\,\hat{P}_R \tag{8}$$

where $\hat{\sigma}^o$ is an estimate of σ^o based on an estimate $\hat{P}_R$ of the true value of return signal P_R. If it is assumed that all parameters in equation (8) are essentially nonrandom except for $\hat{P}_R$, then σ_M is given by

$$\sigma_M = C\ (\mathrm{Var}\ \hat{P}_R)^{1/2} \tag{9}$$

where Var $\hat{P}_R$ is the variance of the measurement of P_R. It is shown in Appendix 2 that,

$$K_p = \frac{(\mathrm{Var}\ \hat{P}_R)^{1/2}}{P_R} \tag{10}$$

where K_p is a normalized parameter which gives the standard deviation of the estimate of P_R as a proportion of the true value of P_R. Combining equations (9), (10) and (6) yields,

$$\sigma_M = C\ K_p P_R = K_p\ \sigma^o \tag{11}$$

that is, the standard deviation σ_M of the measurement of $\hat{\sigma}^o$ can be evaluated directly by determining the standard deviation of the measurement of $\hat{P}_R$.

The following equation, derived in Appendix 2, yields the parameter K_p

$$K_p^2 = \left(\frac{\sigma_M}{\sigma^o}\right)^2 = \left(\frac{1}{B_c\ \tau_{SN}}\right)\left(1 + 2\ N/S + \frac{N^2}{S^2}\ \left[1 + \frac{1}{K_t}\right]\right) \tag{12}$$

where:

$N/S = \dfrac{k\ T_s B_c}{P_R}$ = noise to signal ratio at the i.f. filter prior to square law detection.

τ_{SN} = integration time of radar return signal plus noise, seconds

τ_N = integration time for noise only, seconds

K_t = τ_N/τ_{SN}

Using equation (4), (5) and (12), the expected standard deviation of the measurement of σ^o can be determined for each doppler cell as a function of σ^o.

Trade Off Analysis

A trade off analysis was conducted to determine the optimum choice of antenna beamwidth for a minimum transmitter power and highest equivalent resolution. This was done by chosing an antenna beamwidth and equivalent resolution and determining the transmitter power required to meet User requirements for swath width, minimum wind speed, and wind field measurement accuracy. A range of incidence angles of 25° to 55° was used in the analysis. Reasons for this choice of angles are given in the scatterometer performance requirements section. To cover this range of incidence angles a beam width of 25° in the wide dimension was required. Beamwidths in the narrow dimension of .35°, .5°, and 1° were used in the trade off analysis. Calculations were made for a range of equivalent resolutions of 10 to 60 km, with antenna scan spacings of 50 and 100 km, using four antennas and two polarizations.

Table I lists some of the parameters and constants used in the analysis. The level of two-way system losses, L_s, was assumed equal to - 6.4 dB. This loss is made up of 3 dB losses in both transmitting and receiving and .4 dB two-way loss through the atmosphere. The high transmitting and receiving losses are due to the required uses of rf switches and circulators, as seen in figure 38. The effective system noise temperature, T_s, referred to the input to the rf tunnel diode pre-amp, is equal to 1100 Kelvin. This value is determined using an assumed antenna brightness temperature of 200 K, a pre-amp noise figure of 6 dB, and a receiver loss of 3 dB. The value of T_s is calculated using the following equation:

$$T_s = \frac{T_a}{L_R} + \frac{T_o}{L_R} (L_R F - 1) \qquad (13)$$

where,

T_a = antenna brightness temperature, K

L_R = receiver loss, a factor larger than one

T_o = reference temperature = 290 K

F = tunnel diode pre-amplifier noise figure

Combining and rearranging equations 4 and 5, the following equation results:

$$P_T = \frac{(KT_s B_c) R_c^3 \; 4\pi\phi\beta^2}{N/S\sigma^o (G/G_o)^2 L\varepsilon^2 \lambda^2 \; L_s} \tag{14}$$

This equation was used in the trade off analysis for calculating required transmitter power. The value of N/S used in this equation is determined from equation 12. Substituting in the value of .5 for K_p and solving for N/S, the following equation is obtained.

$$N/S = \frac{(B_c \tau_{SN})^{1/2}}{2} \left(\frac{\tau_N}{\tau_N + \tau_{SN}}\right)^{1/2} \left(\frac{\tau_N}{\tau_N + \tau_{SN}}\right) \tag{15}$$

Since $\tau_N = 2\tau_{SN}$, this equation simplifies to,

$$N/S = \left(\frac{B_c \tau_{SN}}{6}\right)^{1/2} - 2/3 \tag{16}$$

The terms B_c, R_c, and L, for a data cell are determined for each resolution considered in the analysis, using the equations of Appendix 1. The term $(G/G_o)^2$ is determined from the antenna power pattern shown in figure 2 of Appendix 3, for the 25° beamwidth dimension. The values of the remaining parameters in equation (14) are listed in table I.

To minimize the required transmitter power the peak of the antenna beam must be directed toward the doppler cells with the higher incidence angles. This is done for two primary reasons; one, to compensate for the decrease in radar scattering coefficient, σ^o, at the higher incidence angles; and two, since the value of B_c is smaller for the higher incidence angles, to provide the increased SNR required to meet a .5 measurement accuracy. For the incidence angles considered in the trade off study (25° to 55°), the antenna was pointed at an incidence angle of about 51°, ($\theta = 43.5°$), so that the same transmitter power is required for both the 25° and 55° incidence angle measurements. This location was determined by a few trial and error calculations. At this position the antenna gain is approximately - 9 dB down from the peak antenna for the 25° cell, and -.15 dB down for the 55° cell.

Using equation (14) the required transmitter power was calculated for various equivalent resolutions, antenna scan spacings, and antenna narrow dimension beamwidths. The results of these calculations are shown in figure 28.

As seen from figure 28 the transmitter power required increases rather rapidly with decreasing resolution. This is due to the rapid decrease in the parameter L required to obtain the specified resolution, therefore reducing the bandwidth, B_c, and increasing the SNR required to obtain a .5 measurement accuracy. For a fixed antenna beamwidth the parameter L is the only parameter which can be reduced in order to obtain a smaller resolution. Since a narrow beamwidth dimension of the antenna produces a fixed illumination dimension on the surface, there is a lower limit to resolution size. The limiting resolution for the 1°, .5°, and .35° antenna beamwidths are approximately 35, 15, and 10 km., respectively.

As seen from figure 28, antenna beamwidths of .5° or smaller will be required to obtain resolutions of 50 km or smaller using reasonable transmitter powers. From antenna size considerations it appears that antenna beamwidths much smaller than .5° would be impractical (see Appendix 3). To meet the Users requirements for 50 km resolution an antenna beamwidth of 25° x .5° using a transmitter power of approximately 85 watts can be used to make 4 m/s wind speed measurements with a measurement accuracy (K_p) of .5 over incidence angles of 25 to 55 degrees at an altitude of 808 km. No system margin was assumed in this analysis.

Baseline Scatterometer Fan Beam Design - Mode I

After completing the trade-off study discussed in the previous section, a baseline design analysis was performed using the following design specification:

Equivalent resolution	low - 50 km; high - 25 km
Antenna scan spacing (along and cross track cell spacing)	low resolution - 100 km high resolution - 50 km
Swath width	1000 km primary zone

Satellite altitude - 808 km
Wind speed range - 4 m/s to 48 m/s
Accuracy - ±2 m/s or 10 percent whichever is greater for incidence angles of 25° to 55°
Range of σ^o 0 dB to -28 dB
1 standard deviation measurement error, K_p - 50 percent
Range of incidence angles - ~ 25° to 65°
Antenna beamwidth - .5° x 25°
Number of antennas - 4
Number of polarizations - 2 (horizontal and vertical)

(Non-rotating earth assumed)

Low Resolution Design

With these specifications, calculations for all cell parameters were made. The value of l_c which provides proper overlap of the forward and aft data cells is 70.709 km. The two-way propagation delay to the nearest cell is slightly under 6 msec., so a transmit on time as long as 5.7 msec. could be used. However, in Mode II operation, which will be discussed in a following section, the two-way propagation delay time to the 0° incidence angle doppler cell is approximately 5.3 msec. Therefore, for design simplicity, the transmit on time (τ_p) of 5 msec. was chosen for both Mode I and II. The integration time for noise only was chosen to be equal to twice the signal plus noise integration time. The following is a list of the various measurement times:

t_p = 1.891 seconds
τ_p = 5 msec.
T = 26.8 msec.
τ_{SN} = 352.8 msec
τ_N = 705.6 msec
t_m = 1.0 msec.
Duty Factor = 19 percent

To provide center overlap of the corresponding aft and forward data cells the location of the first doppler cell is required to be placed at an incidence angle of 24.1 degrees (see equation 3).

Using the equations in Appendix 1 all geometric parameters for each data cell were calculated for the low resolution baseline design. These parameters are listed in table II. A diagram of the data cells on the surface of the earth from one forward and aft antenna beam is shown in figure 29. The range gate on and off times for each cell is summarized in table III.

As seen from figure 29, a total of 15 contiguous data cells are produced within a fan beam illumination. To provide the 100 km along- and cross-track grid spacing between each data cell, every other data cell is used. This is illustrated in figure 30, where a more detailed diagram of the data cell illumination on the surface of the earth is presented. Measurements from additional surface area can be obtained by including the remaining 7 doppler cells (shown by dotted outlines in figure 30). Using these additional cells, a 50 km by 50 km spacing of data cells is provided. System performance is not affected by including these measurements. However, a slight cost increase will be incurred for additional doppler filters, detectors, and integrators.

To determine the measurement accuracy capability of the baseline design for various wind speeds, a link calculation for each data cell was performed. To do this a calculation of the noise to signal ratio (N/S) for each cell was made using equations (4) and (5). Substituting these values of N/S into equation (12) the measurement accuracy, K_p, was determined for various wind speeds for the incidence angle corresponding to each data cell.

The parameter σ^o for each wind speed (crosswind, vertical polarization) and incidence angle are obtained from figure 6c or figure 15.

The parameters B_c and L are taken from table II, for the corresponding data cell. Note that the value of L for cells 11 through 15 was made equal to the value of L at cell number 10. This was done to maintain a reasonable value of doppler bandwidth, B_c, since the value of L becomes very small for these outer cells, when trying to maintain a 50 km resolution. The resolution of these outer cells will be bigger than 50 km. For example, cell number 11 will have a resolution of approximately 53 km, and cell number 15 a resolution of 70 km.

The term $(G/G_o)^2$ is usually determined from the antenna radiation pattern such as that shown in figure 2 of Appendix 3. However, for these calculations the approximate equations,

$$(G/G_o)^2 = -24\left(\frac{\theta_p - \theta_n}{\beta}\right)^2 \text{, dB} \tag{17}$$

where,

θ_p = the nadir angle from the satellite to the direction of the peak antenna gain, and

θ_n = the nadir angle from the satellite to doppler cell, n, was used to determine this parameter for each data cell. The peak gain of the antenna is pointed slightly beyond cell number 7 ($\theta_p = 42°$). This is done, as explained in the trade-off study, to provide maximum gain for the outer doppler cells, where the scattering coefficient σ^o is the lowest, and thereby minimize the required transmitter power. Due to limited spacecraft dc power and TWTA availability, a maximum transmitter power of 125 watts has been chosen for the baseline scatterometer design. The values of the remaining constants in equations (4) and (5) are listed as follows:

$K = 1.38 \times 10^{-23}$, joules/ K

$T_s = 1100°$

$\phi = 8.75 \times 10^{-3}$ radians, (.5°)

$\beta = .436$ radians, (25°)

$\varepsilon = .5$

$\lambda = 2.157 \times 10^{-5}$ km, ($f_t = 13.9$ GHz) must be updated for SeaSat frequency allocation (approximately 14.6 GHz)

$L_s = -6.4$ dB, (-3 dB each for receiver and transmitter losses and -.4 dB for two-way atmospheric losses)

The results of the link calculations for the lowest σ^o design values corresponding to a 4 m/s wind speed (crosswind, vertical polarization) are summarized in table IV. The actual instrument accuracies, resulting from the link analysis, for data cells whose incidence angles correspond approximately to those required (figure 16) are summarized in table V, for various wind speeds. A review of tables IV and V will show that a measurement accuracy of .5 or better was only obtained for cells 3 through 9 ($\theta_i = 33°$ to $53°$) for a wind speed of 4 m/sec., thus cutting down the swath width at which 4 m/sec.

wind speed measurements can be made. However, at slightly higher wind speeds (6 m/s) the specified measurement accuracies can be extended to $\theta_i = 24^\circ$ to 56° (500 km swath). At a wind speed of 3 m/s an accuracy measurement of 50 percent can only be obtained for some of the middle data cells ($\theta_i = 33^\circ$ to 48°). The location of the peak antenna gain can be changed to greatly improve the performance of the low incidence angle data cells at a slight sacrifice in the performance of the higher incidence angles. By doing this the 4 m/sec. measurement swath width can be extended. If the peak antenna gain is placed at a θ_p of 41°, the measurement accuracies on data cells 1 and 2 are improved sufficiently to obtain 4 m/sec. measurement capability from cells 1 through 9 (450 km swath width). A minimum windspeed measurement capability of 5 m/sec., and 12 m/sec. is obtained at cells 10 and 15 respectively.

A comparison of tables IV and V with figure 16 shows that some margin exists in the measurement accuracy over those required, for the middle incidence angles at low wind speeds, and for the low and high incidence angles at higher wind speeds. It is generally desirable to provide a certain amount of margin to cover changes in the value of various parameters, such as transmitter power, transmitter and receiver losses, and receiver gains. Figure 31 is a plot which shows the amount of signal margin obtained as a function of wind speed for the incidence angles shown in table IV.

Figure 32 is a plot showing how the measurement accuracy varies as a function of the scattering coefficient, σ^o, for the 7 incidence angles listed in table V. Similar curves which lie in the region between cell number 1 and number 7 would result for the remaining eight data cells. This figure shows that the normalized measurement error, K_p, is a monotonically decreasing function of σ^o. This is to say, it also decreases as signal-to-noise ratio (SNR) increases, since σ^o is proportional to SNR as seen from equations (4) and (5). This relationship is shown in figure 33 where σ^o is plotted as a function of SNR for three data cells. Also shown plotted is the normalized measurement error, K_p, as a function of SNR. Note that for SNR < 0 dB, K_p decreases proportional to the increase in SNR. For SNR >> 0 dB, no significant decrease in K_p can be obtained by increasing SNR. This is due to the inherent Gaussian fluctuation of the radar return signals and the limited number of measurement samples taken of the ocean surface. The equivalent number of sample measurements taken can be shown to be the product of the doppler bandwidth and integration or sample time, that is, the product $B_c \tau_{SN}$. How this limit affects the ultimate measurement accuracy can be seen from equation (12), where K_p approaches a value of $\left[\frac{1}{B_c \tau_{SN}}\right]^{1/2}$, as SNR approaches infinity. The ultimate accuracy varies, since each cell has a different doppler bandwidth. For cell number 1 the ultimate accuracy is approximately 1 percent, and for cell number 15 this value is slightly over 3 percent.

The measurement accuracy at any SNR can be improved at the expense of resolution by averaging the measurement of one or more adjacent data cells. This is the same as increasing the number of sample measurements or the $B_c \tau_{SN}$ product, which it can be seen effectively increases the resolution size. The measurement accuracy will improve by the square root of the number of data cells averaged. If data cells along the antenna beam are averaged the resolution size will effectively increase by a factor equal to the number of cells averaged. However, if successive scans of the same antenna are made so that adjacent cells are contiguous, then averaging along track and/or cross track data cells will increase the resolution size by only a small percentage determined mainly by the sample period, t_p. This is more easily seen by a review of figures 23 and 24.

A review of equation (4) and (5) will show, after a few sample calculations, that the term $B_c R_c^3/L$ is essentially a constant for all data cells (see table IV). This is due to the increase in the value of R_c^3 being directly offset by the corresponding decrease in the value of B_c and L. Therefore, the only variable between data cells which affects the SNR received for a particular σ^o is the antenna gain function $(G/G_o)^2$, since the remaining parameters in equation (5) are constants. Note also that for a particular SNR the value of K_p varies between data cells as a function only of the square root of the ratios of their doppler bandwidths, B_c.

High Resolution Design

A high resolution design analysis was performed in an attempt to obtain 25 km resolution capability, at higher wind speed conditions. This was done by dividing the 50 km resolution doppler cells into two 25 km doppler cells, so that 50 km resolution measurements could still be obtained by averaging measurements from the two 25 km doppler cells. If the value of the parameter L is reduced in half from its value at 50 km resolution, received SNR will be the same since the bandwidth, B_c, will also be reduced in half. However, the $B_c\tau_{SN}$ product will also be reduced in half, resulting in the measurement error of one 25 km cell being increased by the $\sqrt{2}$. This increase, however, is offset by the $\sqrt{2}$ improvement resulting from averaging two 25 km data cells as discussed in the previous section and Appendix II. Thus, no degradation results in meeting the original 50 km resolution measurement accuracy requirements.

A review of the equation defining the parameter L will show that it must be reduced by more than a factor of two in order to reduce the equivalent resolution from 50 to 25 km. In fact, for the inner cells, L must be reduced by a factor slightly greater than 3. For the middle and outer cells, L becomes very small because of the effect of the doppler line orientation. Because of this as noted previously in the 50 km baseline design, the equivalent resolutions of cells 11 through 15 were made greater than 50 km. For these outer cells, at best, L can be reduced by a factor of 4; however, the resolution of these cells will still be about 35 to 53 km. Therefore, little will be gained by dividing the outer cells into two higher resolution cells. For the middle cells, L can be reduced by a factor of 3 or 4, resulting in equivalent resolutions of 26 to 33 km. The measurement error of one 25 km cell relative to a 50 km cell will increase by $\sqrt{w}$, where w is the factor by which L is reduced from its 50 km value. Since an improvement of only $\sqrt{2}$ is obtained by averaging two 25 km cell measurements (to obtain a 50 km measurement), additional transmitter power or slightly higher σ° (higher wind speed), equal to $\sqrt{w/2}$, will be required to obtain the same measurement accuracy as that obtained by using a single 50 km resolution data cell.

With this approach a high resolution (25 km) baseline design was conducted by dividing each of the first ten 50 km cells into two 25 km cells. For this design a closer grid spacing of 50 km was used. For this spacing it is advisable to either scan the antennas at a higher rate, which would reduce the integration time, or to limit the number of antennas or polarizations scanned. For the higher scan rate the decreased integration time will degrade the measurement accuracy, limiting the data to higher wind speeds. In an actual system design both approaches could be incorporated, since it would involve only a control function change in the timing to provide either mode of operation. For the high resolution baseline design a four-antenna one-polarization approach was used, which provides a 1000 km swath width. Figure 34 illustrates a sample of the scan pattern for this baseline design. As seen from this figure, a total of 20 contiguous data cells are produced within a fan beam illumination for incidence angles from 25° to 55°. As in the case of the 50 km baseline design, every other 25 km data cell is used to provide the 50 km along- and cross-track grid spacing (figure 34).

The results of the calculations for 25 km resolution are shown in Tables VI and VII, for each incidence angle. Minimum σ^o with a measurement accuracy of .5, and the approximate corresponding windspeeds are shown. Also shown in these tables are the results obtained by combining two 25 km cell measurements to obtain a 50 km cell measurement. As seen from the tables, wind speed measurements of 4 m/sec can be made at design accuracies for incidence angles ranging from about 34 to 41 degrees for 25 km resolution and about 33 to 51 degrees for 50 km resolution. At the lower and higher incidence angles the full swath width requirement is met only if windspeed exceeds 8 m/s for the 25 km resolution case, and 6 m/s for 50 km resolution case.

Mode II Scatterometer Design

Mode II is the experimental operating mode in which a fan beam antenna is directed along the satellite subtrack to measure σ^o at incidence angles of 0 to 65 degrees for the same ocean area. The general specifications and design requirements for Mode II operation are discussed in a previous section. The basic area of illumination for the Mode II antenna is illustrated in figure 14. Designs for this mode are described in the following sections.

Doppler Cell Design

Definition of the dependence of radar scattering coefficient on θ_i require σ^o measurements every 5° of incidence angle from 0 to 65 degrees plus a measurement at 2.5°. In addition measurements at these incidence angles must cover the same specified surface area. There are two possible design approaches which can be used to meet these requirements. The first is to choose doppler cells at the exact incidence angles required. In this approach the center of the cells would not be equidistant on the surface of the earth; therefore, measurements at the required incidence angles would require variable timing to cover the same surface area. The second approach is to choose doppler cells whose center-to-center surface spacing is some fixed increments or a multiple of this increment. The measurement time interval would then be equal to this spacing or its multiple divided by the satellite ground velocity. In this approach each incidence angle measurement would cover the same surface area; however, the incidence angles would not occur exactly at the required values.

Figure 35 illustrates the geometry of the surface illumination for the two options and one polarization. Also included in the figure is an enlarged view of the resolution data cell. The resolution data cell is determined partly by the doppler bandwidth, which establishes the parameter L, and the smear distance generated during the measurement period. Any combination of doppler cell length (L) and measurement period (t_p) can be chosen to form a specified resolution length. It is shown in Appendix 2 that the optimum choice of these parameters, which maximizes the $B_c \tau_{SN}$ product, is made when the smear length and the doppler cell length are made equal. A 50 km resolution length has been specified; therefore, the doppler cell length and the smear length have been set equal to 25 km. With a satellite ground speed of 6.61 km/s, the measurement period, t_p, of 3.782 seconds is obtained.

In figure 35 option I shows the fixed increments of incidence angle approach with variable surface spacing of the data cells. Also note the overlap of the 0° and 5° cells by the 2.5° cell. Option II shows the fixed surface spacing approach, using increments of 50 km along with their corresponding incidence angle. The data cells are contiguous for the lower incidence angles. At the higher incidence angles only those cells are included whose incidence angles are closest to the required values.

A measurement made at the other polarization would be shifted on the surface of the earth by 25 km. Therefore, the data cells of the two polarization measurements would only overlap the same surface area by 25 km (50 percent). The two additional cross-polarization measurements would not overlap the first polarization measurement and only part of the second polarization measurement. A total of 125 km would be covered by the four polarization measurements. To provide better overlapping coverage of the four polarization measurements, the measurement period, t_p, could be reduced and the doppler cell length (L) increased. However, as shown in Appendix 2, the $B_c \tau_{SN}$ product would be greatly reduced resulting in a less accurate measurement.

Measurement Timing

Intra-Measurement Timing.- In order to simplify the electronics, the timing philosophy is kept the same as Mode I. The transmit pulse length in Mode II is therefore kept at 5 ms. Also the pulse repetition period was made equal to 26.8 msec., the same as Mode I. For option I, the range gate on-times are shown in table VIII. The range gate off-times are 5 msec later. Option II timings are approximately the same.

Measurement-to-Measurement Timing.- To produce overlap of the same surface area by each incidence angle measurement, the time interval between measurements must be properly adjusted.

Figure 36 illustrates the measurement sequence required for both options at H and V polarization for each incidence angle measurement to cover the same surface area. As seen from the figure for both option I and II it requires over 200 seconds and a surface distance of over 1300 km for all incidence angles to measure the same surface area. At each incidence angle a 3.78 second measurement is made for each of two polarizations. Sufficient time is not available to make cross-polarization measurements that cover the same surface area. Cell number 15, ($\theta_i = 65°$) will be the first cell to cover a specified surface area, followed in sequence by the remaining lower incidence angles. The times shown between each measurement are the times required to allow the spacecraft to traverse the appropriate distance so that the measurement at the next incidence angle will occur at the specified surface area. The times are shown for a 808 km altitude spacecraft with a ground speed of 6.61 km/s. Note that in option I the 2.5° incidence angle (cell number 2) is not included, since for two polarization measurements, sufficient time is not available between cells 1 and 3 for the 2.5° measurement to cover the specified area. With one polarization measurement however, cell number 2 could cover the same specified area. It must be noted however, that during each 3.78 second measurement period, measurements for all incidence angles are being obtained including an incidence angle of 2.5°, even though they may not be at the same specified area.

The major difference between option I and option II is the sampling interval used between measurements. In option II the measurement interval is the time it takes to move 50 km on the surface, or multiples thereof. As such, completely new measurements could be made each 50 km (t_p = 7.56s.), thus allowing each incidence angle to contiguously cover the same surface of the earth. In option I the time intervals are not at a fixed rate; therefore, all incidence angles will not necessarily fall on the same surface of the earth except for the surface area measured by cell number 15.

During the 200 plus seconds that Mode II data are being obtained, Mode I will be inoperative, since both these modes will be using common receiver front ends and transmitter. Certain mode combinations are desirable, such as those shown on figure 21. For example, some Mode I data can be obtained in the surface area adjacent to that of Mode II. This can be accomplished if only one polarization is used in both modes. This is illustrated in figure 37, where a combined measurement sequence for Mode I and Mode II using one polarization is shown. Mode II measurement timing is arranged to allow each incidence angle to measure the same surface area starting with cell 15. During the off-time between each Mode II measurement period, four Mode I measurements are made, one for each antenna. The measurement timing for Mode I is adjusted to allow the same surface overlap of the front and back antennas for most of the measurement periods. Since the off-time interval of Mode II at the lower incidence angles is small, only two Mode I antennas can be sampled during those time periods (see figure 37).

Link Calculation.- A link calculation was performed for option I. Equations 4, 5, 15, and 16 were used to perform these calculations. Prior to these calculations the geometric parameters for each doppler cell were first determined using the equations of Appendix 1. The spacecraft angle, θ, slant range, R_c, and doppler bandwidth, B_c, obtained from these calculations are required in the link calculations. The parameter L is the same for all data cells and is equal to 25 km. The integration period for signal plus noise is 705.6 ms., and for noise only is 1.411 sec. The remaining parameters in the link equations are the same as those in Mode I except the antenna beamwidth, B.

Since a relatively wide S/C angle, θ, of about 54^o must be covered for Mode II measurements, a wider beamwidth antenna than used in Mode I is required. The same antenna design as used in Mode I can be used with one dimension being changed to increase the beamwidth B, as discussed in Appendix 3. A beamwidth of $.5^o \times 40^o$ was chosen for the Mode II design. The 40^o beamwidth was chosen as a compromise on coverage, antenna gain loss and maximum beamwidth obtainable using a modified Mode I antenna design (Appendix 3). The beam center was pointed at S/C angle, θ_p, of 42.1^o. This angle was picked so that the required minimum σ^o measurement of 0 dB can be made at an incidence angle of 0^o.

Using equation 15, the N/S required to obtain a measurement accuracy (K_p) of .5 was determined for each data cell. Then using equations 4 and 5, the σ^o value which would provide this N/S value was calculated. Table VIII lists the geometric parameters and the results of the link calculations. As seen from the table the minimum σ^o obtained at incidence angles above 50^o did not meet the required minimums listed in Fig. 20. Since these calculations were made with a transmitter power equal to 125 watts, very little margin is available for some of the incidence angles which did meet the required minimums. The only alternative to obtaining the required minimum σ^o measurements, with adequate margin, is to use two $.5^o \times 25^o$ beamwidth antennas.

Earth Rotational Effects

In the fan beam design presented in the previous sections the effects of the earth's rotation were not included. This was done to simplify the initial design analysis. However, in the final system design the effects of earth rotation on the doppler frequencies and bandwidths, location of data cells on the earth's surface, and the measurement overlap requirements of the forward and aft antenna cells will have to be taken into consideration. A brief discussion of these effects is presented in this section. A more detailed analysis with applicable equations is presented in Appendix 1.

At first it would appear that the tangential motion (.465 km/s at the equator) of the earth's rotation would have a small effect on the fan beam design. This is not the case. Two effects, which are major consequences, occur on the system design: one is the change in the doppler velocity created by a component of the earth's tangential velocity, and the other is the movement of the surface area measured by the forward antenna data cell during the time required for the spacecraft to travel the surface distance (S_c) separating the forward and aft antenna data cells. Each of these problems is discussed in the following paragraphs.

The tangential component of the earth's rotational velocity must be combined with the satellite velocity component to establish the doppler filter frequencies and bandwidths. This component, although small in comparison to the satellite velocity and easily accounted for in doppler velocity calculations, does not remain constant in amplitude or orientation with respect to the satellite velocity throughout the satellite orbit. For this reason the doppler filter frequencies and bandwidths for any particular incidence angle will vary throughout the orbit. Since the orbit is retrograde, the satellite velocity vector at the maximum latitude points (72° N and S) is 180° away from the earth's tangential velocity vector. Throughout the remaining portion of the orbit the satellite velocity vector (as well as antenna beams) rotates $\pm 72^{\circ}$ from this position. The maximum rotation of 72° occurs at the equator. The earth's tangential velocity decreases with increasing latitude, from its maximum value at the equator, as a function of the cosine of the latitude angle.

The total doppler velocity[1] on all antenna beams is approximately equal

---

[1] Doppler velocity in this discussion refers to the component in the plane of the antenna beam, parallel to the earth's surface. This velocity must be multiplied by $\sin\theta$ to obtain the doppler velocity to a particular data cell along the beam (see figure 22).

at the maximum latitudes of 72°. During the remaining portion of the orbit the doppler velocity is either increased or decreased from this value as a function of the changing orientation of the antenna beams with respect to the earth's velocity vector. During the ascending portion of the orbit the magnitude of the doppler velocity is increased on beams 1 and 3, and decreased on beams 2 and 4. During the descending portion of the orbit the situation is reversed. In both cases the magnitude of the doppler velocities on beams 1 and 3 are always approximately equal. The same holds true for beams 2 and 4. The slight inequality that does occur is caused by the latitude difference between these beams at any point in the orbit. At the equator the latitude differences have a negligible effect on the doppler velocities. At the maximum spacecraft latitude (72°) the difference in latitude between beams 1 and 3 and between beams 2 and 4 causes about a $1.7^{o}/_{o}$ difference in their doppler velocities at a 65° incidence angle and about a $.4^{o}/_{o}$ difference at a 24° incidence angle.

The doppler velocities on each beam change about $6^{o}/_{o}$ as the spacecraft moves from the maximum latitude to the equator. Since this change is positive in one crossing direction and negative in the other crossing direction, a total change in doppler velocity of about $12^{o}/_{o}$ occurs on each beam throughout one orbit. Since only one bank of fixed doppler filters will be provided in the receiver processor, the effect of the variable doppler velocity will be to shift the location of the data cell corresponding to each doppler filter in and out along each beam. The shift will thus cause an expanding and compressing of the range of incidence angles throughout the orbit. For example, the incidence angle for cell number 1 will vary from approximately 22.7° to 25.8°, for cell number 10 from approximately 51° to 61°, and for cell number 15 from 60° to 75°.

One possible solution to alleviate the wide variation in incidence angles caused by the varying doppler velocity is to rotate the spacecraft approximately ±3.3° about the yaw axis during a single orbit. It is shown in Appendix 1 that by slight continuous yawing of the antenna beams the doppler velocity can be held essentially constant throughout the orbit. The effect of this yawing is to compensate for the variable earth velocity vector by varying the component of satellite velocity (function of cos ϕ', see figure 22) which contributes to the total doppler velocity. Instead of a continuous yawing, a few step changes in yaw during specific portions of the orbit could result in significant improvement. The rotation of the spacecraft impacts the design of the satellite bus, and as such may be costly to incorporate. However, the scatterometer can be utilized without rotation capability with a minimum impact on User requirements.

The capability of providing forward and aft antenna data cell overlap at the same surface of the earth is greatly affected by the earth's rotation. At the equator, the surface of the earth at data cell number 1 of the forward antenna will have moved approximately 31 km by the time cell number 1 of the aft antenna reaches the corresponding location. Thus only a small corner of the equivalent resolution square of the two data cells will overlap. At the maximum incidence angle (65°) the surface measured by the front antenna data cell will have moved approximately 130 km before the aft antenna data cell reaches the corresponding location. The remaining data cell measurements of the front antenna will move by some amount between these extreme values. At the higher latitudes, of course, the amount of shift of the front antenna data measurements is correspondingly smaller due to the decrease in the earth's tangential velocity. (See Appendix 1 for a more detailed discussion of the amount and direction of data cell movement caused by the earth's rotation throughout the satellite orbit).

Thus it is seen that the ideal situation of data cell overlap depicted in figure 30 is greatly altered by the rotational motion of the earth. This movement of the forward antenna data cells considerably compromises the ability to make orthogonal measurements to determine surface wind direction and to remove the effects of wind direction in making a wind speed measurement. A study of figure 30 will show that when the data cell measurements of the front antenna are shifted by the amount indicated in Appendix 1, they lie either in a blank area between data cells or they fall in an area measured by the aft antenna at a higher incidence angle - or a combination of both. A possible solution to providing orthogonal measurements of the same surface of the earth from the front and back antennas is to include all contiguous data cells along each antenna beam and make the along-track spacing (S_s) equal to 50 km. By doing this the blank spaces shown in figure 30 will be filled in, therefore providing contiguous coverage of 50 km squares within which scattering coefficient measurements are made. Thus two orthogonal measurement cells can be found in which common overlap area does exist, although the incidence angles at which these measurements are made are not exactly the same. (Maximum difference in incidence angle that will occur is approximately 4.5^o). The sample time, t_p, will have to be reduced in half to provide 50 km along-track spacing. The measurement integration time will also be reduced in half which will result in a measurement accuracy degradation by $\sqrt{2}$. The minimum wind speed that can be measured will be slightly higher (about 1 m/s) than the baseline design capability.

Mode II will be affected in a similar manner, in trying to obtain measurements at the same surface of the earth at all incidence angles. However, if the test sites are located at a high latitude (60^o or higher), the 65^o incidence angle measurement will only move by about 40 to 50 km until the 0^o incidence angle measurement is made. The higher incidence angle measurements will fall closer to the 65° measurement since there is less delay between those measurements.

Data reduction and processing tasks will be significantly increased due to earth's rotational effects. Precise orbital and earth-local parameters are required so that correct determination of the location and incidence angles of the resolution cells can be made for each measurement, and so proper combining of forward and aft antenna cell measurements are assured.

In summary then, the following changes to the baseline design can be made to accommodate the effects of the earth's rotation:

1. Provide contiguous data cells for each antenna beam and set the timing to provide along-track data cell spacing of 50 km.
2. Locate sites for Mode II measurements at latitudes of 60° or greater, or at lower latitudes in groups of 5 incidence angles on successive orbits.

BASELINE HARDWARE SYSTEM DESCRIPTION

System Block Diagram

The particular design considered here is based largely on systems used in other scatterometers, such as AAFE RADSCAT and Skylab S-193. Because of this, some sections contain more detail than would otherwise be available. This design is intended only as an example.

A block diagram of the SeaSat Scatterometer is shown in Figure 38. This system utilizes an integrated frequency synthesizer to generate all of the necessary rf signals at UHF and microwave frequencies needed by the exciter, transmitter, mixers and scatterometer processor. The synthesizer consists of a highly stable crystal controlled oscillator from which all required frequencies are derived thus assuring coherency throughout the sensor. The low level microwave output of the synthesizer is amplitude gated (on and off) by a pin diode type switch to insure high isolation (typically $\geq$ 60dB) between the "ON" and "OFF" states. The pulsed rf is amplified in the final output stage which consists of a TWT and integrated power supply. The 125W peak power output pulse is directed to the stick antenna array through a series of waveguide components consisting of electromechanical waveguide switches, circulators and 1X5 waveguide diode switch. Each antenna has associated with it a switchable polarization circulator which is commanded in a preset fashion by the timing and control electronics.

Received rf energy from the proper antenna is directed through the chosen path of the 5-way switch and sent through the T/R circulator and receiver protection circulator to the low noise preamplifier, band pass filter and first conversion mixer. In the mixer a microwave signal derived from the stable oscillator in the synthesizer is added to the return signal to produce a coherent IF signal which is then fed to the scatterometer processor. The Scatterometer processor consists of IF amplifiers, amplitude=control range gates, and processing channels. The processing channels for the data consist of a bank of band-pass doppler filters, detectors, dc amplifiers and signal integrators. The timing and control for the processor are provided by the control unit.

The function of the control unit is to accept spacecraft commands and power, to generate the precise timing and control logic needed by the scatterometer to form rf pulses and operate the processor. In addition it accepts the output scatterometer data and instrument telemetry parameters and formats them so they are compatible with the spacecraft data system.

Scatterometer Transmitter

Integrated Frequency Synthesizer.- Using an ultra stable crystal oscillator the integrated frequency synthesizer generates all required rf signals at UHF, VHF and microwave frequencies for the scatterometer. Stabilities of better than 1 part in 10^8 over a few milliseconds and 1 part in 10^7 per day can be obtained with proportionally controlled heated crystal oscillators. The oscillator frequency chosen depends on the final output frequency selected as well as the desired 1st and 2nd rf frequencies, but would typically be 50 MHz or below and employ a 3rd overtone crystal. The basic oscillator output is then buffered, amplified, and used to drive a harmonic generator which produces integer multiples of this frequency. Using stripline or combline filter techniques the required UHF/VHF signals for down conversion are then obtained. Another portion of the crystal oscillator's output is used to drive a phased locked solid state multiplier and produce the proper microwave signal for the output.

Pin Diode Switch - This component utilizes a pair of pin diodes shunted across the waveguide structure which are driven into conduction or back biased into the "OFF" state. Typical performance achievable in such a switch is > 35 dB ON/OFF ratio,< 2 dB insertion loss in ON state, ≤ 10 nsec rise and fall time and <2 nsec rf pulse delay. These performance specifications insure high fidelity pulse with ultra sharp rise and fall times to guarantee proper scatterometer performance.

Output TWTA.- The output TWTA amplifies the pulsed rf input from the pin diode switch and has an output of 125W minimum saturated power. Based on a TWT design derived from a Hughes tube (294-H) to be flown on the Japanese Broadcast Satellite, the TWTA can operate over a 200 MHz bandwidth with greater than 40 percent efficiency including the power supply. Typical gain is 42 dB minimum at saturation, and advanced cathode design should permit operation for over 3 years with little or no performance degradation. The TWTA requires spacecraft power input, commands to turn on the heaters and high voltage plus a pulse modulation input command. It provides telemetry outputs of critical temperatures, voltages and currents to the scatterometer housekeeping telemetry data stream. Although reliability figures for space qualified TWT's are greater than 90 percent, overall amplifier system reliability can be further enhanced by parallel operation of two or more tubes which provides redundancy or can be used to increase total output power if operated simultaneously. However, in this simultaneous mode the relative phase of the TWTA output must be maintained within 25° (ref. 31) in order for the signals to add properly. Under present technology, there is no convincing evidence that TWTA's can be operated together with this phase stability.

Scatterometer Receiver

Receiver "Front End".- The scatterometer receiver front end consists of the 5-way waveguide diode switch which directs energy from the chosen antenna to the T/R and receiver protection circulator. Both of these circulators together provide about 60 dB of isolation for the receiver when the pulse is being transmitted. In the receive state they should exhibit less than 0.5 dB insertion loss. The low noise device will be a Tunnel Diode Amplifier (TDA). It has a gain of 30 dB with a 6 dB noise figure. Minimizing losses from the TDA to the antenna should keep the total system noise temperature to about 1100 K (assuming total loss of 3 dB).

The output of the TDA is combined with a low level microwave signal derived from the synthesizer in a low noise, low conversion loss diode mixer to produce the 1st IF signal.

Scatterometer Processor - The scatterometer processor must amplify, detect and integrate the samples of the backscattered energy and provide a measure of the total received power to the spacecraft data system. To do this, systems of this nature generally amplify the 1st IF signal, then mix once again with a signal derived from the synthesizer to bring the information down to a convenient 2nd IF frequency. At this frequency the range gating and doppler filtering are accomplished which achieve the desired spatial resolution on the ground. After filtering, the selected element is detected, amplified and integrated for a specific period of time. It is this integrated value, which represents an estimate of the received power, which is A/D converted and put in the data stream.

The scatterometer processor is controlled through logic and switching commands provided by the digital control electronics to insure the proper sequence of range gating and integration.

Control Unit

The function of this unit is to act as interface between the spacecraft and the scatterometer providing all necessary input voltages and accepting output data and housekeeping telemetry. A few of its functions are: generation of pulses of proper width and PRF for scatterometer transmitter, generation of proper sequence of commands for switching antennas and antenna polarization, generation of proper commands for operation of scatterometer processor including range gates and integration commands, distribution of raw and processed voltages to scatterometer components, formating, A/D converting, and multiplexing of input data and telemetry, and delivery of the scatterometer data stream to the spacecraft data handling system.

Antenna System

A total of five separate antennas are used in the scatterometer design. Each antenna can operate in one of two linear polarization modes. The four antennas used in Mode I have an antenna beamwidth of .5 x 25 degrees. The fifth antenna has a beamwidth of .5 x 40 degrees and is used in Mode II only. Various antenna designs can be utilized to produce the required beamwidths. The design requires a smooth uniform antenna pattern in both planes, with low side lobe levels and high polarization purity. For a more detail discussion of an antenna design which produces these qualities see Appendix 3.

CONCLUDING REMARKS

A historical review of microwave scatterometer aircraft and satellite measurements has been given to show that the instrument can be used to sense ocean winds on a global basis. Instrument performance characteristics have been developed based on User requirements for a wind sensor on the SeaSat-A satellite. User requirements include a wind speed measurement range of 4-50 m/sec ±2 m/sec for a swath width of 1000 km, a resolution cell size of 50 km, and a measurement grid spacing of 100 km.

A specific instrument design was developed that satisfies the User requirements and specifications with minor exceptions. This instrument uses 4 antenna arrays, each with a .5° x 25° half power beamwidth, producing a 761 km measurement swath on each side of the satellite. Wind speed measurements are made over a range of incidence angles from 24° to 66°. A minimum wind speed measurement of 4 m/s can be made for incidence angles of 24° to 53° (450 km swath on each side) and a 5 m/s measurement for incidence angles of 24° to 56° (500 km swath on each side). Higher wind speeds (7 to 12 m/sec.) are required for satisfactory measurement at the outer incidence angles.

A research mode instrument design using a fifth antenna (beamwidth = .5° x 40°) was developed to make σ^o measurements along the satellite sub-track for incidence angles of 0° to 65°. However, the minimum σ^o measurement requirements for this mode can not be completely satisfied for the higher incidence angles (50° to 65°). The minimum σ^o that can be measured at an incidence angle of 45° is -24.5 dB, which is only 1/2 dB from the required levels.

Changes to the baseline design can be made to accommodate the effects of Earth's rotation as follows:

1. Provide contiguous data cells for each antenna beam and set the timing to provide along-track data cell spacing of 50 km.
2. Locate test sites for Mode II measurements at latitudes of 60° or greater, or obtain measurements in groups of 5 incidence angles on successive orbits at a lower latitude.

REFERENCES

1. "SeaSat-A Study Task Team Report", Oct. 1973.

2. Bass, F. G., I. M. Fuks, A. I. Kalmykov, I. E. Ostrovsky and A. D. Rosenberg, "Very High Frequency Radiowave Scattering by a Disturbed Sea Surface, " *IEEE Transactions*, vol. AP-16, no. 5, pp. 560-568, September 1968.

3. Wright, J. W., "Backscattering from Capillary Waves with Application to Sea Clutter, " *IEEE Transactions*, vol. AP , no. 6, pp. 749-754, November 1966.

4. Bass, F. G. and V. G. Bocharov, "On the Theory of Scattering of Electromagnetic Waves from a Statistically Uneven Surface," *Radioteknika i electronika*, vol. 3, pp. 251-258, 1958.

5. Wright, J. W., "A New Model for Sea Clutter," *IEEE Transactions*, vol. AP-16, no. 2, pp. 217-223, March 1968.

6. Valenzuela, G. R., "Backscattering of Electromagnetic Waves from a Tilted Slightly Rough Surface," *Radio Science*, vol. 3, no. 11, pp. 1057-1066, November 1968.

7. Chia, R. C., "The Theory of Radar Scatter from the Ocean," University of Kansas Center for Research, Inc., Technical Report 112-1, October 1968.

8. Jackson, F. C., "A High Frequency Correction to the Kirchoff Approximation, with Application to Rough Surface EM Wave Scattering," GSL Report TR-71-8, Dept. of Meteorology and Oceanography, New York University, 1971.

9. Semyonov, B., "Approximate Computation of Scattering of Electromagnetic Waves by Rough Surface Contours," *Radio Engineering and Electronic Physics*, vol. 11, pp. 1179-1187, 1966.

10. Barrick, D. E. and W. H. Peake, "Scattering from Surfaces with Different Roughness Scales: Analysis and Interpretation ," Research Report, Battelle Memorial Institute, Ohio, 1967.

11. Krishen, K., "Correlation of Radar Backscattering Cross Sections with Ocean Wave Height and Wind Velocity," Lockheed Electronics Company, TR No. 649D.21.025, Houston, Texas, March 1970.

12. Semyonov, B., "An Approximate Calculation of Scattering of Electromagnetic Waves from a Slightly Rough Surface," Radiotekika i Electronika (USSR) 11, (English Translation), 1966.

13. Fung, A. K. and H. L. Chan, "On Backscatter from Two-Scale Rough Surfaces," Propagation Limitations in Remote Sensing, AGARD Convention, Colorado Springs, June 1971.

14. Chan, H. L. and A. K. Fung, "Backscattering from a Two-Scale Rough Surface with Application to Radar Sea Reutrn," NASA Contractor Report CR-2327, November, 1973.

15. Pierson, W. J., Jr., F. C. Jackson, R. A. Stacy and E. Mehr, "Research on the Problem of Radar Return from a Wind Roughened Sea," Principal Investigator's Review, Advanced Applications Flight Experiments, NASA Langley Research Center, pp. 83-114, October 1971.

16. Pierson, Willard J., Jr. and Robert A. Stacy, "The Elevation, Slope, and Curvature Spectra of a Wind Roughened Sea", NASA CR-2247, November, 1973.

17. Sutherland, A. J., "Spectral Measurements and Growth Rates of Wind Generated Water-Waves," Stanford University, Dept. of Civil Engineering, Technical Report 84, August 1967.

18. Guinard, N. W. and J. C. Daley, "An Experimental Study of Sea Clutter Model," IEEE Proceedings, vol. 58, no. 4, pp. 543-550, April 1970.

19. Valenzuela, G. R., M. B. Laing and J. C. Daley, "Ocean Spectra for the High Frequency Waves as Determined from Airborne Radar Measurements," Journal of Marine Research, vol. 29, no. 2, 1971.

20. Daley, J. C., "An Empirical Sea Clutter Model", NRL Memo Report 2668.

21. Bradley, G. A., "Remote Sensing of Ocean Winds Using a Radar Scatterometer," Ph.D. Thesis, University of Kansas Center for Research, Inc., September 1971.

22. Claassen, J. P. and H. S. Fung, "The Wind Response of Radar Sea Return and its Implication on Wave Spectral Growth," Technical Report 186-5, University of Kansas Center for Research, Inc., March 1972.

23. Jones, W. L., L. R. Shultz, and N. D. Akey. "AAFE-RADSCAT Observations of Wind-Driven Seas," 1972 USNC/URSI Fall Meeting, Williamsburg, Virginia.

24. Swift, C. T. and Jones, W. L. "Satellite Radar Scatterometry", 1974 IEEE InterCon, New York, New York, March 26-29, 1974.

25. Apel, J. R. "A Hard Look at Oceans From Space", AIAA 9th Annual Meeting, Washington, D.C., January 8-10, 1973, paper no. 73-11.

26. Pierson, W. J., V. J. Cardone, and J. A. Greenwood, "The Applications of SeaSat-A to Meteorology", Technical Report prepared for SPOC of NOAA/NESS under Grant No. 04-4-158-11. The University Institute of Oceanography, The City University of New York, August 1974.

27. Moore, R. K., "Congressional Presentation", February 20, 1974.

28. Mitsuyasu, H. and T. Honda, "The High Frequency Spectrum of Wind Generated Waves", J. of Oceanographical Society of Japan (to be published), Vol. 30, no. 4, 1974.

29. Ruck, George T., Donald E. Barrick, William D. Stuart, Clarence K. Krichbaum, "Radar Cross Section Handbook", Vol. II, Plenum Press, 1970.

30. Private communications with J. T. McGoogan, Wallops Flight Center, Wallops Island, Va.

31. Sullivan, John W., "Want More Power from Your TWT's? Parallel 'em!", Microwaves, pp. 38-45, July, 1974.

32. Mumford, W. W., Schiebe, E. H., "Noise Performance Factors in Communications Systems," p. 20 and p. 23.

33. Davenport, Jr., W. B. and Root, W. L., "Random Signals and Noise," pp. 253-257.

Table I - Trade off analysis parameters and constants.

σ^o = - 10.8 dB for $\theta_i = 25^\circ$, and - 25.5 dB for $\theta_i = 55^\circ$

Altitude = 808 km

Measurement accuracy, $K_p = .5$

Transmit pulse width, $\tau_p = 5.5$ msec.

Pulse repetition period, $T = 26.7$ msec.

Integration period for signal plus noise, $\tau_{SN} = 195$ msec. for 50 km spacing and 389 msec. for 100 km spacing

Integration period for noise only, $\tau_N = 2\tau_{SN}$

Transmitted frequency, $f_t = 13.9$ GHz ($\lambda = 2.157 \times 10^{-5}$ km)

Antenna efficiency, $\varepsilon = .5$

Antenna beamwidth, $\beta = 25^\circ$

Antenna beamwidth, $\phi = .35^\circ$, $.5^\circ$ and 1.0°

Table II - Baseline Geometric Parameters - MODE I

CELL No.	R_g, km	γ, deg	θ, deg	$θ_i$, deg	R_c, km	f_D, Hz	δ, deg	L, km	B_c, Hz
1	318.26	2.85	21.30	24.15	875.76	177377	5.01	52.75	25002.8
2	388.97	3.49	25.36	28.86	907.34	209199	6.86	51.78	22055.1
3	459.68	4.12	29.11	33.24	943.84	237611	8.95	50.55	19112.6
4	530.39	4.76	32.54	37.31	984.70	262710	11.18	49.03	16306.1
5	601.10	5.39	35.66	41.06	1029.39	284713	13.48	47.22	13725.7
6	671.81	6.03	38.48	44.52	1077.45	303901	15.76	45.06	11401.0
7	742.52	6.67	41.03	47.70	1128.43	320582	17.99	42.54	9348.0
8	813.23	7.30	43.32	50.63	1181.94	335063	20.13	39.61	7553.3
9	883.95	7.94	45.39	52.33	1237.66	347630	22.14	36.24	5998.3
10	954.66	8.57	47.24	55.82	1295.29	358544	24.03	32.37	4655.2
11	1025.37	9.21	48.91	58.12	1354.58	368033	25.77	32.37	4051.1
12	1096.08	9.84	50.41	60.25	1415.32	376299	27.38	32.37	3532.0
13	1166.79	10.48	51.75	62.23	1477.31	383512	28.87	32.37	3085.6
14	1237.50	11.11	52.97	64.08	1540.41	389820	30.22	32.37	2701.3
15	1308.21	11.75	54.06	65.81	1604.48	395348	31.47	32.37	2369.7

Alt. = 808 km.

r = 50 km.

l_c = 70.709 km

S_s = 100 km.

f_t = 13.9 GHz

Table III Range Gate Timing - MODE I

Cell Number	1	2	3	4	5	6	7	8	9	10	11	12	13	14	15
R. G. ON (ms)	5.8	6.1	6.3	6.6	6.9	7.2	7.5	7.9	8.3	8.6	9.0	9.4	9.9	10.3	10.7
R. G. OFF (ms)	10.8	11.1	11.3	11.6	11.9	12.2	12.5	12.9	13.3	13.6	14.0	14.4	14.9	15.3	15.7
R. G. WIDTH (ms)	5	5	5	5	5	5	5	5	5	5	5	5	5	5	5

Table IV Baseline Link Analysis and Accuracy Parameters For 4 m/s Wind Speed - MODE I

CELL No.	$\frac{B_c R^3}{L}$	$KT_s B_c$	$B_c \tau_{SN}$	$(G/G_o)^2$, dB	σ^o, dB	S/N, dB	K_p, %
1	3.18×10^{11}	3.8×10^{-16}	8820.23	-16.46	-16	-17.27	70.4
2	3.18×10^{11}	3.3×10^{-16}	7780.37	-10.63	-21	-16.44	62.1
3	3.18×10^{11}	2.9×10^{-16}	6742.36	-6.38	-22.5	-13.69	35.9
4	3.17×10^{11}	2.5×10^{-16}	5752.31	-3.44	-24	-12.24	28.1
5	3.17×10^{11}	2.1×10^{-16}	4842.0	-1.54	-24.2	-10.54	20.2
6	3.16×10^{11}	1.7×10^{-16}	4021.93	- .476	-26	-11.26	27.1
7	3.16×10^{11}	1.4×10^{-16}	3297.69	- .036	-26.3	-11.11	29.0
8	3.15×10^{11}	1.1×10^{-16}	2664.58	- .058	-26.8	-11.62	37.7
9	3.14×10^{11}	9.1×10^{-17}	2116.02	- .441	-27	-12.19	45.9
10	3.13×10^{11}	7.1×10^{-17}	1642.21	-1.05	-28	-13.79	74.3
11	3.11×10^{11}	6.1×10^{-17}	1429.11	-1.83	-28	-14.55	94.5
12	3.09×10^{11}	5.4×10^{-17}	1245.98	-2.72	-28	-15.40	123
13	3.07×10^{11}	4.7×10^{-17}	1088.52	-3.65	-28	-16.31	161
14	3.05×10^{11}	4.1×10^{-17}	952.94	-4.62	-28	-17.25	213
15	3.02×10^{11}	3.6×10^{-17}	835.94	-5.59	-28	-18.17	281

P_T = 125 watts
θ_p = 42^o
t_p = 1.891 seconds
T = 26.803 msec.
τ_p = 5 msec.
τ_{SN} = 352.77 msec.
τ_N = 705.53 msec.
BW = $.5^o\times25^o$
T_s = 1100 K
wind speed = 4m/s

TABLE V FAN BEAM SCATTEROMETER ACCURACIES - MODE I

Cell Number		1	2	5	8	10	12	15
Earth Incidence Angle Deg. / Wind Speed m/sec.		24°	29°	41°	51°	56°	60°	66°
3	σ^o(dB)	-18	-23	-26	-29	-30	-30	-30
	$\frac{\Delta\sigma^o}{\sigma^o}$,%	111	98	31	59	117	193	444
4	σ^o(dB)	-16	-21	-24	-27	-28	-28	-28
	$\frac{\Delta\sigma^o}{\sigma^o}$,%	70	62	20	38	74	122	281
6	σ^o(dB)	-14	-18	-21	-23	-24	-24	-24
	$\frac{\Delta\sigma^o}{\sigma^o}$,%	45	32	11	16	31	50	114
12	σ^o(dB)	-9	-12	-15	-18	-19	-19	-19
	$\frac{\Delta\sigma^o}{\sigma^o}$,%	15	9	4	6	11	18	38
24	σ^o(dB)	-4	-6	-9	-12	-13	-13	-13
	$\frac{\Delta\sigma^o}{\sigma^o}$,%	5	3	2	3	5	6	12
48	σ^o(dB)	0	-1	-3	-6	-7	-7	-7
	$\frac{\Delta\sigma^o}{\sigma^o}$,%	2.6	1.6	1.5	2	3	4	5

K_p

θ_p = 42°

P_T = 125 watts

ant. Bw = .5° x 25°

t_p = 1.891 sec

T = 26.8 msec

τ_{SN} = 352.8 msec

τ_N = 705.5 msec

r = 50 km

S_s = 100 km

altitude = 808 km

Table VI-Geometric Parameters and Minimum σ^o and Wind speeds for 25 km Resolution Design (Cells 1 through 5) - MODE I

50km Cell No.	1		2		3		4		5	
25km Cell	lower	upper	lower	upper	lower	upper	lower	upper	lower	upper
Rg, km	300.5	336.0	371.2	406.7	441.9	477.4	512.6	548.2	583.3	618.9
θ, deg	20.2	22.3	24.7	26.3	28.2	30.0	31.7	33.4	34.9	36.4
θi, deg	22.9	25.4	27.7	30.0	32.2	34.3	36.3	38.3	40.1	41.9
R_c, km	868.7	883.2	899.0	916.1	934.2	953.7	974.0	995.6	1017.8	1041.2
L, km	17.3	17.3	16.29	16.29	15.02	15.02	13.46	13.46	11.58	11.58
B_c, Hz	8404.5	7994.6	7136.4	6740.7	5856.7	5502.2	4625.6	4328.6	3482.9	3250.5
σ^o_{min}, dB	-10.3	-13.6	-16.2	-18.6	-20.4	-22	-23.1	-24.2	-24.6	-25.1
K_p	.5	.5	.5	.5	.5	.5	.5	.5	.5	.5
w/s, m/s	9	6	6	5.5	5	4	4	3.5	3.5	3.5
σ^o_{min}, dB	-13		-18.7		-22.7		-25.2		-26.5	
25 km K_p	.914	.44	.87	.51	.84	.58	.79	.63	.76	.67
50 km K_p	.5		.5		.5		.5		.5	
w/s, m/s	6.5		5		4		3		3	

S_s = 50km

Alt. = 808 km

P_T = 125 w

t_p = 1.891s

τ_{SN} = 352.8 ms

TABLE VII - Geometric Parameters and Minimum σ^o and Wind speeds for 25 km Resolution Design (Cells 5 through 10)
MODE I

50 km Cell No.	6		7		8		9		10	
25 km Cell	lower	upper	lower	upper	lower	upper	lower	upper	lower	upper
R_g, km	654.9	688.7	726.6	758.5	798.4	828.1	870.4	897.5	942.5	966.8
θ, deg	37.8	39.1	40.5	41.6	42.9	43.8	45	45.8	46.9	47.5
θ_i, deg	43.7	45.3	47	48.4	50	51.2	52.8	53.8	55.4	56.2
R_c, km	1065.7	1089.4	1116.7	1140.3	1165.5	1193.5	1226.8	1248.6	1285.3	1305.4
L, km	11.27	11.27	10.64	10.64	9.9	9.9	9.1	9.1	8.1	8.1
B_c, Hz	2947.6	2756.7	2413.3	2263.9	1944.5	1832	1547.2	1465.7	1193	1137.1
σ^o_{min} dB	-25.5	-25.7	-25.6	-25.6	-25.8	-25.0	-24.4	-24.1	-23.2	-22.9
K_p	.5	.5	.5	.5	.5	.5	.5	.5	.5	.5
w/s, m/s	3.5	4	4	4.5	5	5	5.5	6	7	7.5
σ^o_{min} dB	-27.2		-27.2		-27.0		-25.9		-24.7	
25 km K_p	.725	.694	.704	.715	.647	.776	.695	.745	.691	.745
50 km K_p	.5		.5		.5		.5		.5	
w/s, m/s	3		3.5		4		5		6	

Table VIII Geometric Parameters, Link Parameters and Minimum σ^o Measurements for Mode II (Option I)

Cell No.	R_g, km	θ, deg.	θ_i, deg.	R_c, km	On Gate, ms	f_D, hz	B_c, hz	KT_sB_c watts	$B_c\tau_{SN}$	$(G/G_o)^2$ dB	S/N dB	σ^o dB
1	0.0	0.0	0.0	808	5.39	0.0	21367	3.2×10^{-16}	15076	-26.7	-17	0
2	31.31	2.21	2.5	808.7	5.40	26740	21312	3.2×10^{-16}	15033	-23.9	-16.9	-2.7
3	62.71	4.43	5	811	5.40	53428	21150	3.2×10^{-16}	14923	-21.3	-16.9	-5.2
4	126.2	8.86	10	819	5.45	106446	20511	3.1×10^{-16}	14472	-16.6	-16.9	-10
5	191.2	13.28	15	833	5.54	158657	19481	3×10^{-16}	13746	-12.5	-16.8	-13.9
6	259.2	17.67	20	854	5.67	209661	18111	2.8×10^{-16}	12779	- 9	-16.6	-17.2
7	330.6	22.03	25	881	5.84	259067	16467	2.5×10^{-16}	11619	- 6	-16.3	-19.9
8	406.8	26.34	30	916	6.07	306498	14627	2.2×10^{-16}	10321	- 3.7	-16.1	-22
9	489.5	30.6	35	961	6.36	351604	12674	1.9×10^{-16}	8943	- 2	-15.8	-23.4
10	580.4	34.78	40	1016	6.72	394031	10693	1.6×10^{-16}	7545	- .8	-15.4	-24.2
11	682	38.87	45	1085	7.18	433458	8764	1.3×10^{-16}	6184	- .16	-15	-24.5
12	797.4	42.83	50	1170	7.74	469586	6958	1.1×10^{-16}	4910	- .01	-14.5	-24.1
13	930.7	46.63	55	1276	8.44	502141	5331	8.1×10^{-17}	3762	- .31	-13.8	-23.2
14	1087.3	50.23	60	1408	9.32	530875	3924	6×10^{-17}	2768	- 1.0	-13.2	-21.9
15	1274.3	53.55	65	1574	10.42	555569	2755	4.2×10^{-17}	1944	- 1.9	-12.4	-20.2

$\theta_p = 42.1^o$

$t_p = 3.782$ sec.

$\tau_{SN} = 705.53$ ms

$\tau_N = 1.411$ sec.

BW = $.5^o\times40^o$

$K_p = .5$

L = 25 km

Remaining Parameters same as Mode I

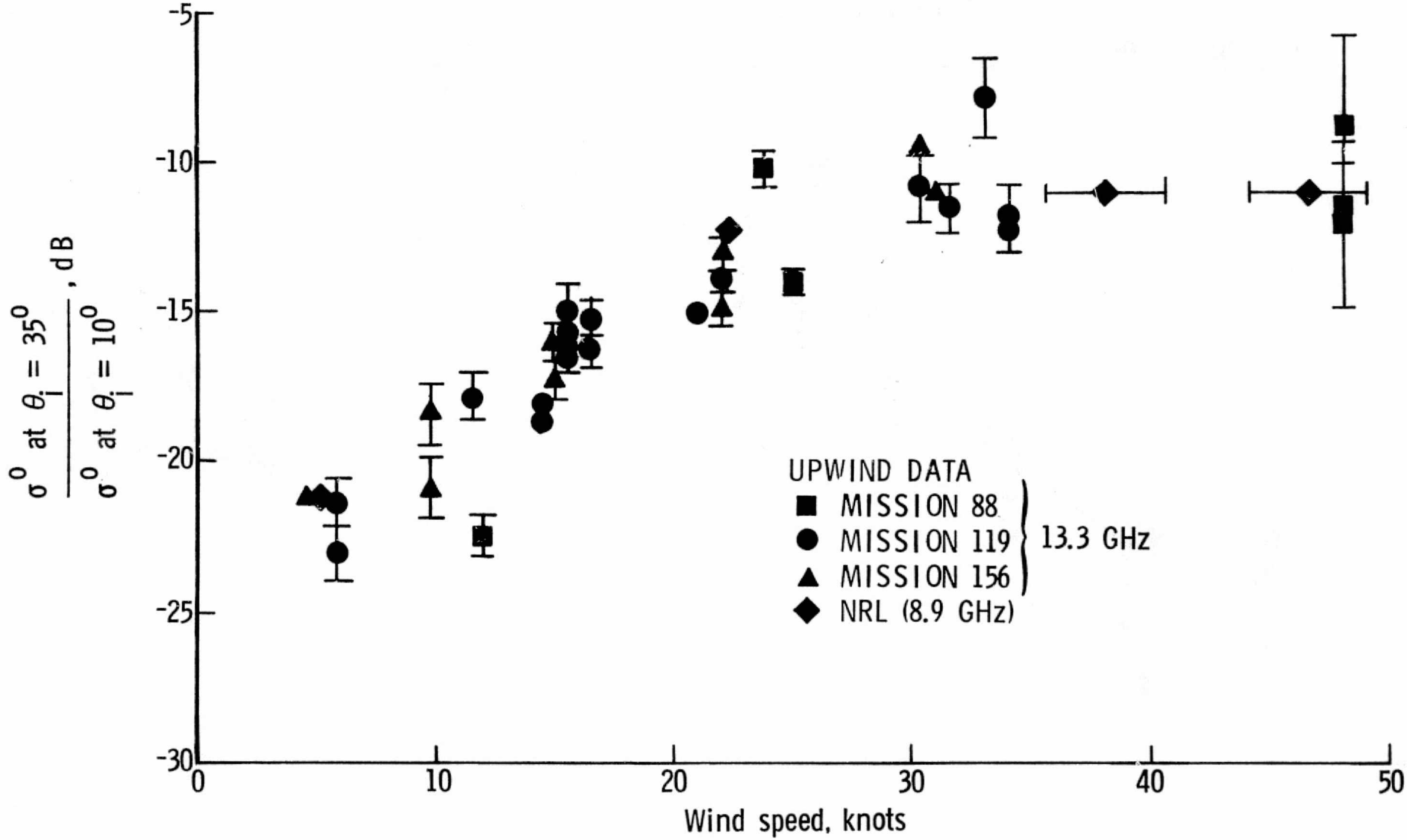

Figure 1.- Normalized scattering coefficient data from JSC and NRL (log-linear plot).

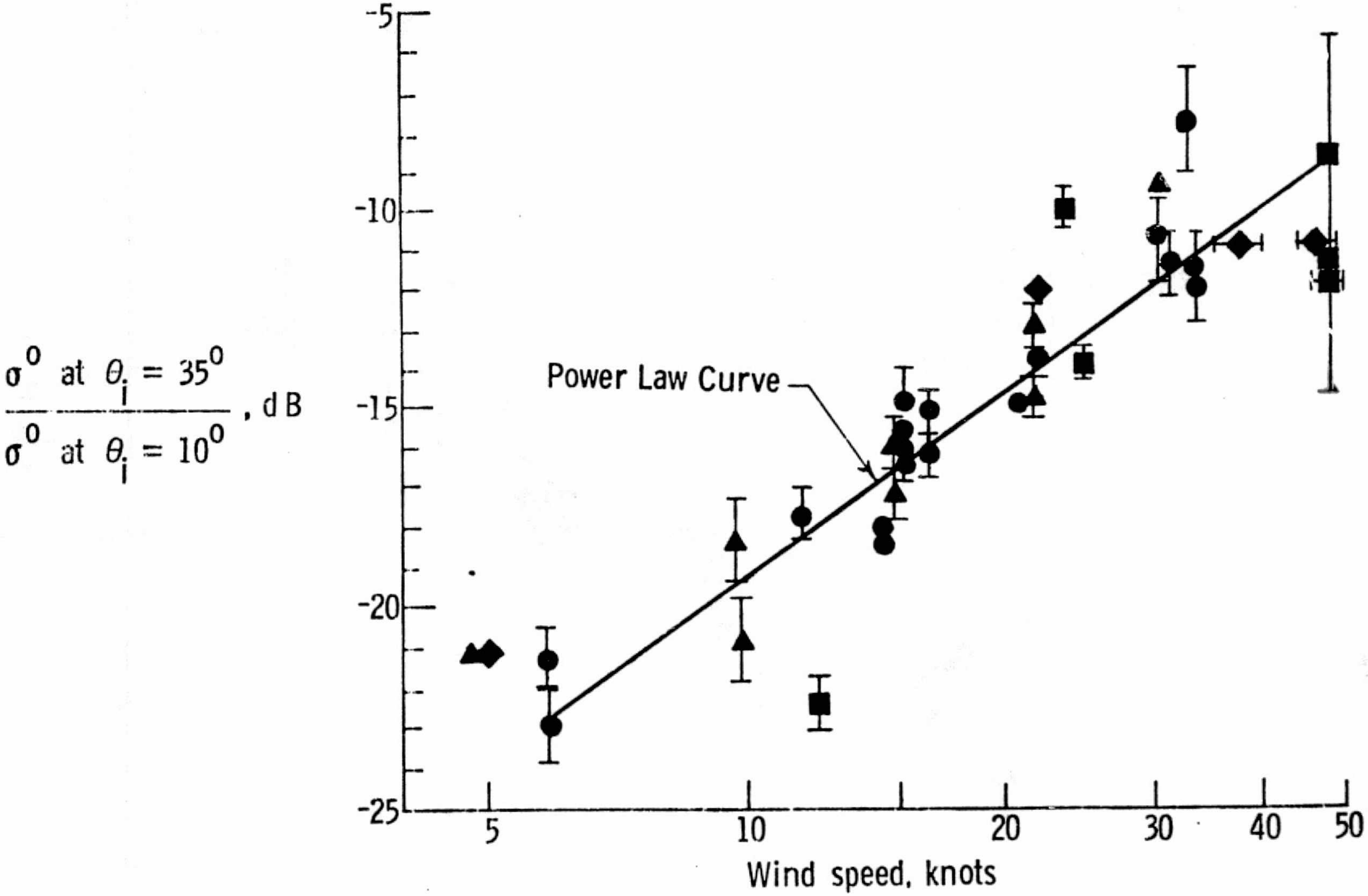

Figure 2. - Normalized scattering coefficient data from JSC and NRL (log - log plot).

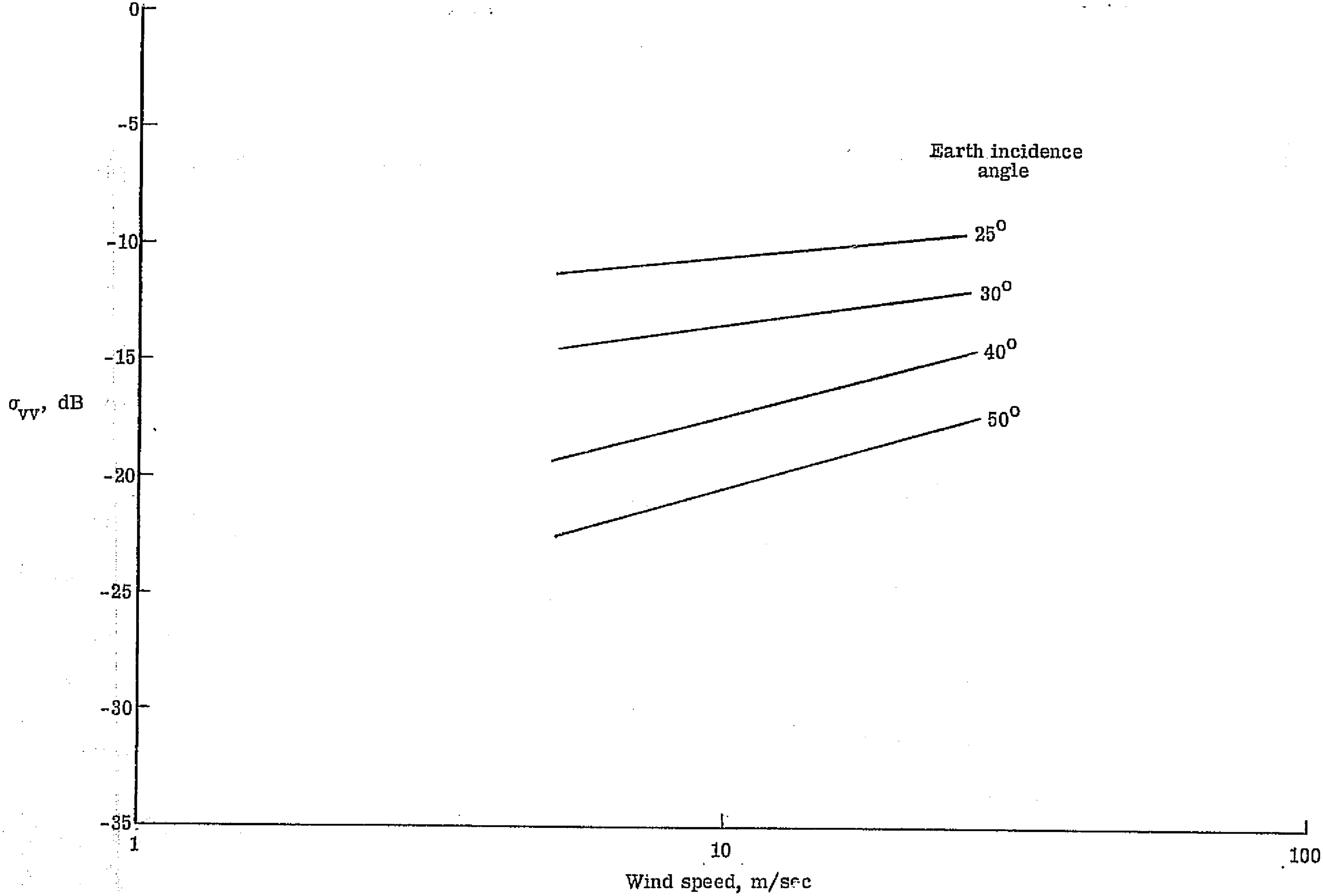

(a) Vertical polarization.

Figure 3.- Upwind 8.9 GHz NRL σ^0 versus wind speed (data from reference 20).

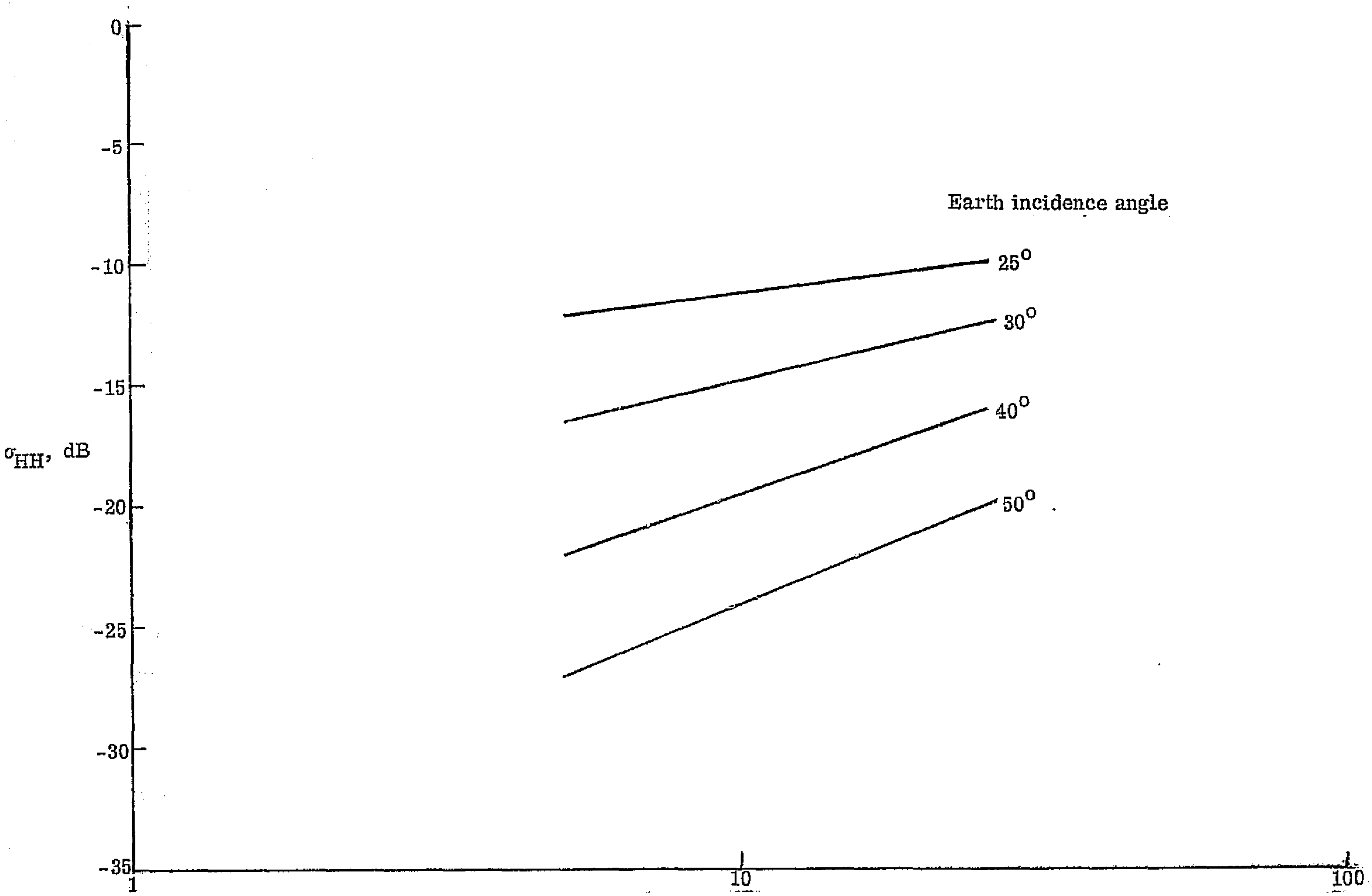

(b) Horizontal polarization.

Figure 3.- Concluded.

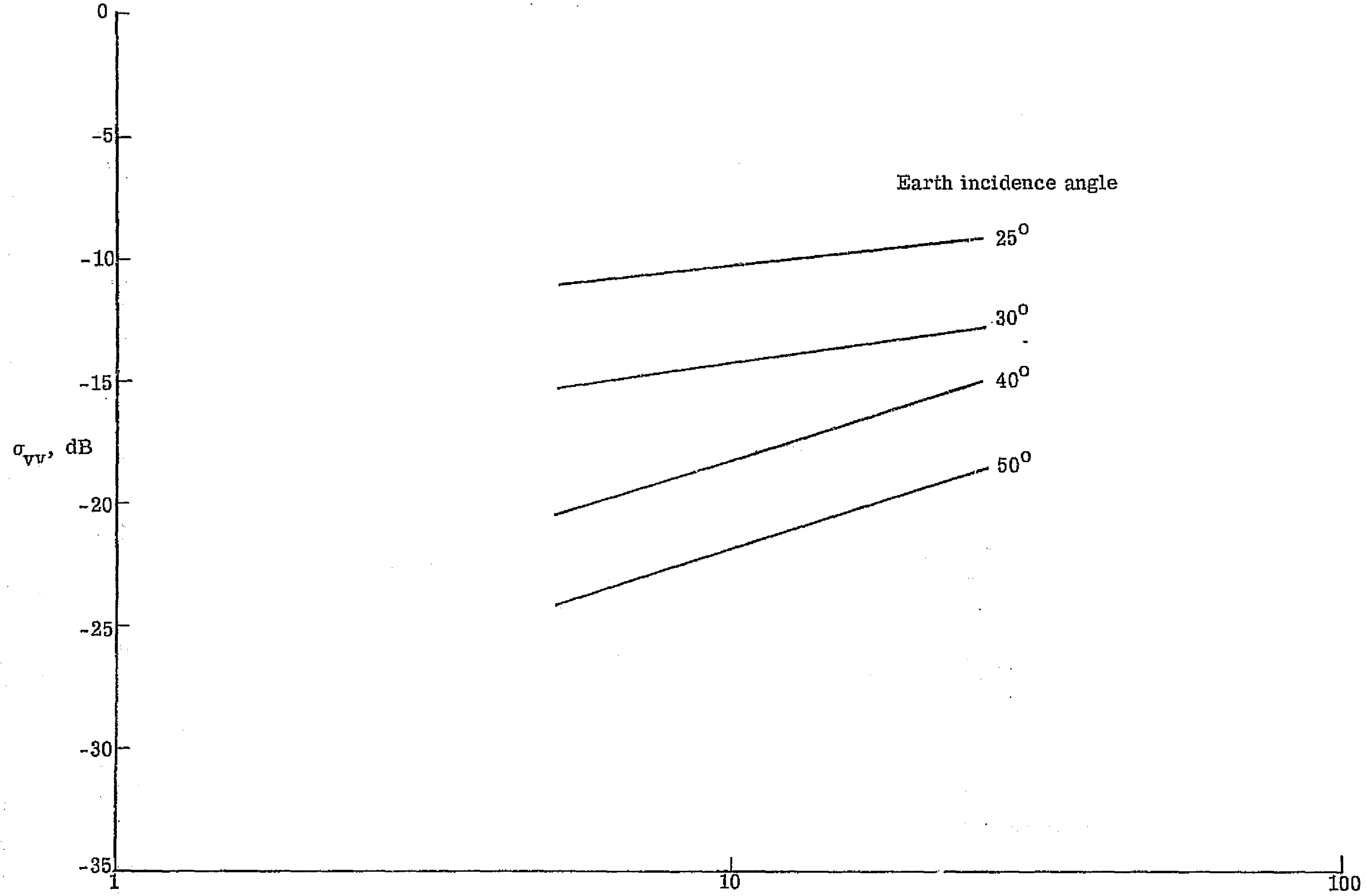

(a) Vertical polarization.

Figure 4.- Downwind 8.9 GHz NRL σ^{o} vs. wind speed (data from reference 20).

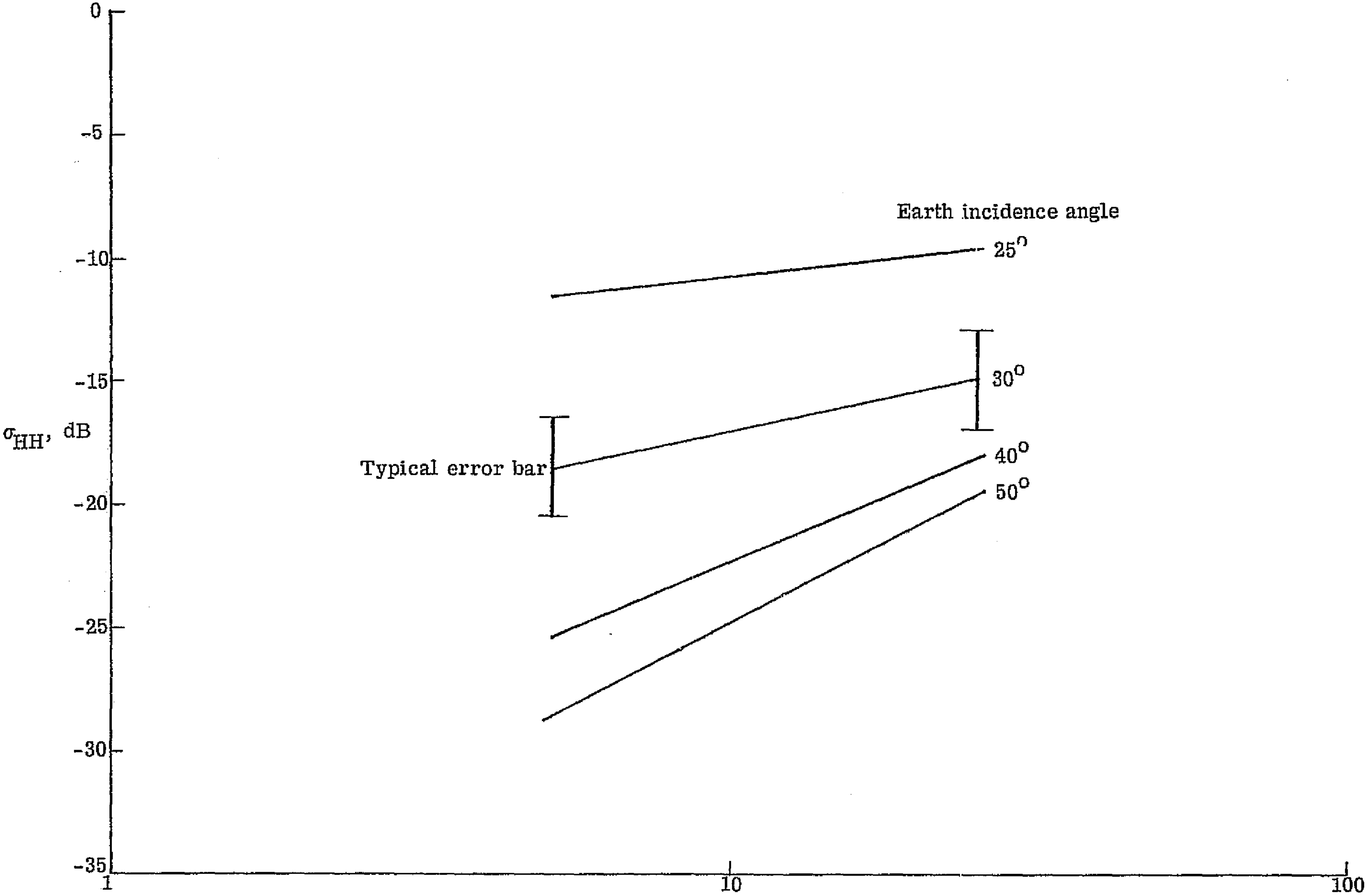

(b) Horizontal polarization.

Figure 4.- Concluded.

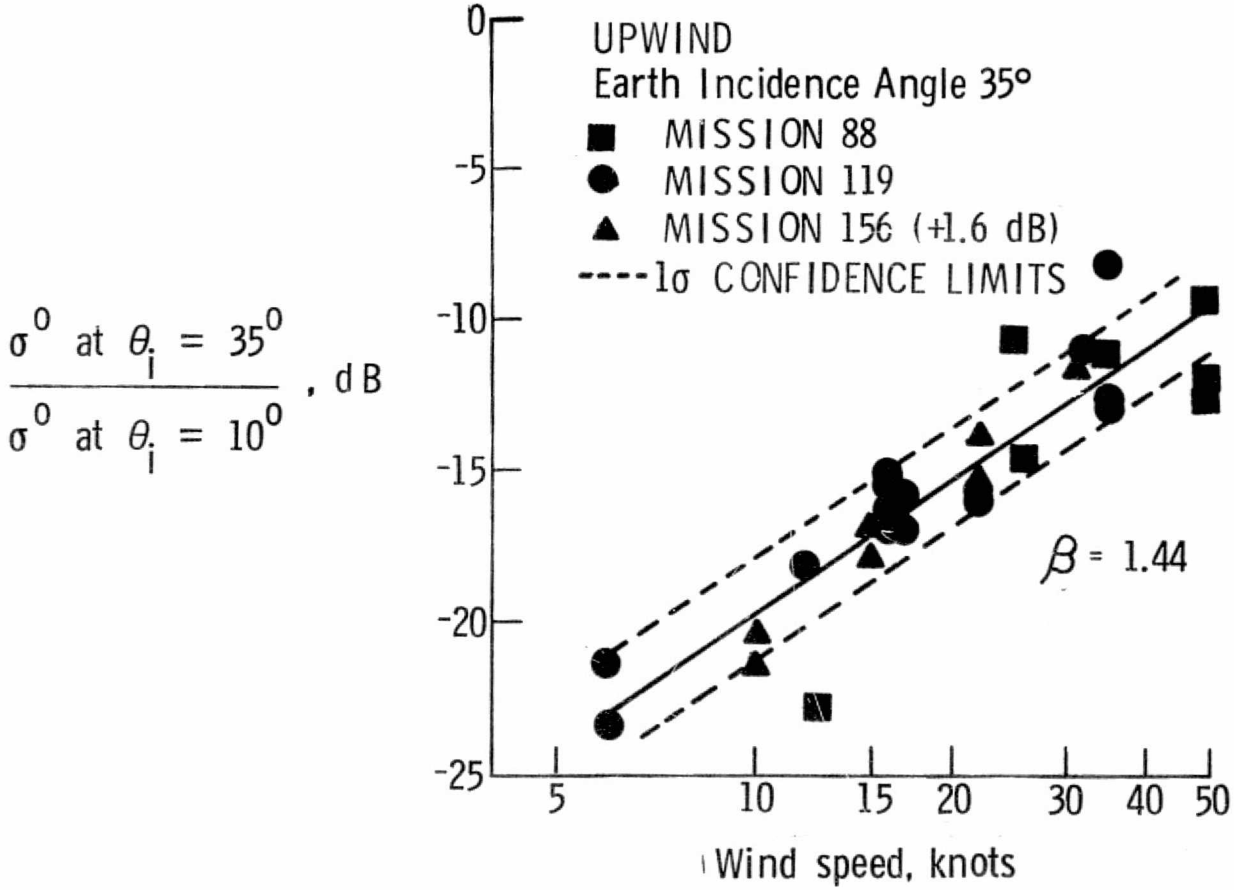

Figure 5.- Upwind JSC normalized scattering coefficient vs. wind speed.

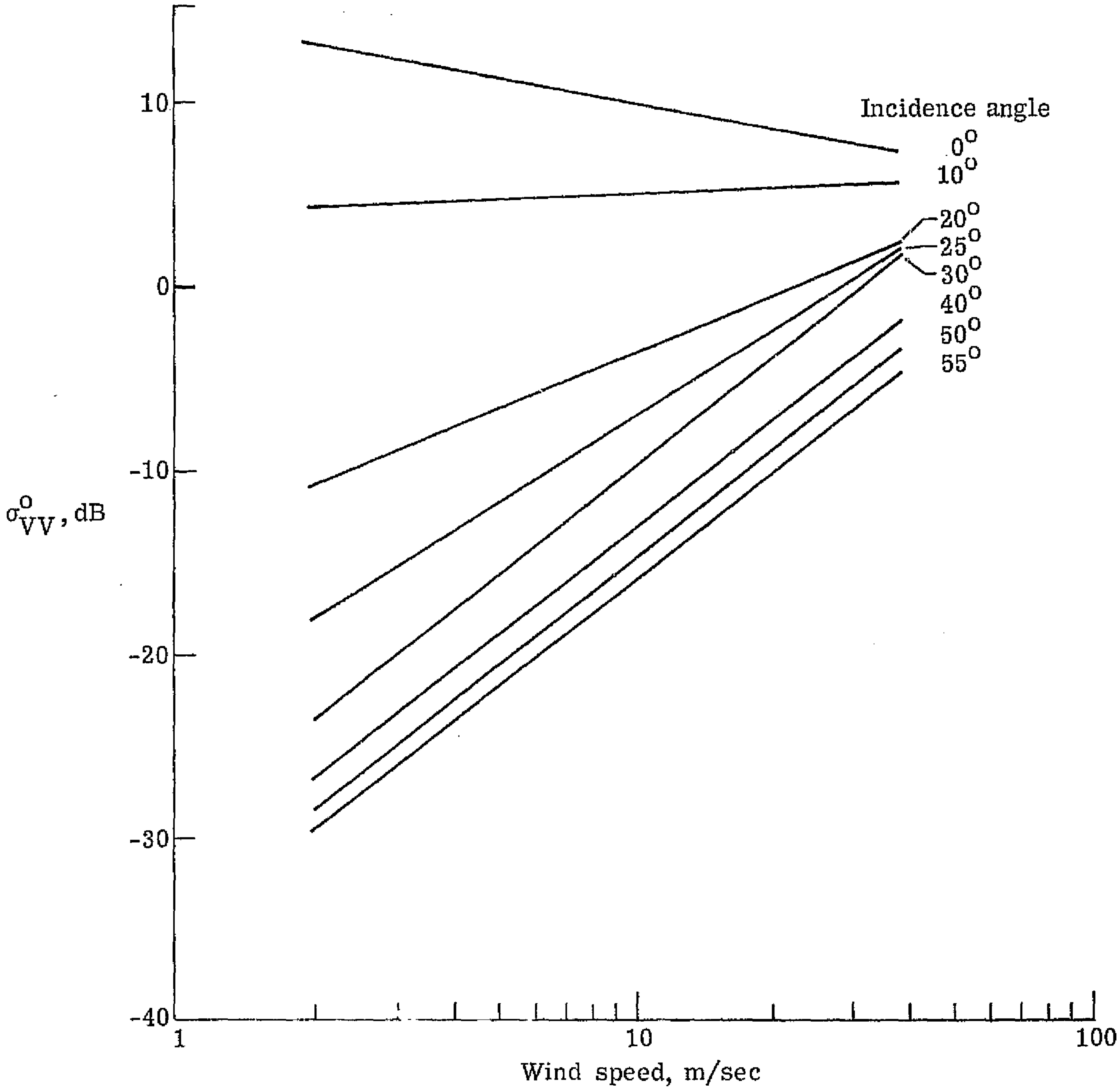

(a) Upwind.

Figure 6.- AAFE Radscat σ^o_{VV} vs. wind speed.

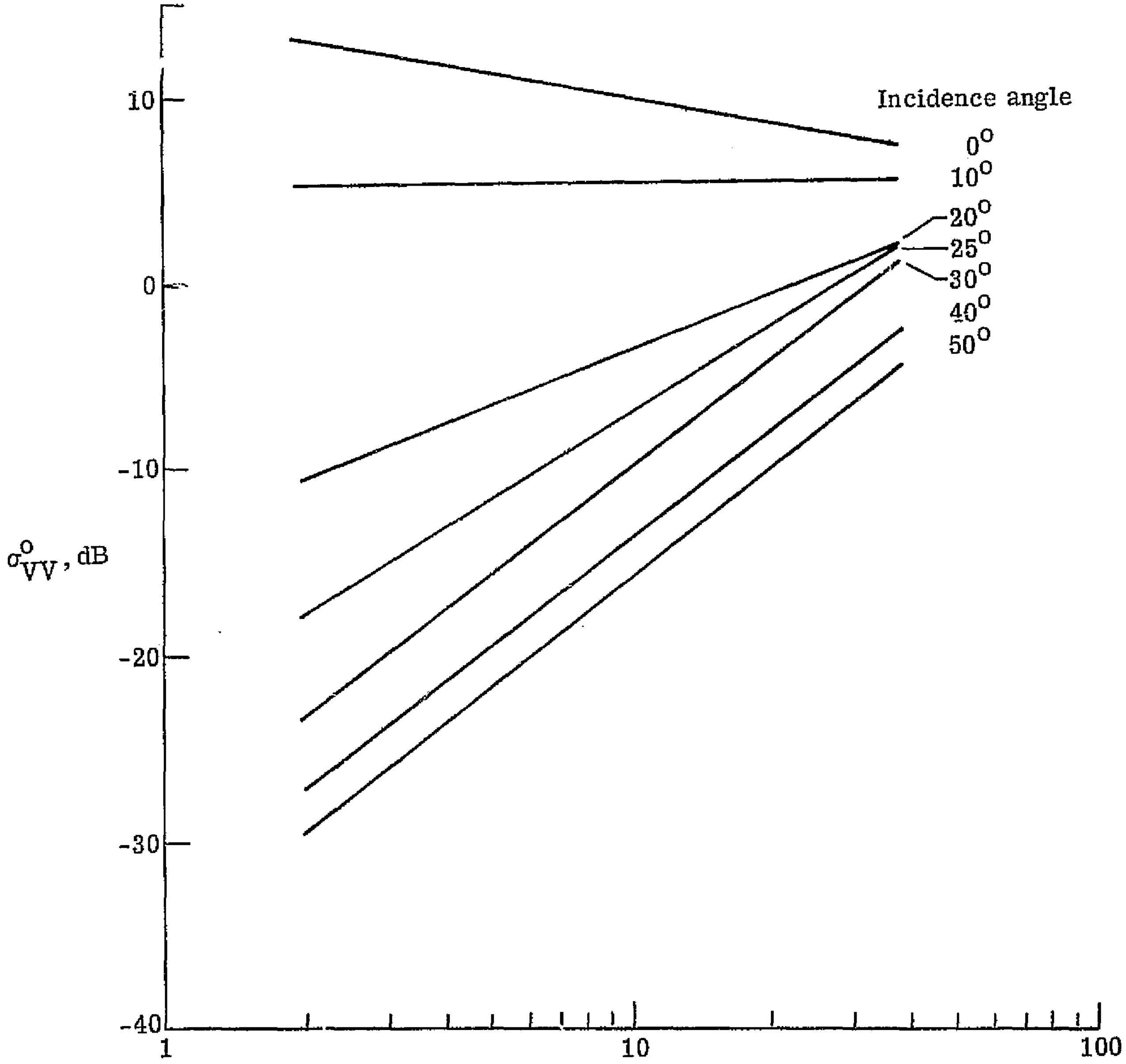

(b) Downwind.

Figure 6.- Continued.

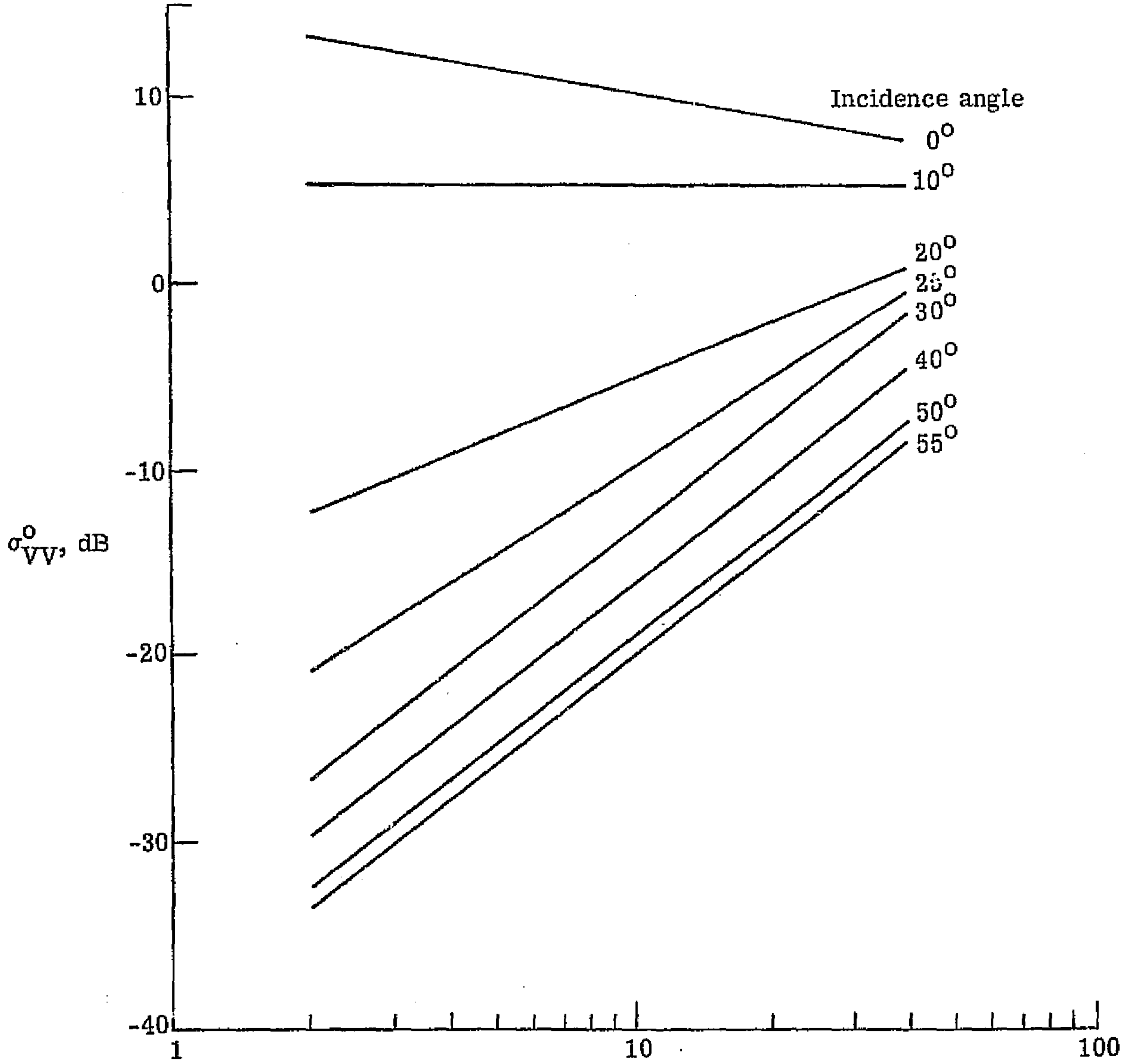

Wind speed, m/sec

(c) Crosswind.

Figure 6.- Concluded.

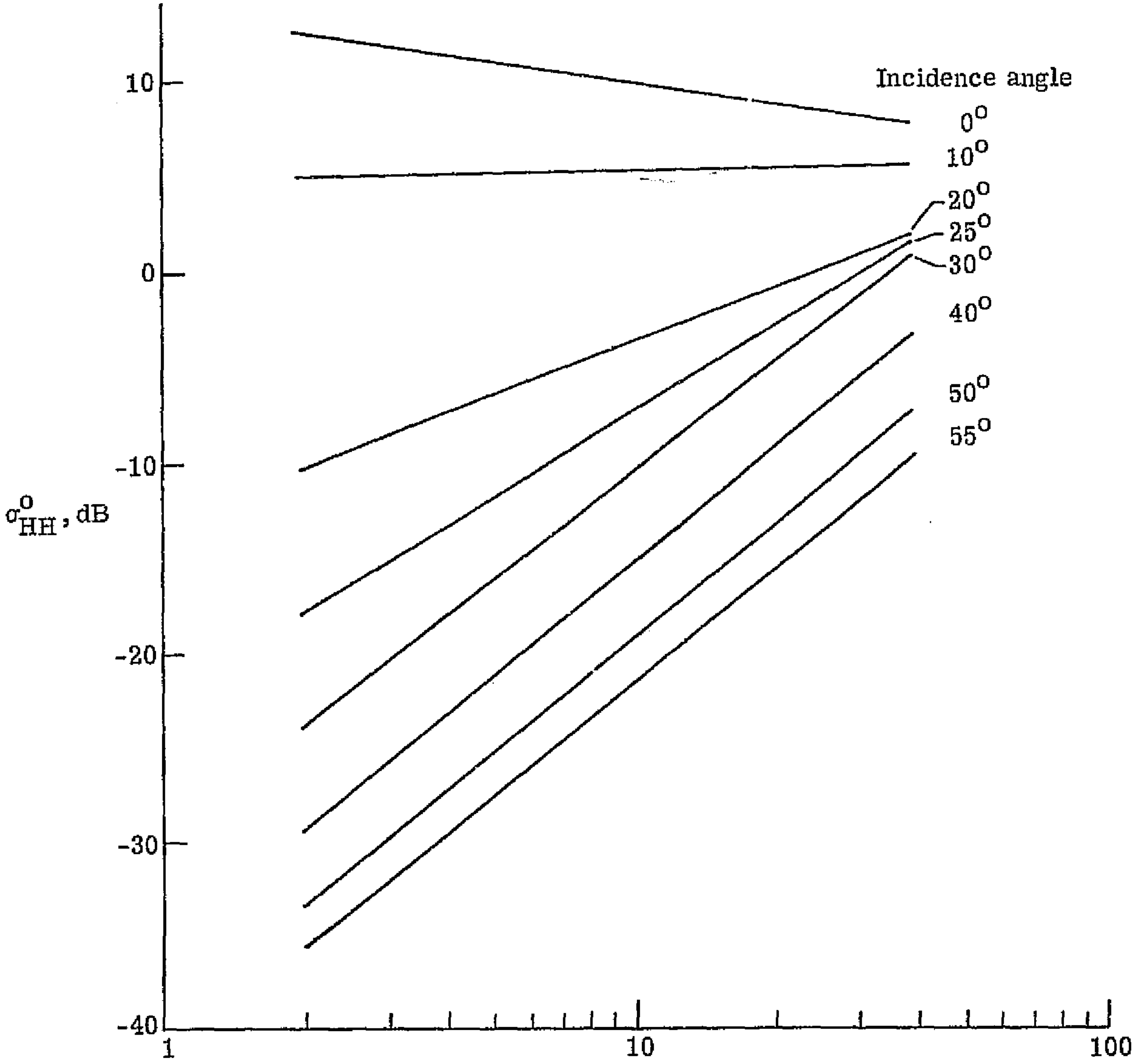

(a) Upwind.

Figure 7.- AAFE Radscat σ^{o}_{HH} vs. wind speed.

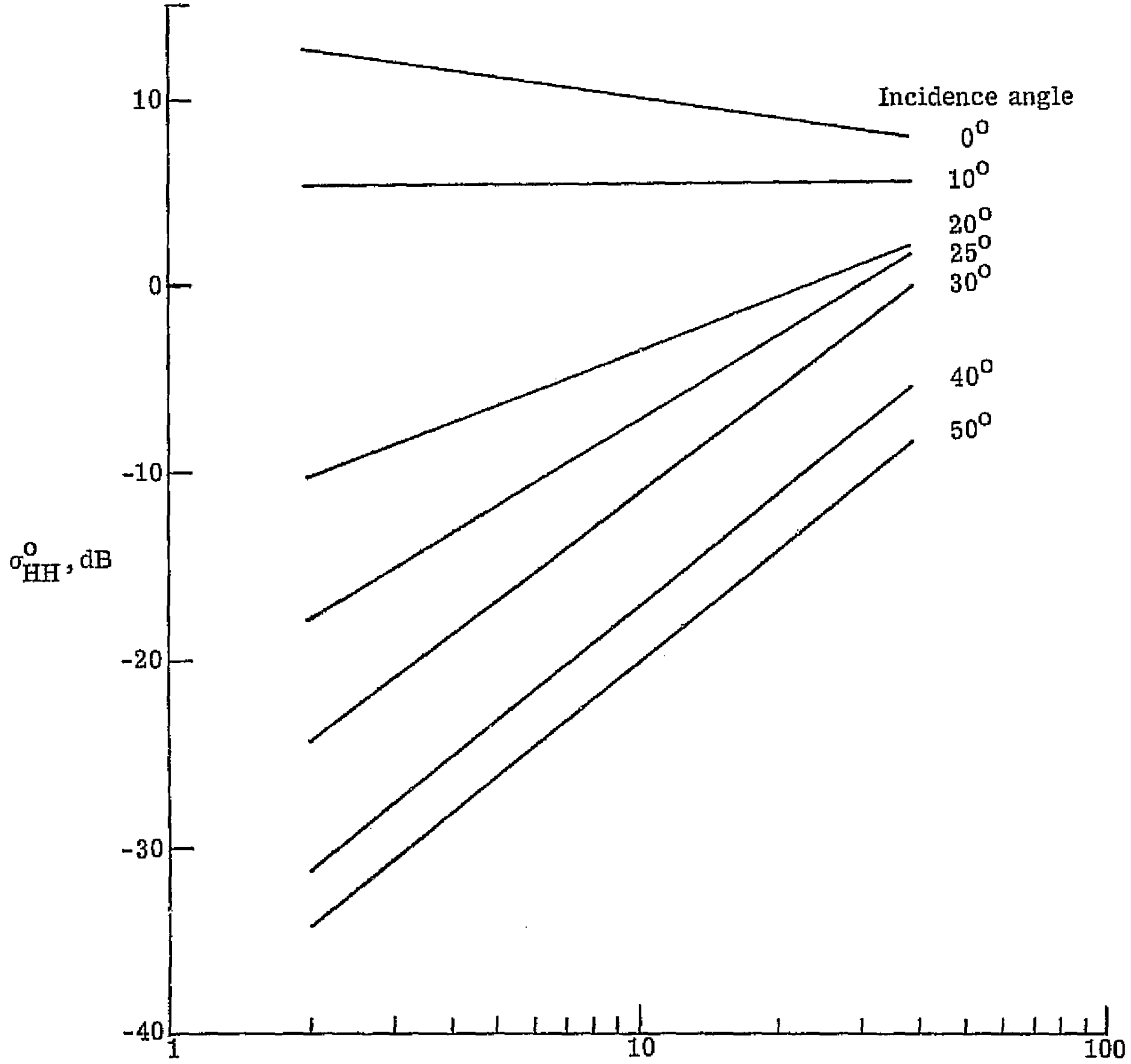

(b) Downwind.

Figure 7.- Continued.

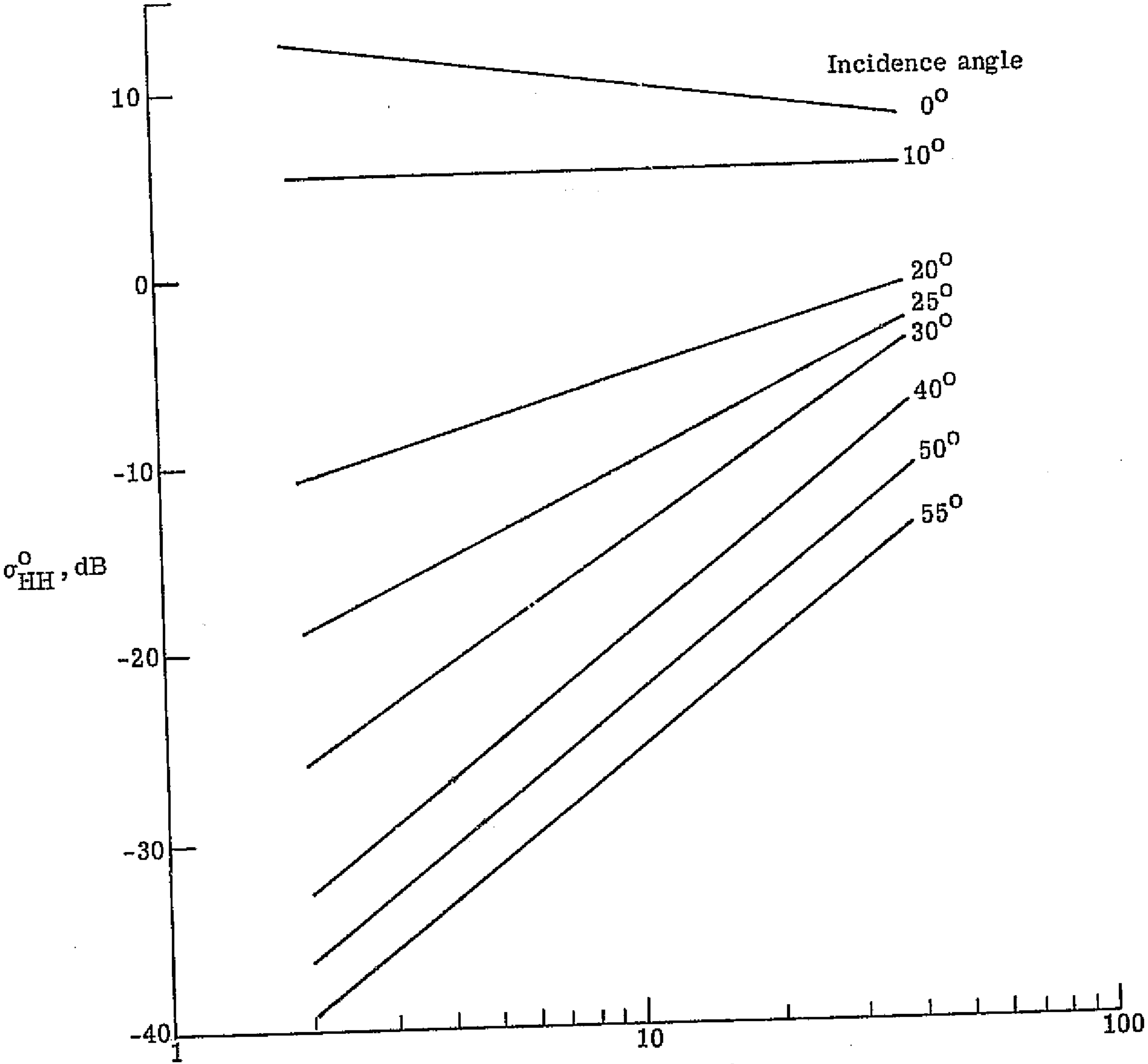

(c) Crosswind.

Figure 7.- Concluded.

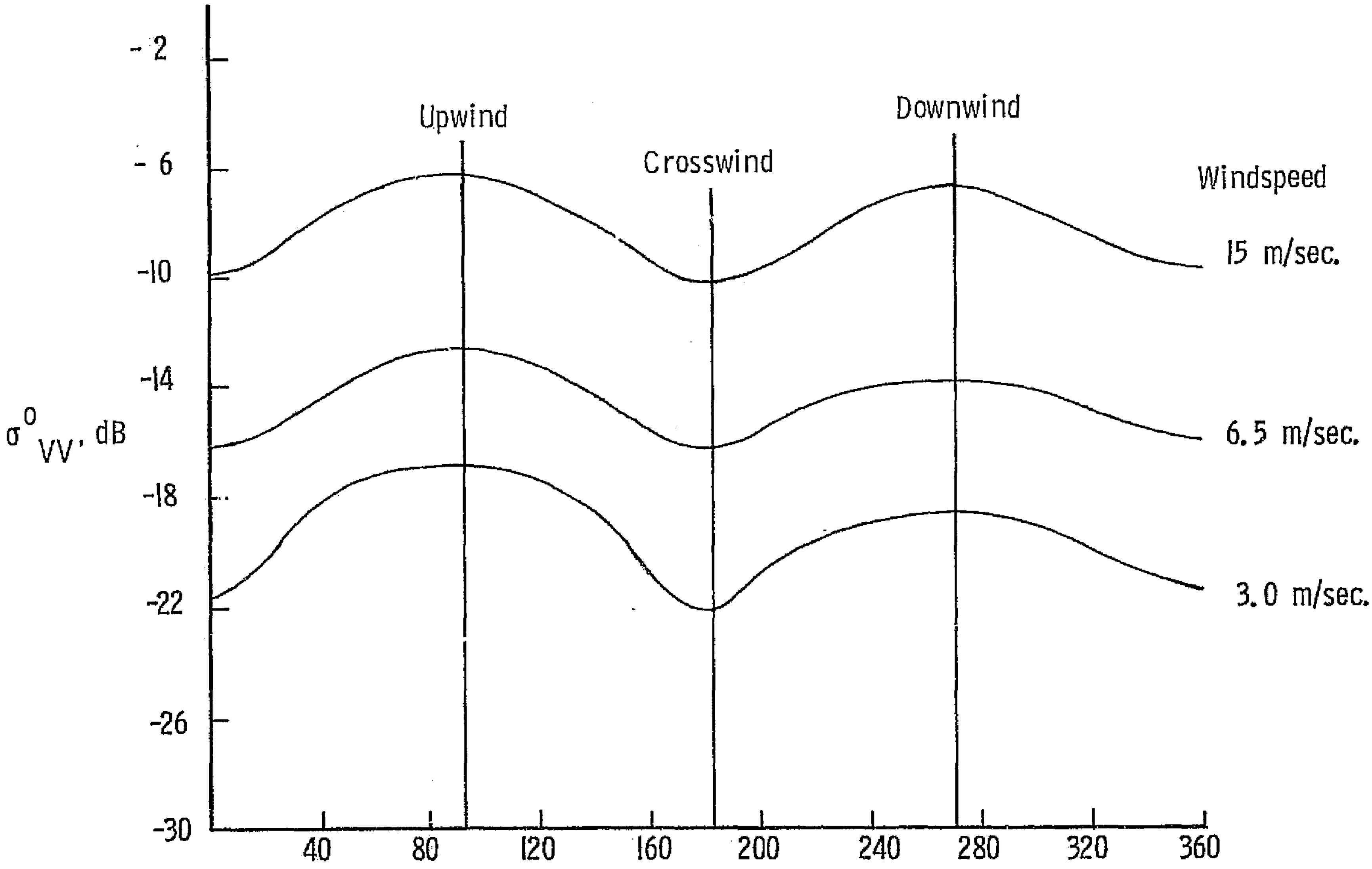

Figure 8. - AAFE Radscat Scatterometer wind direction sensitivity.

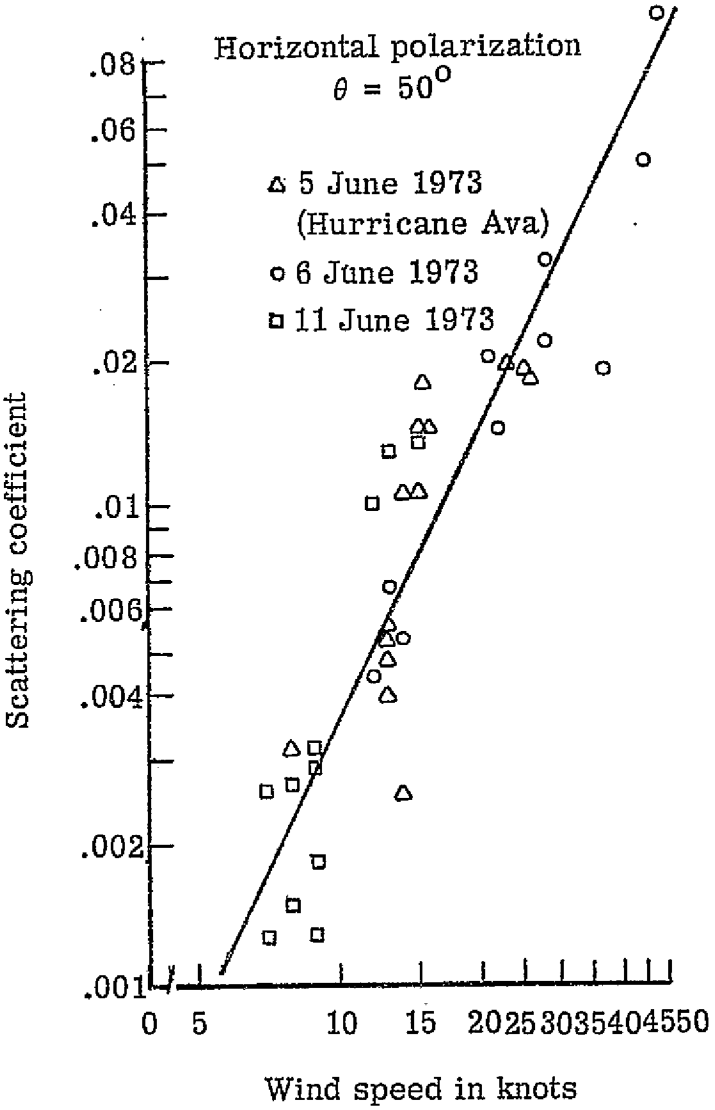

Figure 9.- Skylab S-193 Scatterometer response to wind at sea (from congressional presentation by Dr. R. K. Moore, Feb. 20, 1974).

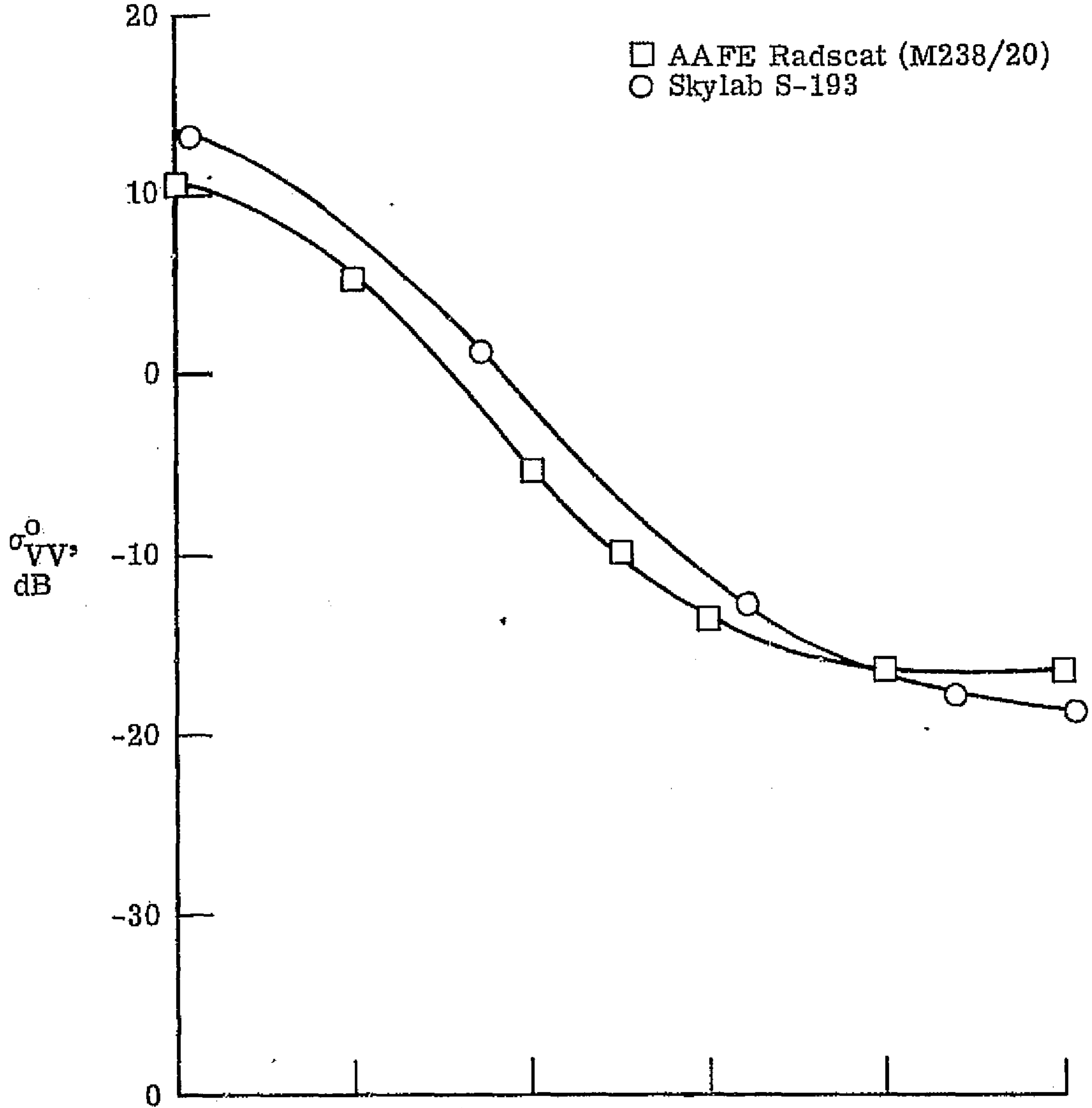

(a) Vertical polarization.

Figure 10.- Comparison of AAFE Radscat with Skylab S-193 data. June 5, 1973 pass, Gulf of Mexico, 13 knot winds, upwind.

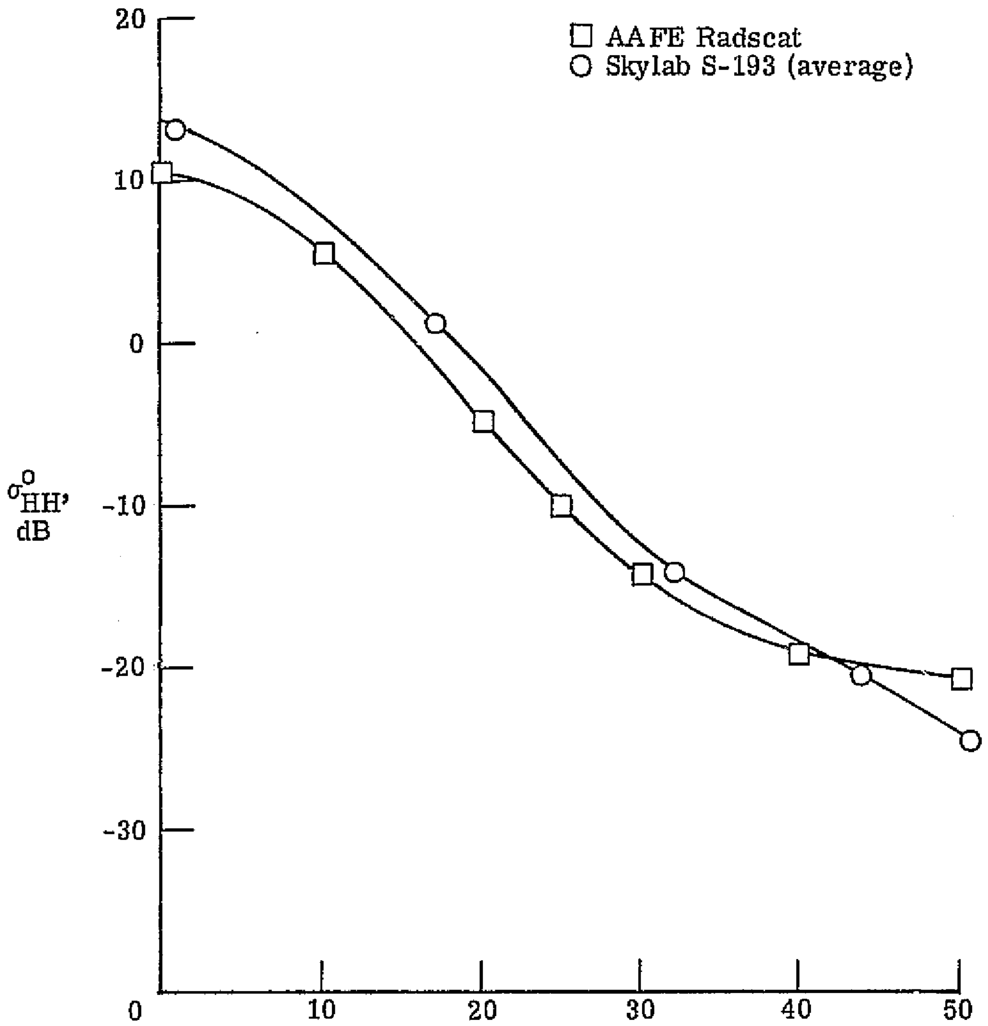

Incidence angle, degrees

(b) Horizontal polarization.

Figure 10.- Concluded.

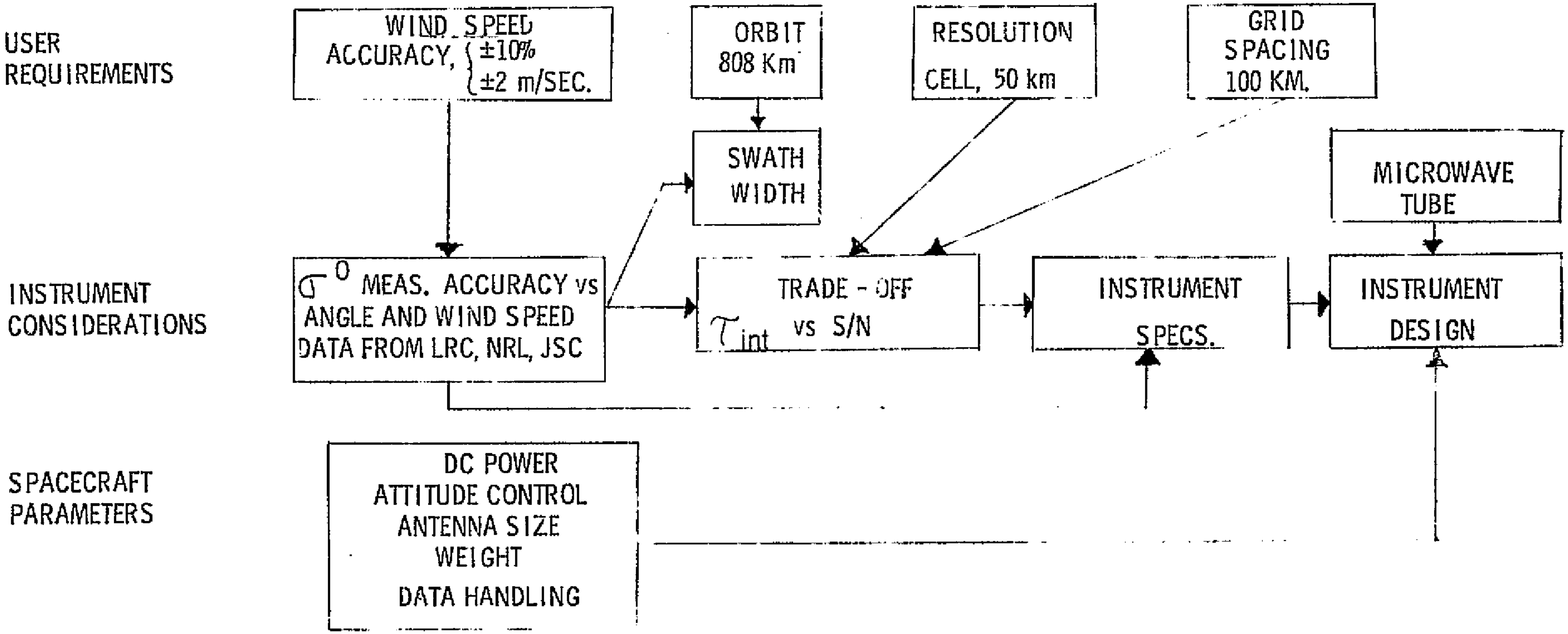

Figure 11. DEVELOPMENT OF SCATTEROMETER SPECIFICATIONS

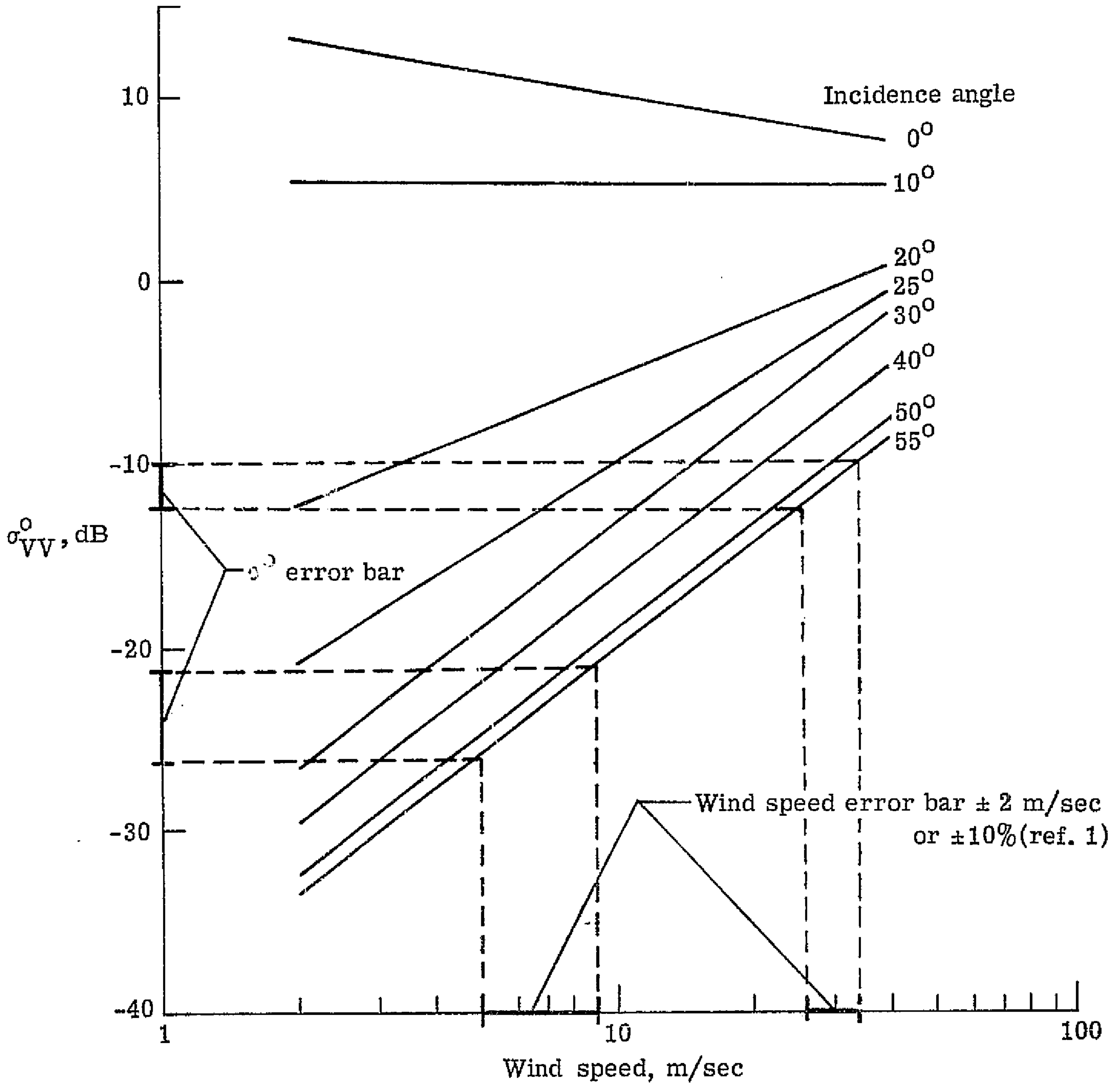

Figure 12.- Wind speed dependence of σ^o_{VV} (crosswind AAFE Radscat data).

INCIDENCE ANGLE WIND SPEED m/sec	10°	20°	25°	30°	40°	50°	55°
4	5 1%	-9 50%	-16 50%	-21 50%	-24 50%	-27 50%	-28 50%
6	5 1%	-8 34%	-14 50%	-18 50%	-21 50%	-23 50%	-24 50%
12	5 < 1%	-5 16%	-9 29%	-12 35%	-15 32%	-18 32%	-19 32%
24	5 < 1%	-2 10%	-4 18%	-6 20%	-9 20%	-12 20%	-13 20%
* 48	5 1%	2 10%	0 18%	0 18%	-3 20%	-6 20%	-7 22%

σ^{o}_{VV} (dB)
K_p x 100

* These values are determined from extrapolation of σ^{0}_{VV} curves beyond the 3 m/sec to 26 m/sec data range.

Figure 13.- Required σ^{0}_{VV} accuracy for scatterometer wind speed accuracy of ± 2 m/sec or ± 10 percent.

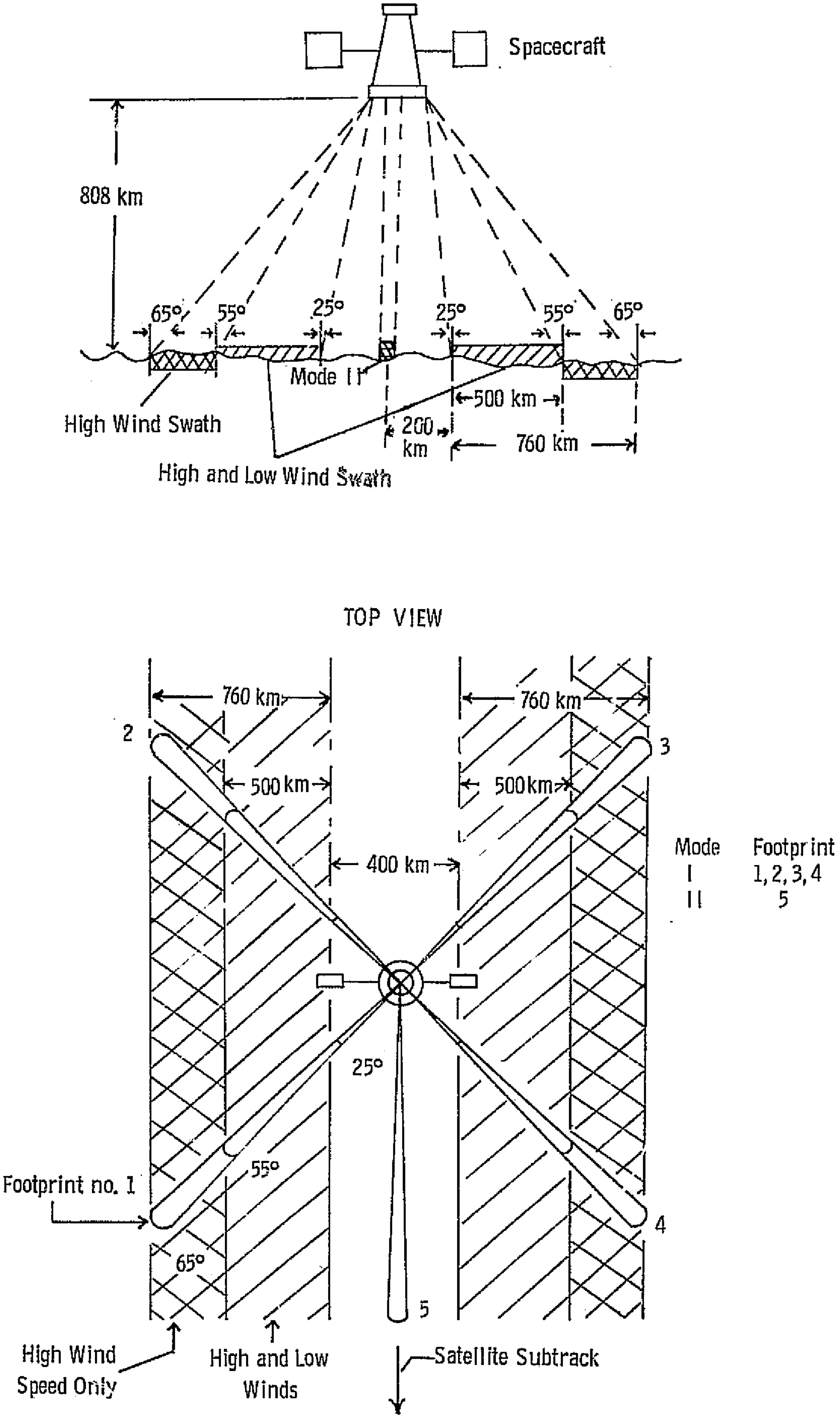

Figure 14.- Scatterometer fan beam geometry.

- Operating Frequency Band 14.5 - 14.9 GHz
- Scattering Cross Section
- σ^0 Normalized Standard Deviation

Earth Incidence Angle / m/sec. wind Speed	Scatterometer Parameters	25°	30°	40°	50°	55°	60° Note 1	65° Note 1
4	σ^0 K_px100	-16 50%	-21 50%	-24 50%	-27 50%	-28 50%	-28 50%	-28 50%
6	σ^0 K_px100	-14 50%	-18 50%	-21 50%	-23 50%	-24 50%	-24 50	-24 50%
12	σ^0 K_px100	- 9 29%	-12 35%	-15 32%	-18 32%	-19 32%	-19 32%	-19 32%
24	σ^0 K_px100	- 4 18%	- 6 20%	- 9 20%	-12 20%	-13 20%	-13 20%	-13 20%
48 Note 2	σ^0 K_px100	0 18%	0 18%	- 3 20%	- 6 20%	- 7 22%	- 7 22%	- 7 22%

  - Range of σ^0 Values (See Note 3)

Incidence Angle / Parameter	25°	30°	40°	50°	55°	60° Note 1	65° Note 1
σ^0 Max dB	+7	+6	+3	+2	0	0	0
σ^0 Min dB	-19	-24	-27	-30	-31	-31	-31

  - Maximum σ^0 Bias Error ± 2 dB
  - Resolution Requirement 0.2 dB
- Antenna Requirements (See Note 5)
  - Side Lobe Level -20 dB
  - Azimuth Angles - Two required 90° apart. Data should be timed to cause the two resolution cell centers to overlap.
  - Earth Incidence Angle 25° to 65° (See Note 1)
  - Polarization Options - VV and HH
  - Polarization Purity - 99 percent (At Earth Surface)
  - Cross Polarization level - 20 dB integrated value across the half power beam relative to integrated value of main beam primary polarization.
- Geometric Separation Between σ^0 Measurements
  - Along Track 100 km
  - Cross Track 100 km
- Resolution Cell Size 50 km (including integration smear)

Note 1. The minimum measurable σ^0 value at 60° and 65° is desirable but not mandatory.

Note 2. These values are determined from extrapolation of σ^0_{VV} curves beyond the present data range (3 to 26 m/sec.)

Note 3. The range of values is based on RADSCAT aircraft data (upwind, downwind and crosswind) and has a 3 dB margin at both ends of the σ^0 range.

Note 4. Values are from figure 16a for a crosswind of 4 m/sec.

Note 5. Signal return due to side lobes must be 30 dB below return signal from main beam for that same doppler band.

FIGURE 15 SCATTEROMETER PERFORMANCE SPECIFICATION FOR MODE I

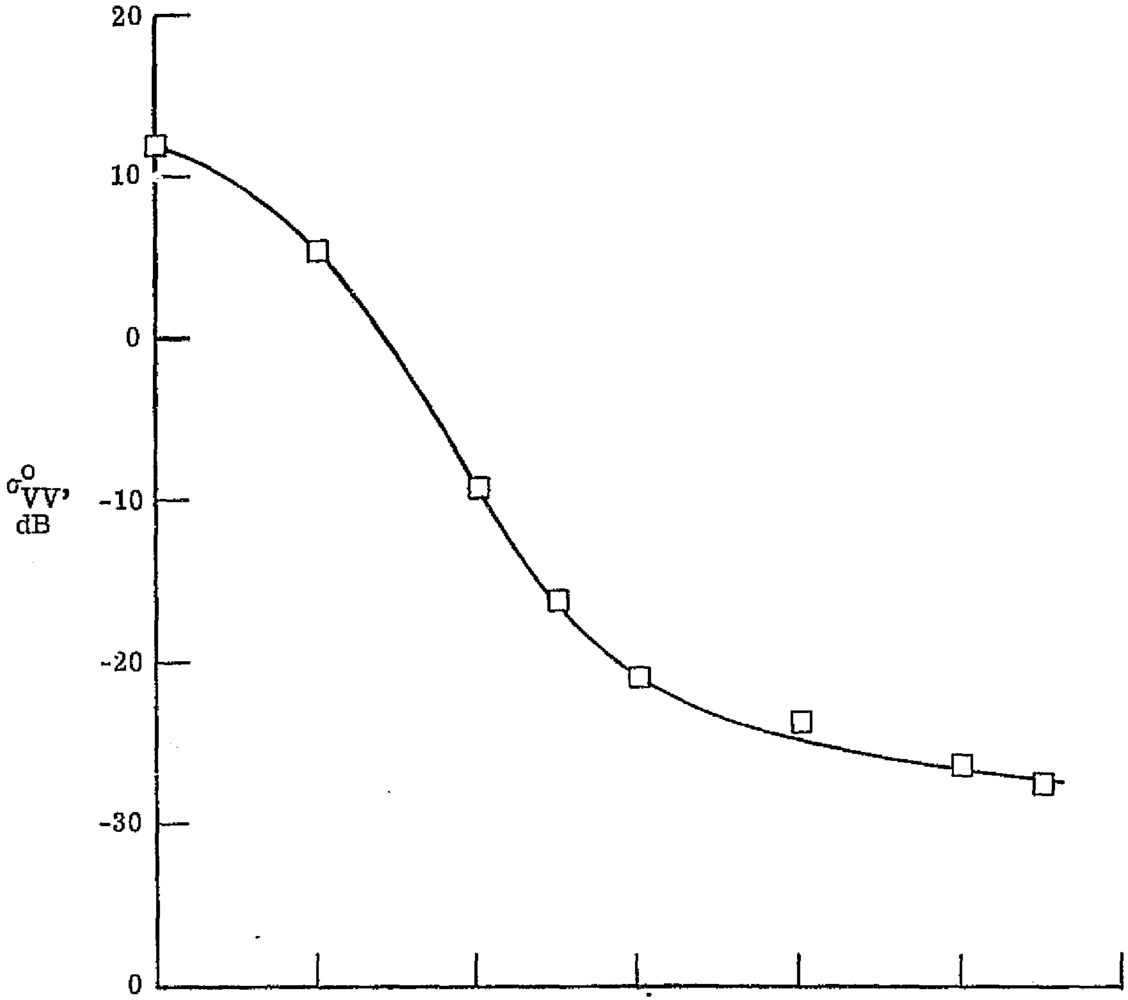

(a) Vertical polarization.

Figure 16.- Scattering coefficient vs. angle of incidence for 4 m/sec wind speed (crosswind).

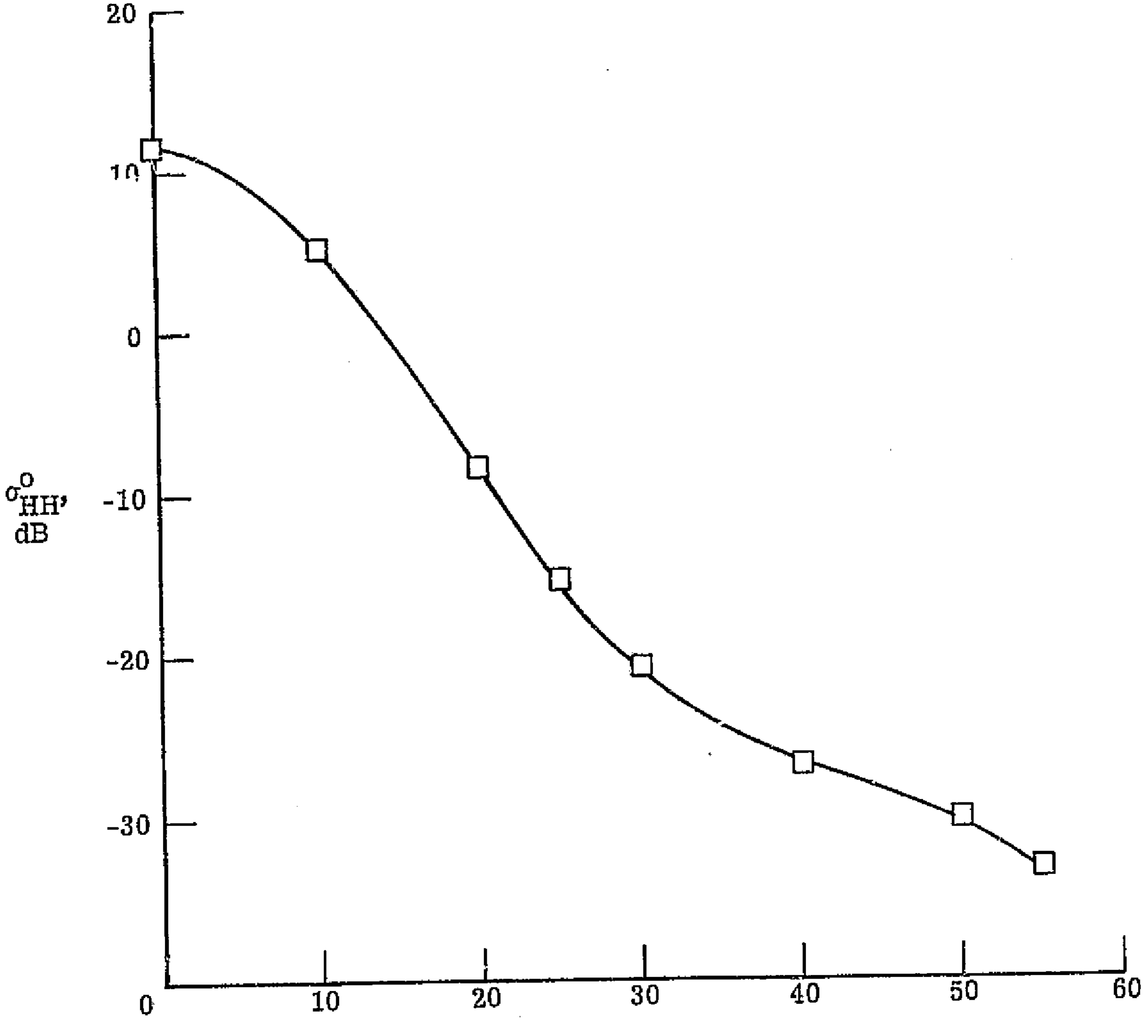

Incidence angle, degrees

(b) Horizontal polarization.

Figure 16.- Concluded.

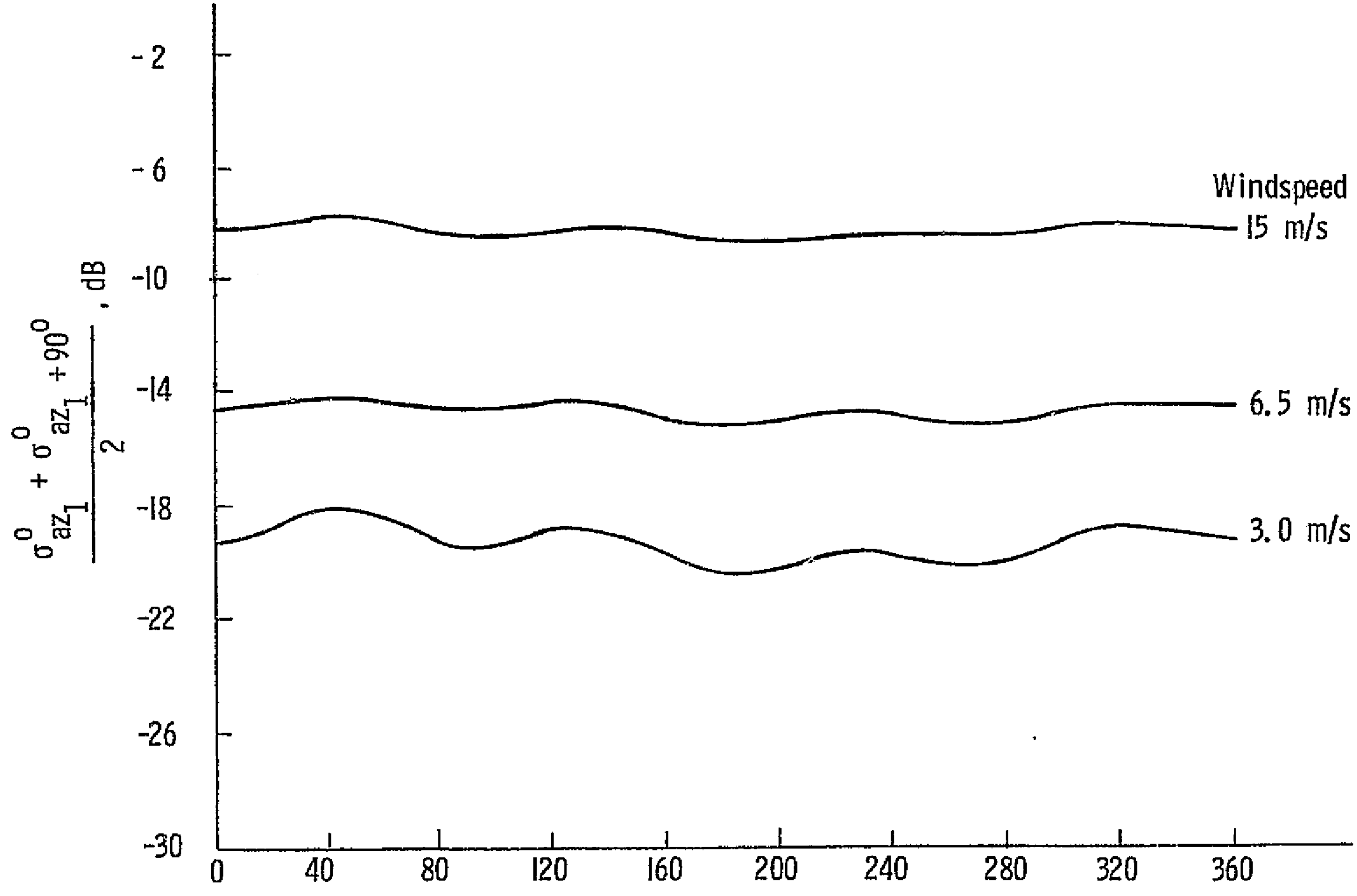

Figure 17.- Mean σ^0_{VV} at two orthogonal wind azimuths. (AAFE Radscat data at 30^0 incidence.

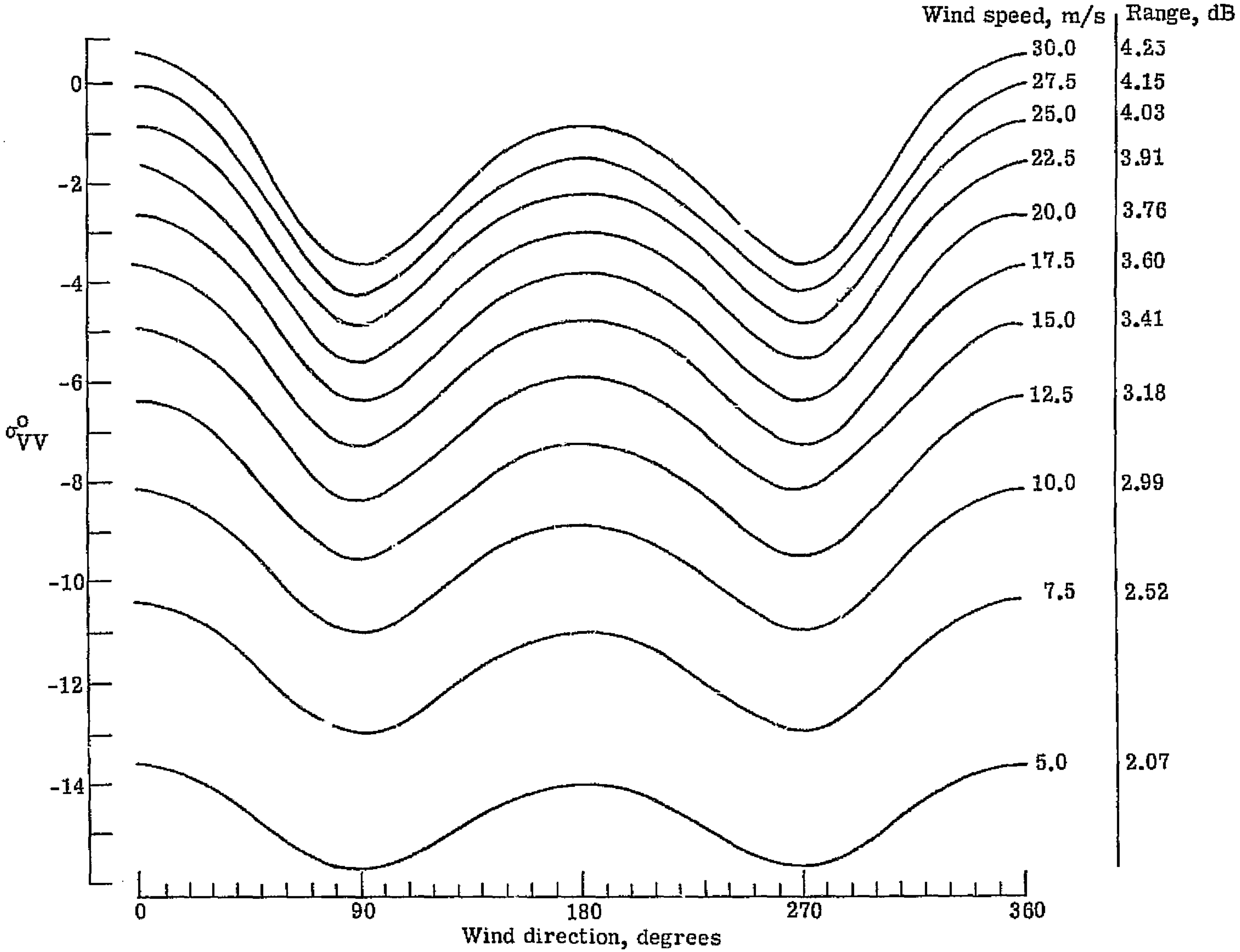

(a) σ^o_{VV} vs. wind azimuth angle.

Figure 18.- Scattering coefficient dependence on wind azimuth angle at $\theta_i = 30^o$ (from reference 26).

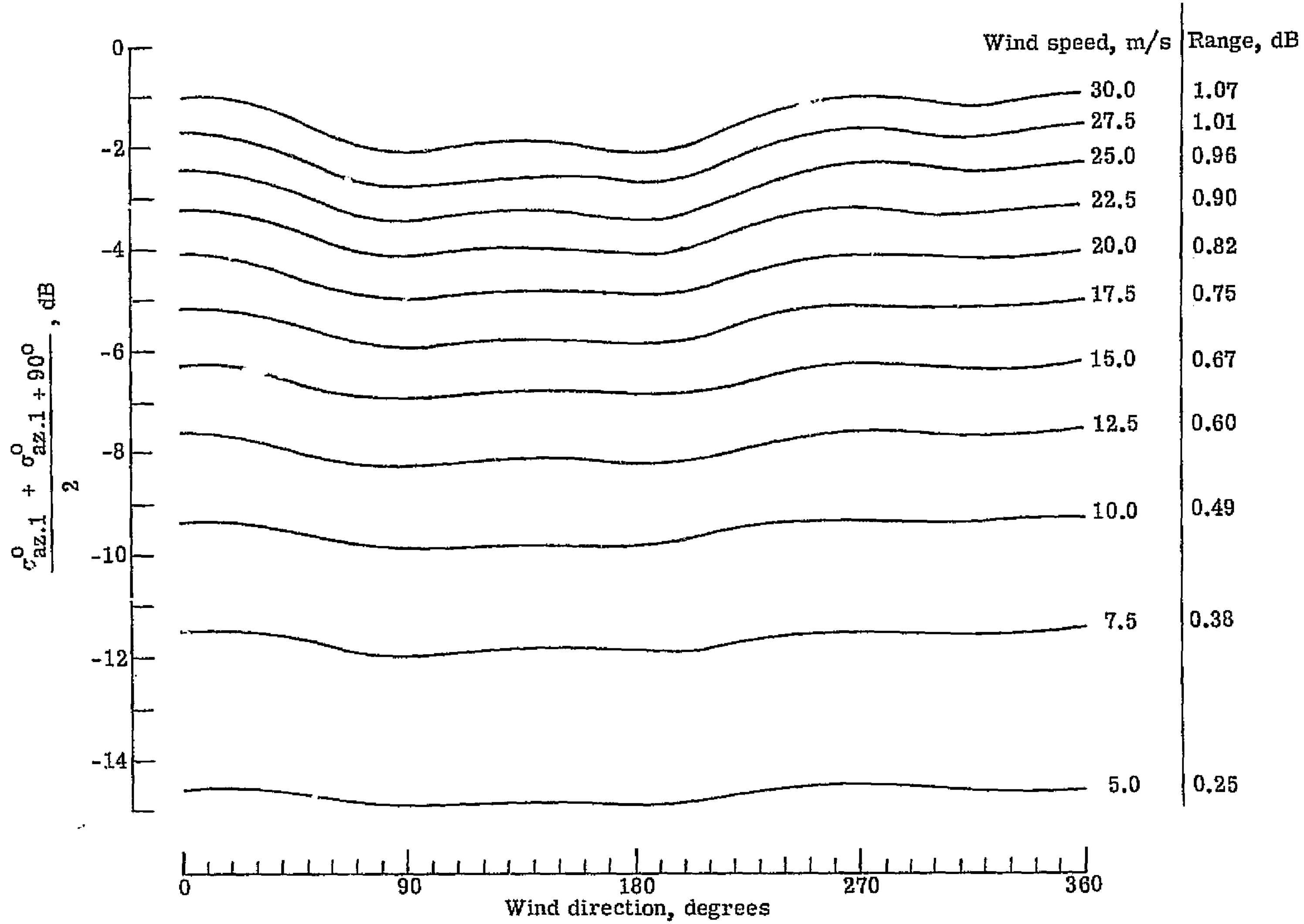

(b) Mean σ^o_{VV} at two orthogonal wind azimuth angles.

Figure 15.- Concluded.

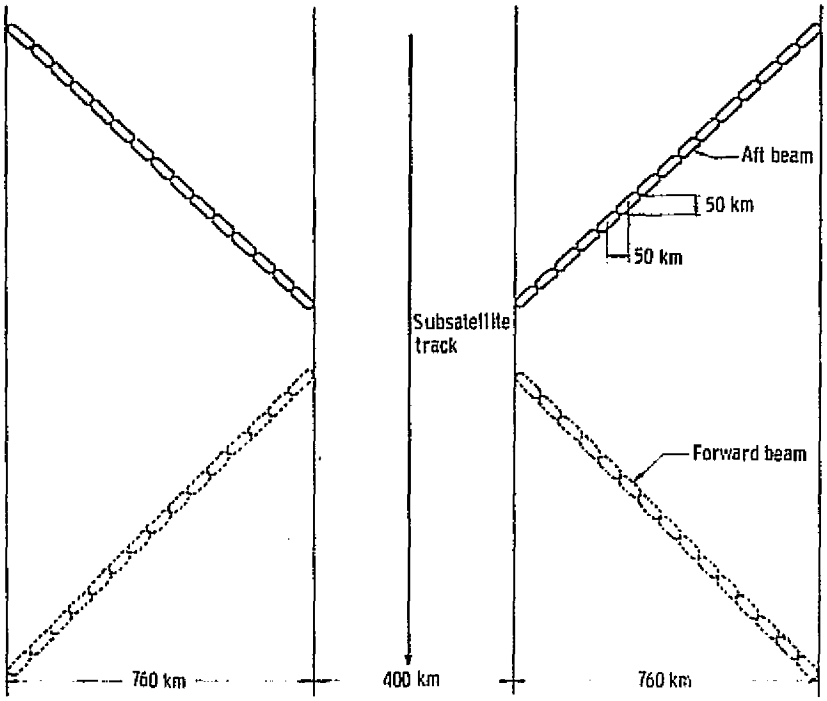

(a) Earth coverage geometry and scatterometer doppler cells

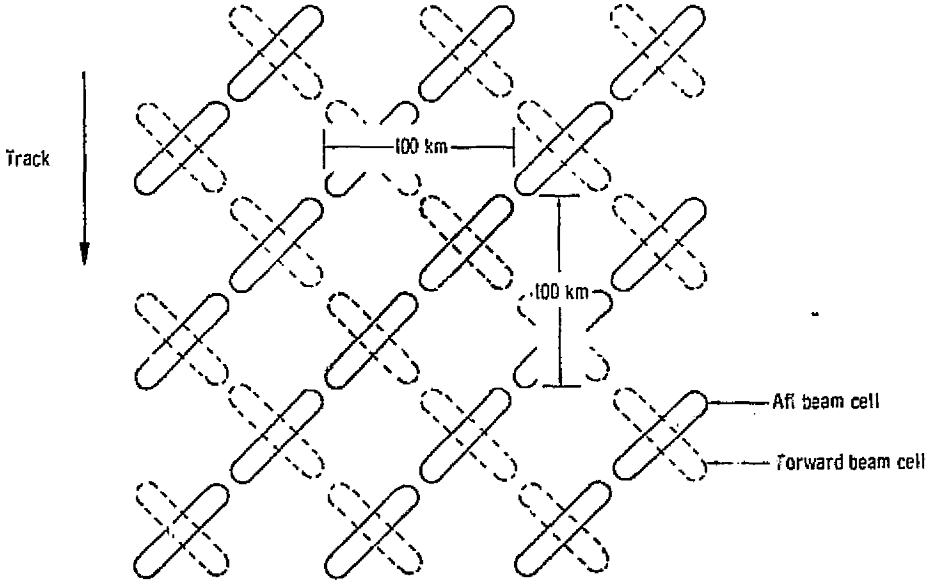

(b) Expanded view of forward and aft footprint crossings - 100 km grid

Figure 19.- Orthogonal doppler cell crossings for forward and aft antenna beams (Mode I).

- Operating Frequency Same as Mode I
- Scattering Cross Section Measurement Ability
  - σ^o normalized standard deviation - optimize by proper choice of antenna beamwidth β and θ_p (Tube power fixed by Mode I requirements). Beamwidth angle ϕ must be same as Mode I to minimize antenna development cost.
  - Range of σ^o values (See Note 1)

Parameter \ Frequency Angle	0	10	20	25	30	40	50	55	60	65
σ^o_{max} , dB	+20	+9	+5	+7	+6	+3	+2	0	0	0
σ^o_{min} , dB	+4	+2	-13	-19	-24	-27	-30	-31	-31	-31

  - Maximum σ^o bias error ± 2 dB
  - σ^o resolution requirement 0.2 dB
- Antenna Requirements
  - Azimuth angle 0° or 180° relative to satellite subtrack vector
  - Earth incidence angle 0 to 65°
  - Side lobe level -20 dB relative to peak gain
  - Polarization options σ_{VV} , σ_{HH} , σ_{HV} , σ_{VH}
  - Polarization purity 99 percent
  - Cross polarization level -20 dB
    (Integrated value over the half power beam relative to integrated value of main beam primary polarization)
- Resolution Cell Size 50 km (including integration smear)
- Geometric Separation Between σ^o Measurements
  - Mode II (Common resolution cell σ^o measurement for each incidence angle.)
  - Mode III, IX, and X 100 km along track.

Note 1. The range of values is based on RADSCAT aircraft data (upwind, downwind, and crosswind) and has a 3 dB margin at both ends of the σ^o range.

Note 2. Signal return due to integrated effects of side lobes must be 20 dB below return signal from main beam for that same doppler band.

FIGURE 20 SCATTEROMETER PERFORMANCE SPECIFICATION MODE II

Mode Identification	Antenna Polarization		Swath Width	Comments
	Antenna no. 1, 2, 3, 4	Antenna no. 5		
I	σ^{o}_{VV}, σ^{o}_{HH}	–	1000 Km	Mode for taking operational data
II		σ^{o}_{VV}, σ^{o}_{HH}, σ^{o}_{VH}, σ^{o}_{HV}	NA	Research mode for evaluating instrument limits
III	σ^{o}_{VV}	Any two pol.	1000 Km	Gives user req'd wind speed and direction plus wind speed along the satellite subtrack
IV	σ^{o}_{HH}	Any two pol.	1000 Km	Gives user req'd wind speed and direction plus wind speed along the satellite subtrack
V	σ^{o}_{VV} antennas 1 and 2 only	–	500 Km	Improves σ^{o} measurement accuracy for V_{pol} operational data
VI	σ^{o}_{VV} antennas 3 and 4 only	–	500 Km	Improves σ^{o} measurement accuracy for V_{pol} operational data
VII	σ^{o}_{HH} antennas 1 and 2 only	–	500 Km	Improves σ^{o} measurement accuracy for H_{pol} operational data
VIII	σ^{o}_{HH} antennas 3 and 4 only	–	500 Km	Improves σ^{o} measurement accuracy for H_{pol} operational data
IX	σ^{o}_{VV}	σ^{o}_{VV}	1000 Km	Efficient mode for taking operational data including wind speed along subtrack
X	σ^{o}_{HH}	σ^{o}_{HH}	1000 Km	Efficient mode for taking operational data including wind speed along subtrack

Note: It may not be possible to get all four polarization measurements made for all incidence angles at the instrumented test site during one satellite pass. 1st priority should be given to providing all incidence angles at each polarization, then to providing differential σ^{o} measurements at a given angle between polarizations.

Figure 21.- Representative Mode Options for Scatterometer.

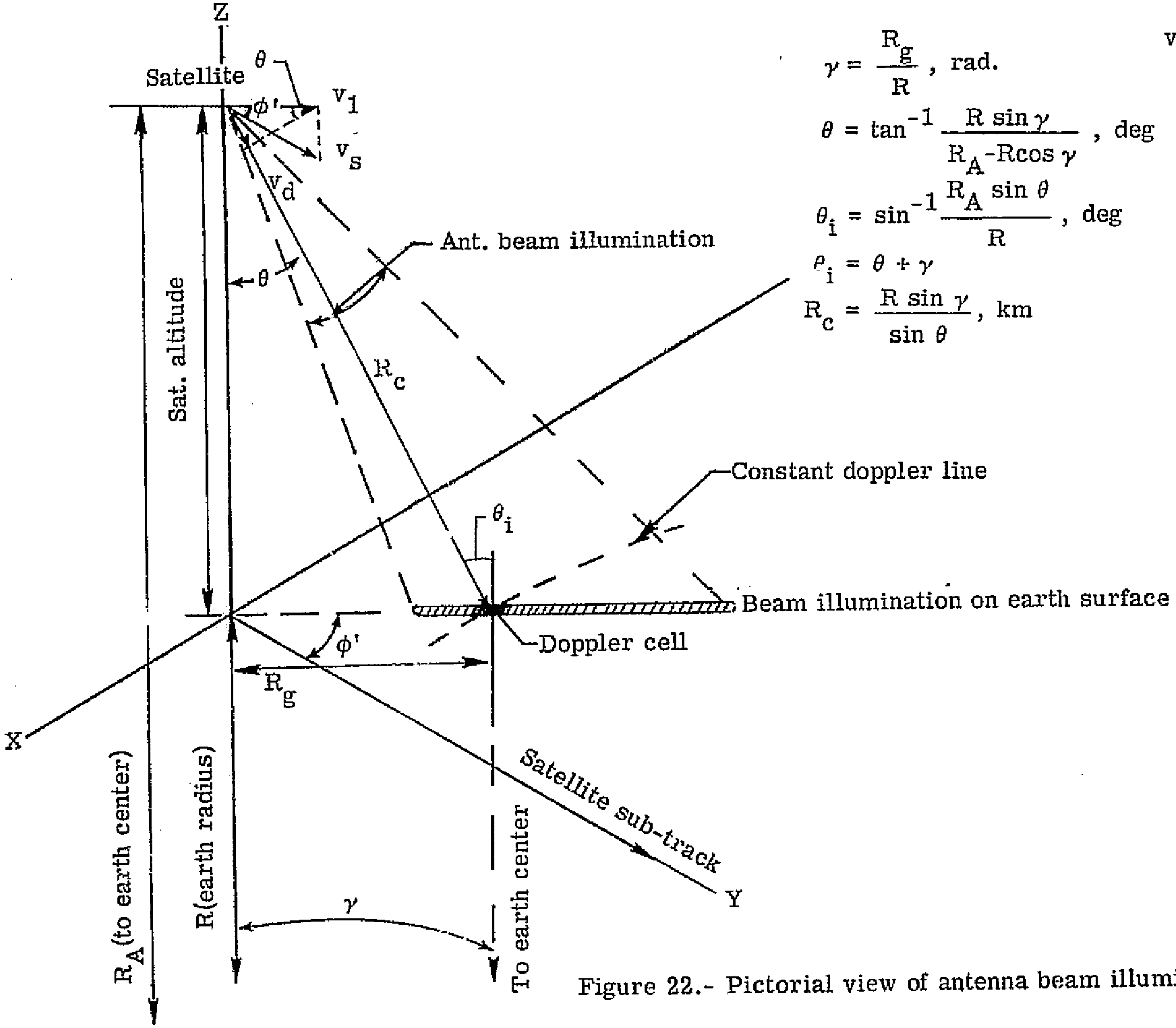

Applicable equations

$$\gamma = \frac{R_g}{R}\text{, rad.}$$

$$\theta = \tan^{-1}\frac{R\sin\gamma}{R_A - R\cos\gamma}\text{, deg}$$

$$\theta_i = \sin^{-1}\frac{R_A\sin\theta}{R}\text{, deg}$$

$$\theta_i = \theta + \gamma$$

$$R_c = \frac{R\sin\gamma}{\sin\theta}\text{, km}$$

$$v_1 = v_s\cos\phi' = v_s\cos 45^\circ$$

$$v_1 = \frac{\sqrt{2}}{2}v_s$$

$$v_d = v_1\sin\theta$$

$$v_d = \frac{\sqrt{2}}{2}v_s\sin\theta$$

$$f_D = \frac{2v_d f_t}{C}\text{, Hz}$$

$$f_D = \frac{\sqrt{2}v_s f_t}{C}\sin\theta\text{, Hz}$$

Figure 22.- Pictorial view of antenna beam illumination geometry.

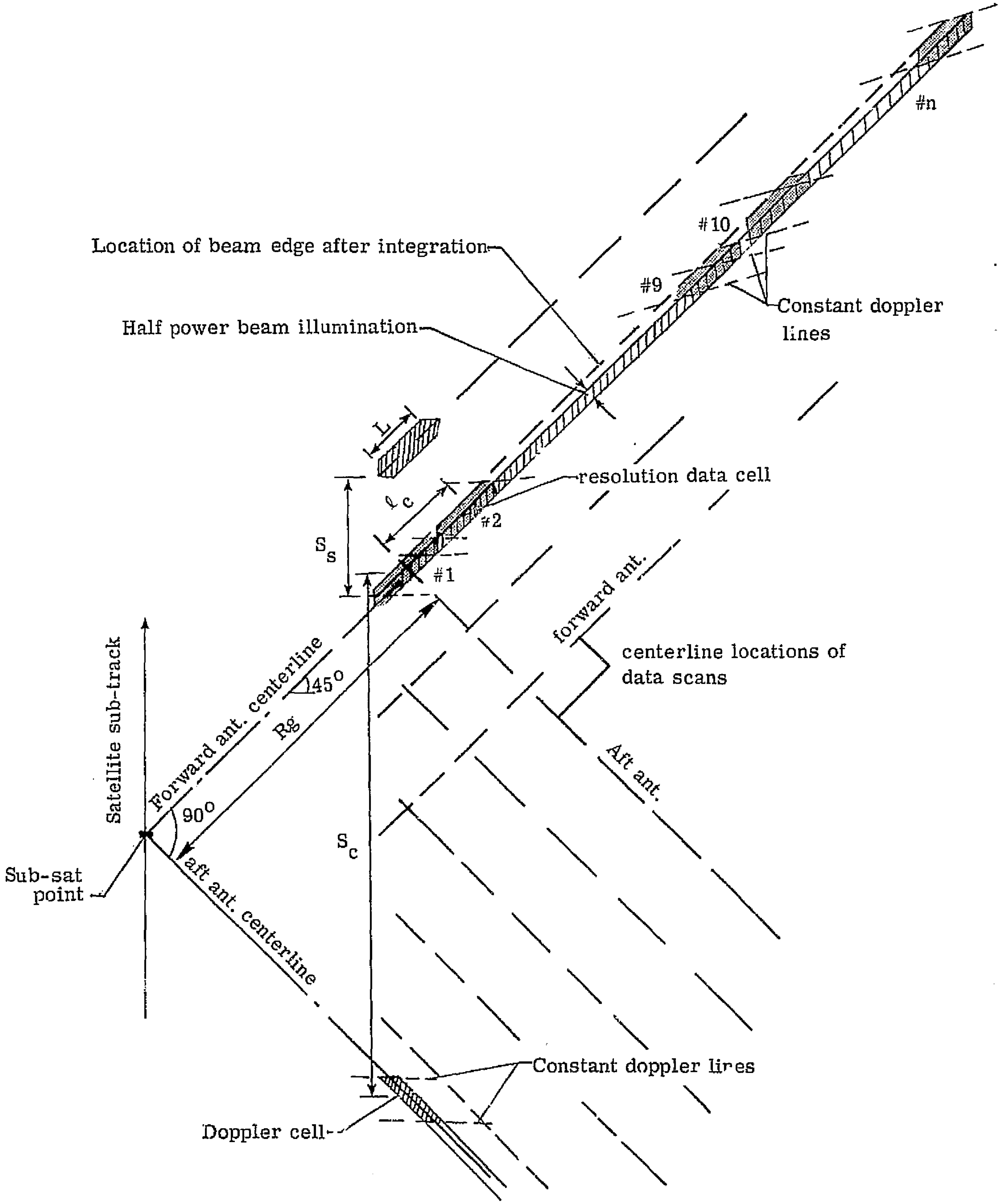

Figure 23.- Plan view of antenna illumination geometry (one side of satellite).

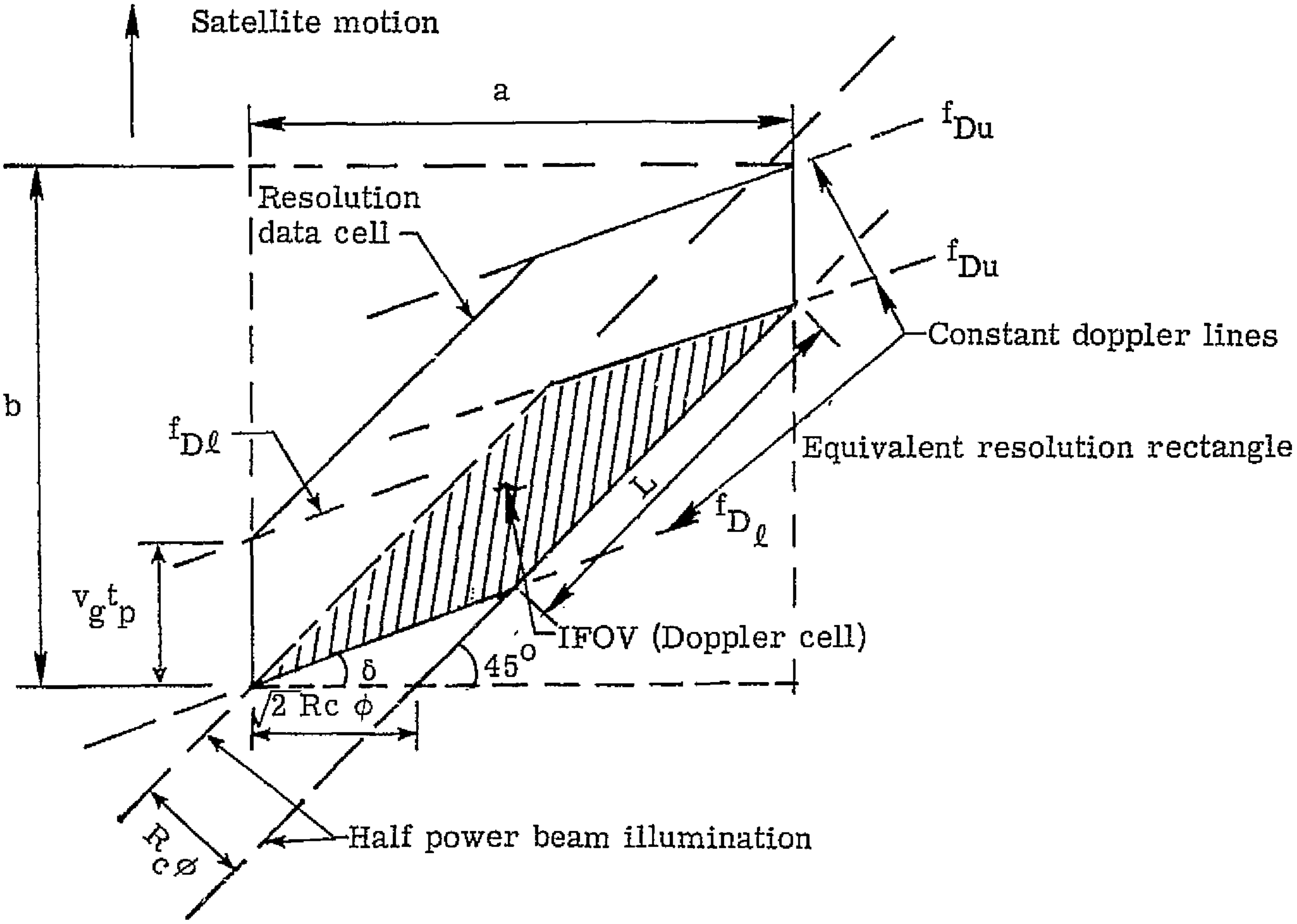

$$\text{IFOV} = A_c = R_c \phi L$$

$$\text{Doppler BW} = B_c = f_{D_u} - f_{D_\ell}$$

$$\text{Equivalent resolution} = r = \frac{a + b}{2}$$

$$L = \sqrt{2}\, r - \frac{V_g t_P}{\sqrt{2}} - R_c \phi - \frac{\sqrt{2}\, R_c \phi \sin \delta}{\sin (135 + \delta)}$$

Figure 24.- Geometry of one resolution cell.

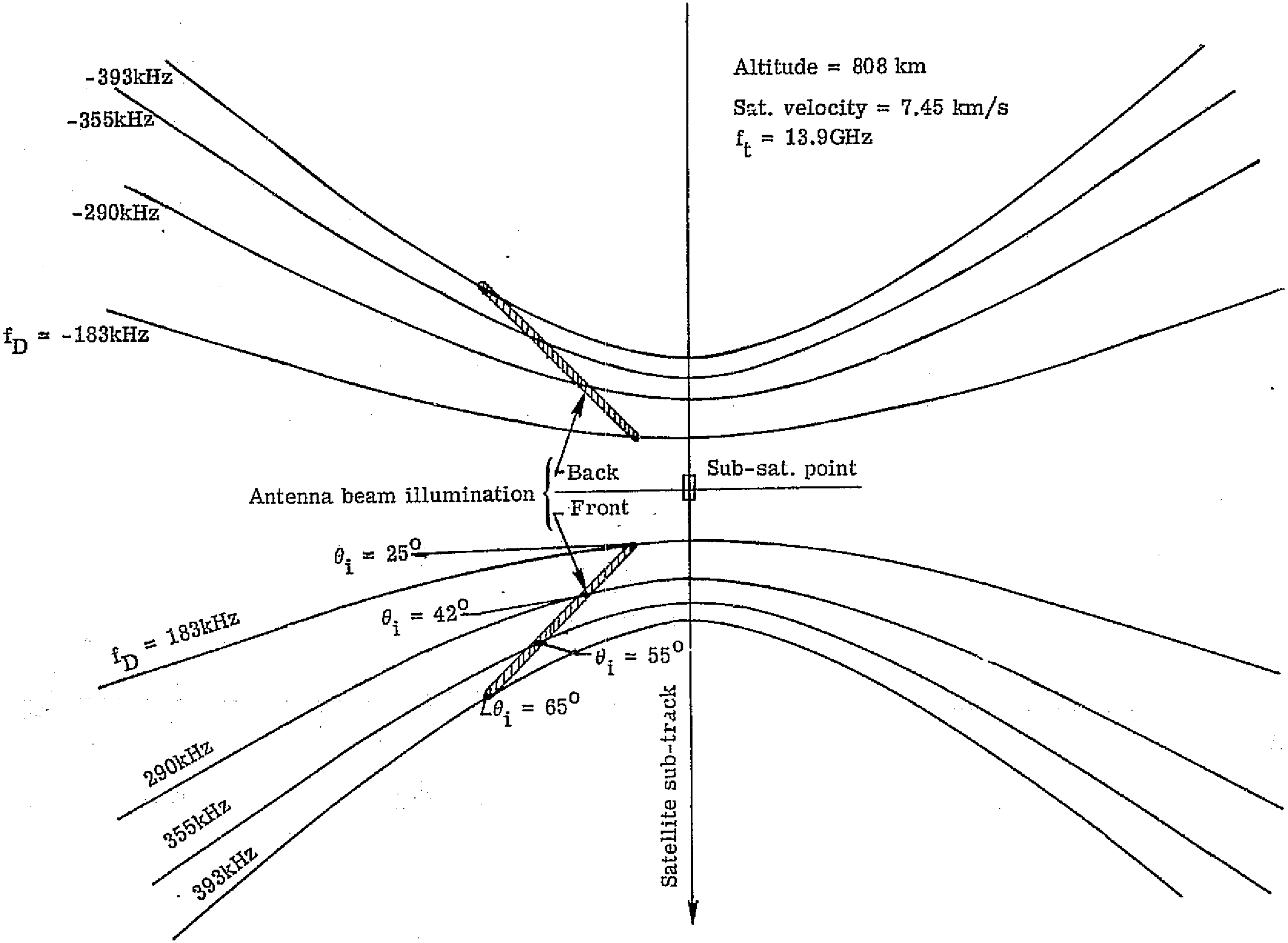

Figure 25.- Plot of constant doppler lines on earth surface.

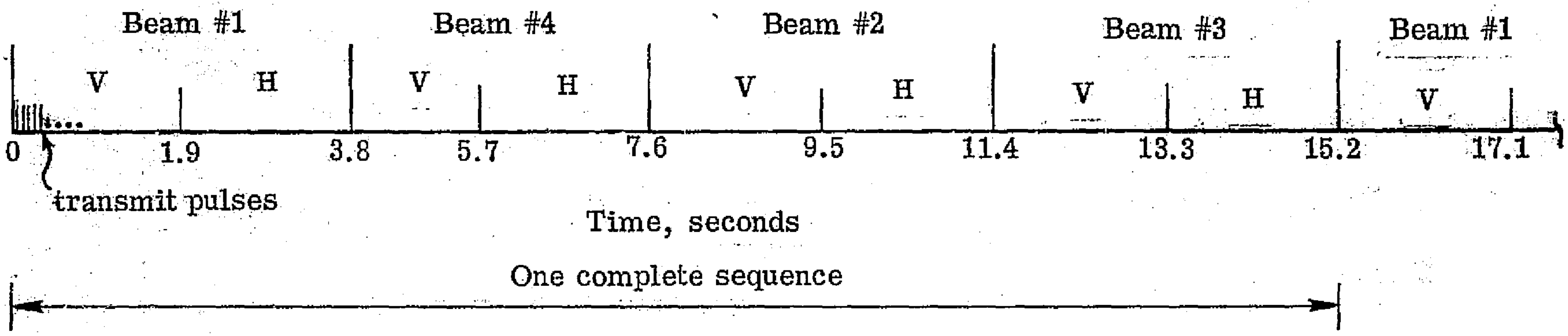

Note: V = Vertical polarization (transmit & receive)
H = Horizontal polarization (transmit & receive)

Figure 26.- Scatterometer mode 1 measurement sequence.

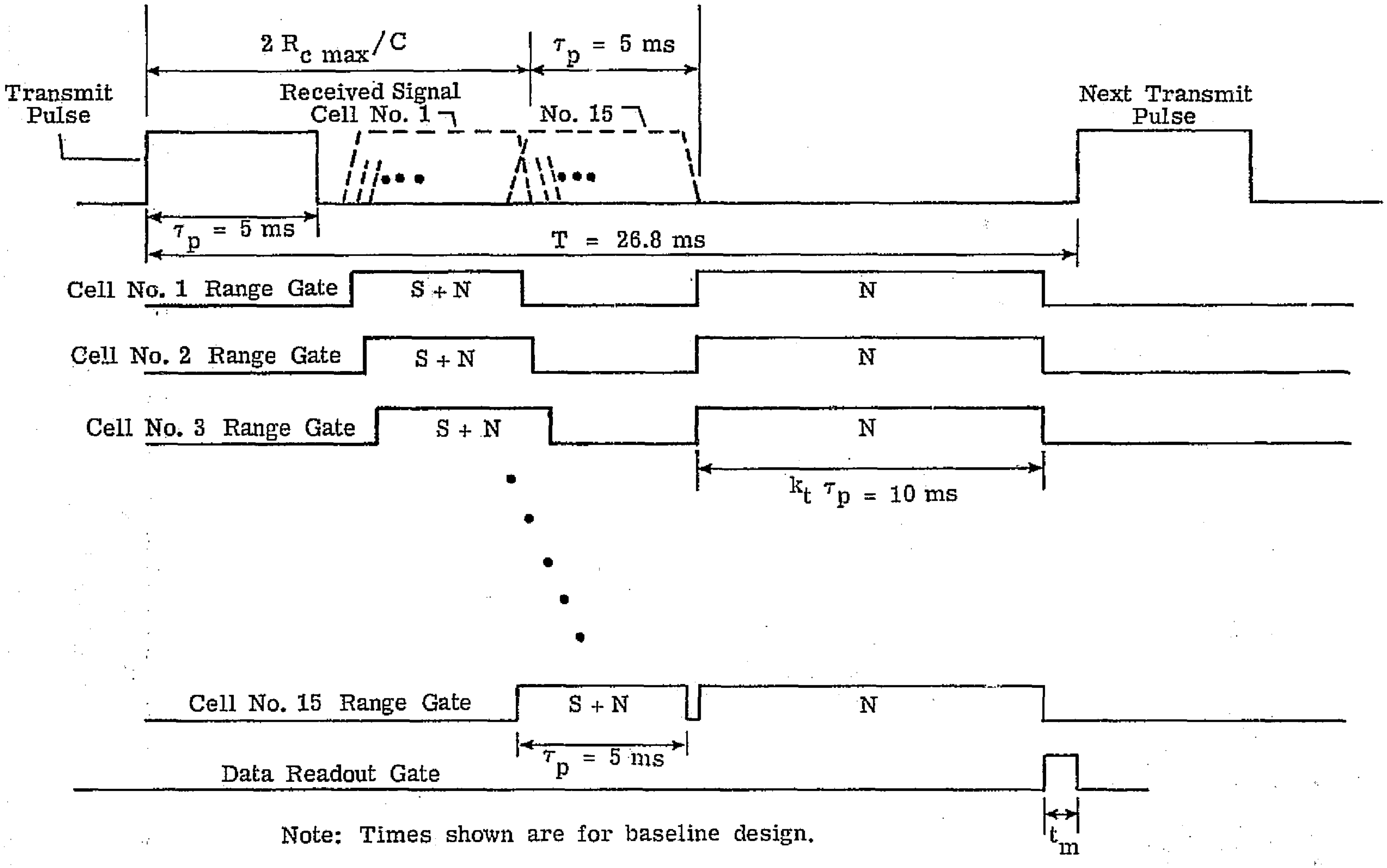

Note: Times shown are for baseline design.

$$T = \frac{2R_{c\,max}}{C} + \tau_p + k_t \tau_p + t_m, \text{ sec.} \quad , \quad k_t = \frac{\tau_N}{\tau_{SN}} = 2$$

$$\tau_{SN} = t_p \left(\frac{\tau_p}{T}\right), \text{ sec.}$$

Figure 27.- Transmit, receive, and processing timing diagram.

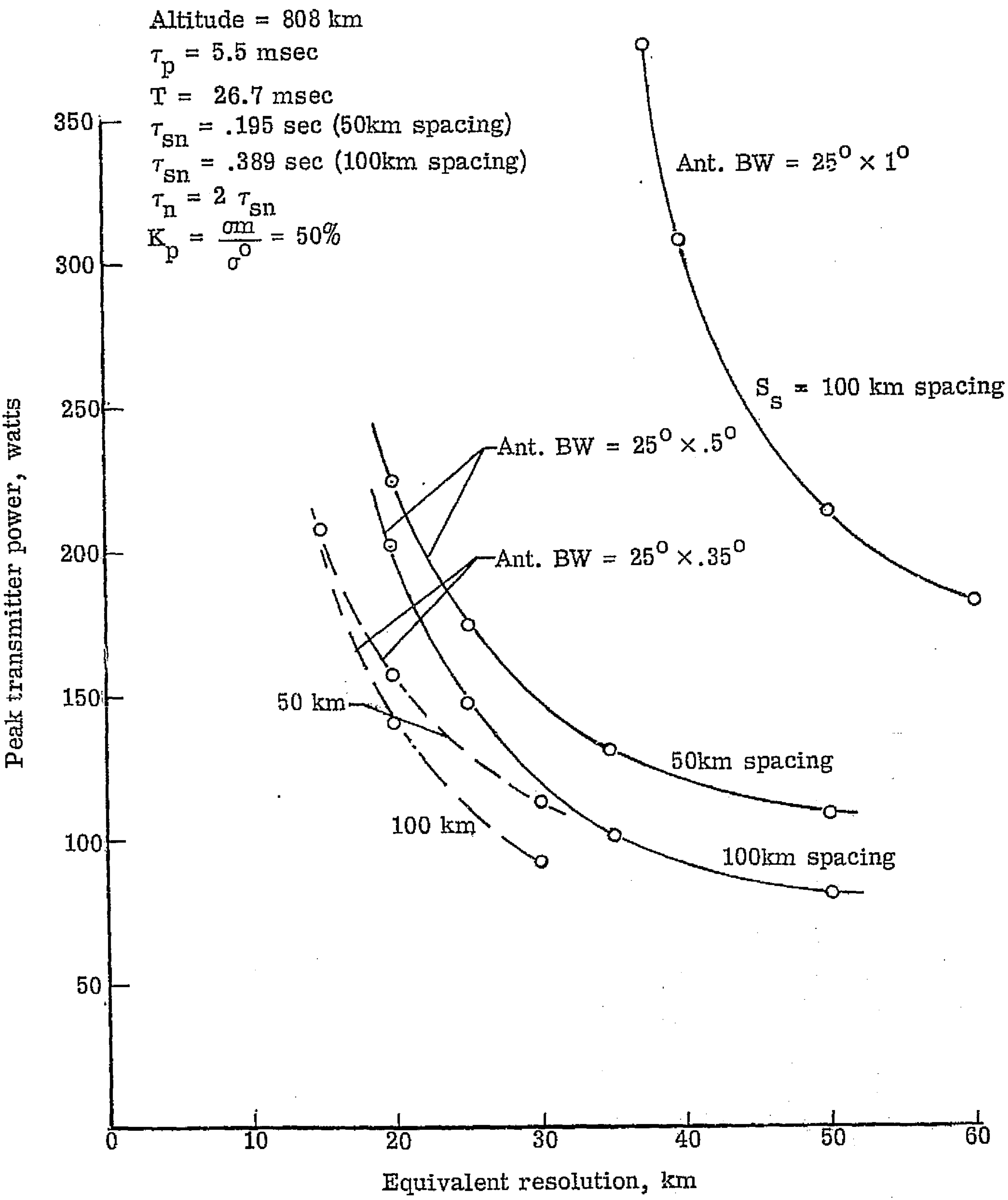

Figure 28.- Transmitter power requirements for fan beam scatterometer.

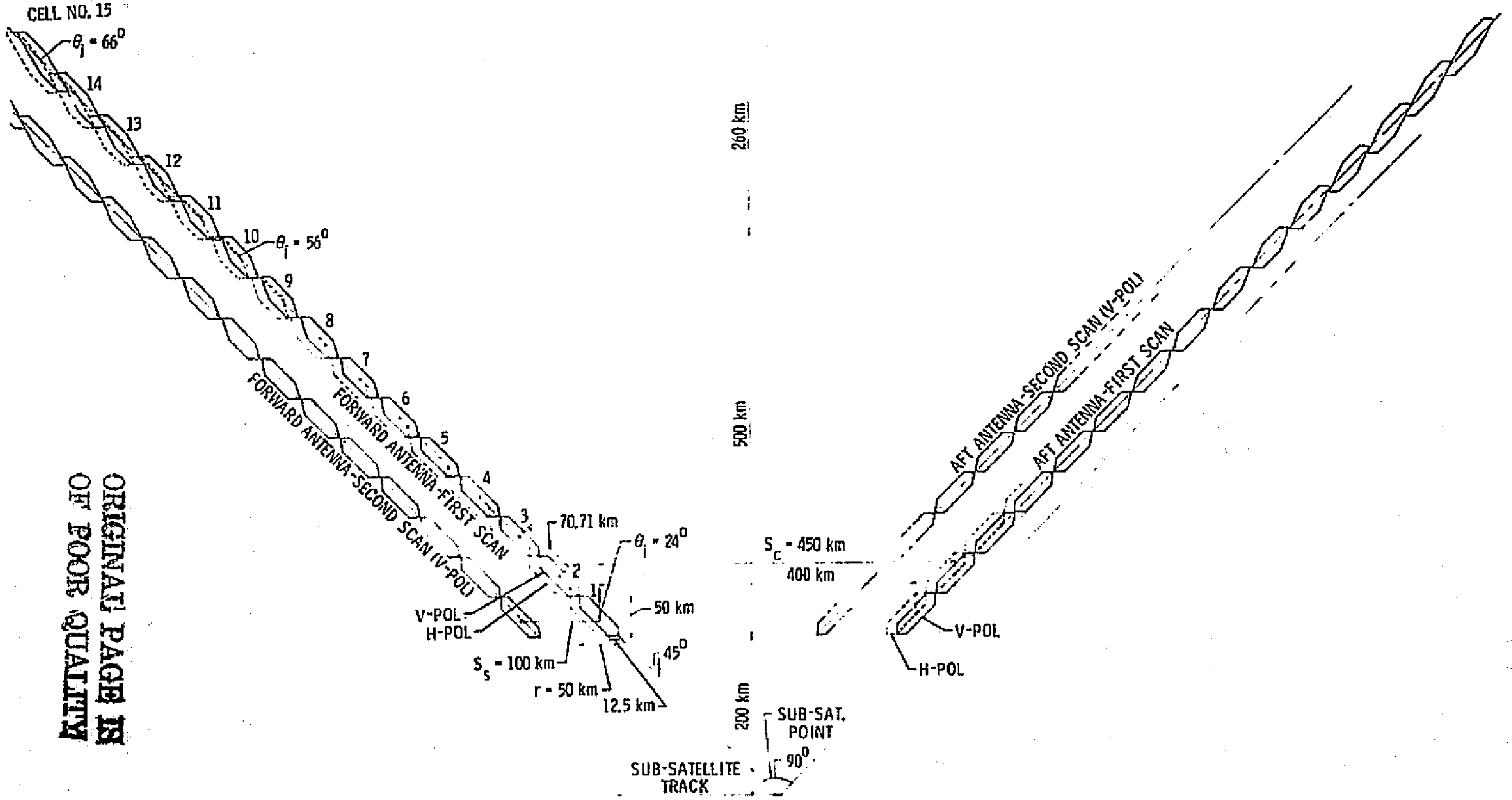

Figure 29.- Diagram of data cells illumination from forward and aft antenna - Mode I.

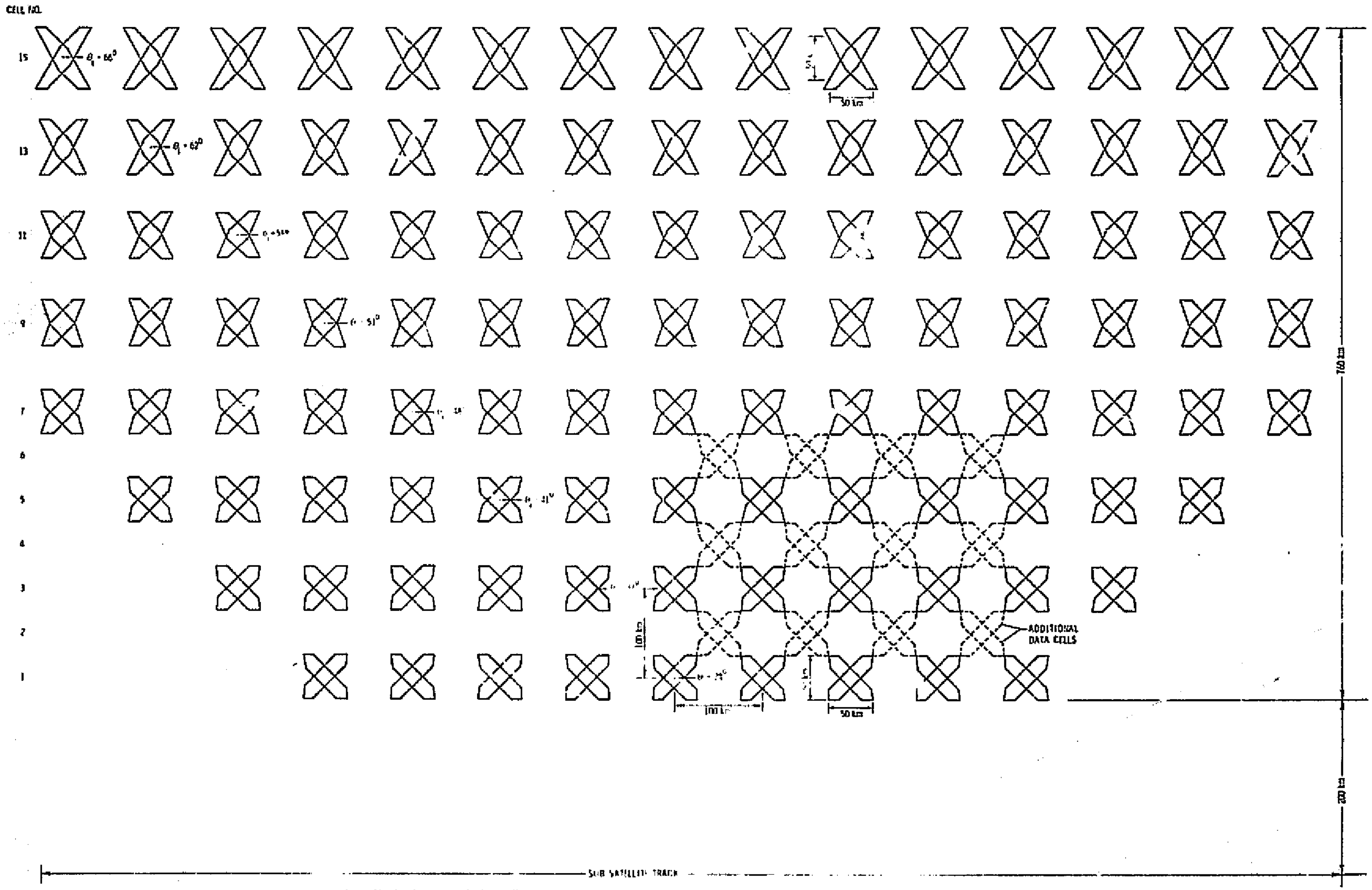

Figure 30.- Detailed diagram of data cell illumination from intersection of forward and aft antenna-cone polarization, Mode 1.

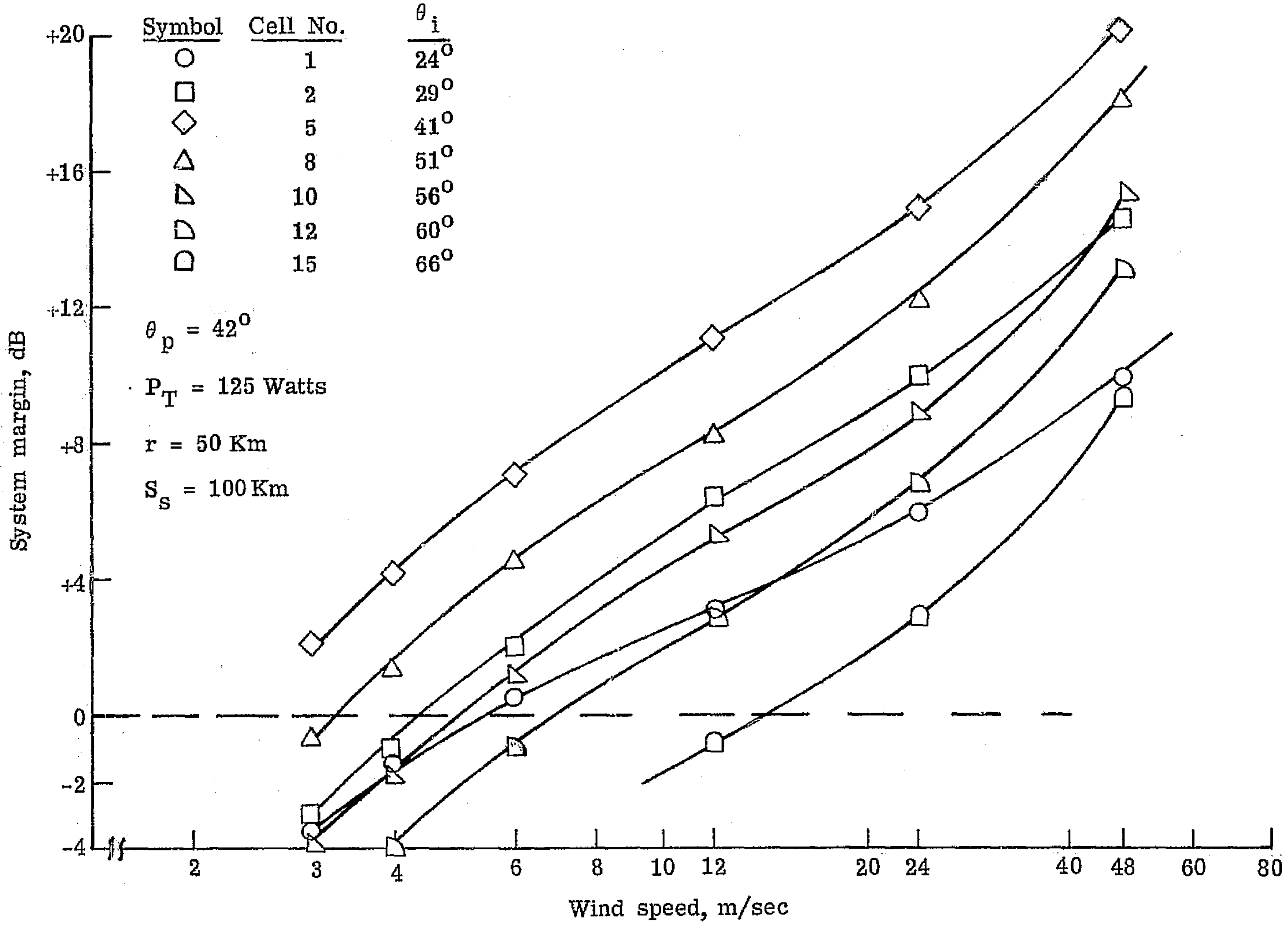

Figure 31.- Margin available for various wind speeds.

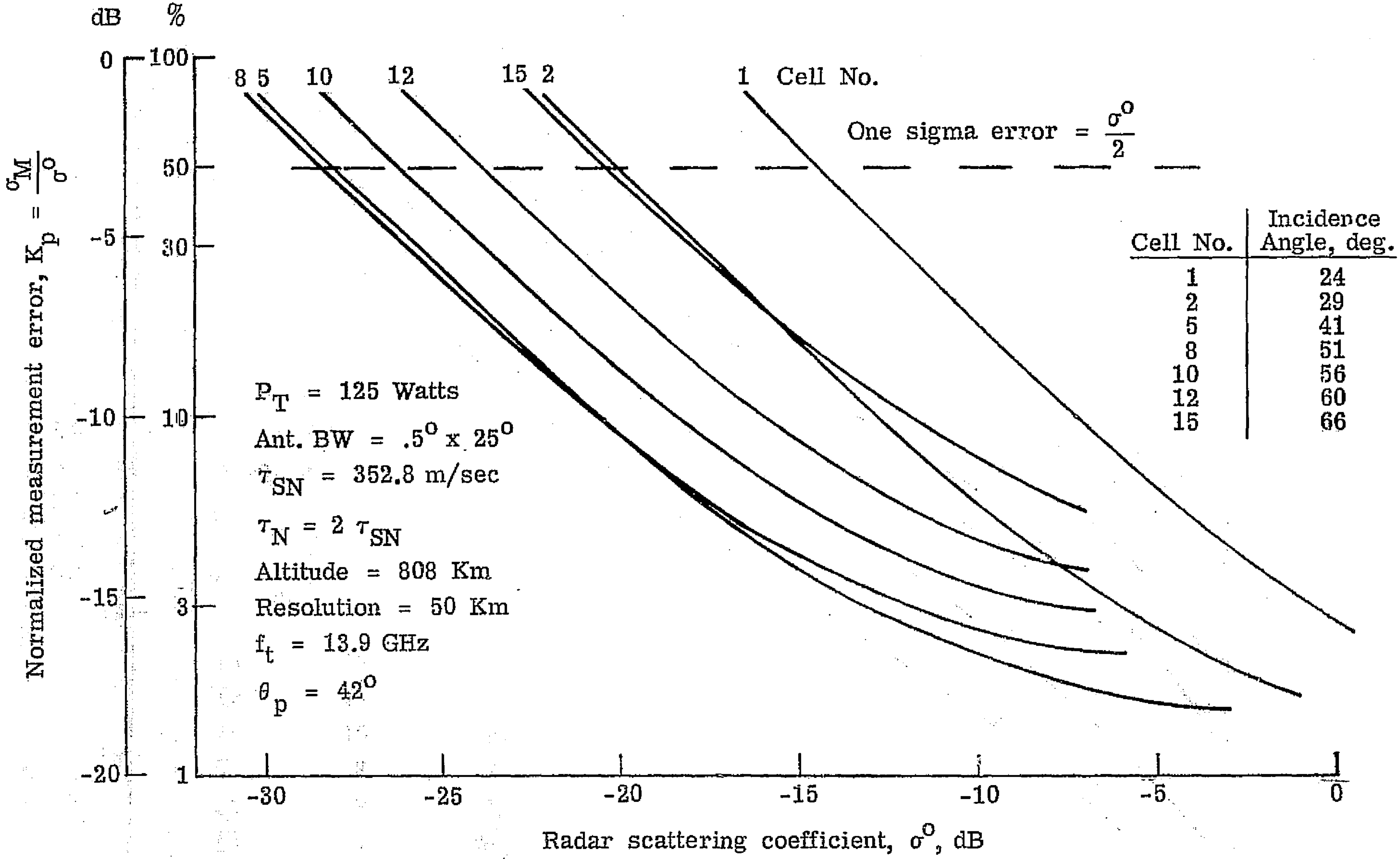

Cell No.	Incidence Angle, deg.
1	24
2	29
5	41
8	51
10	56
12	60
15	66

Figure 32.- Radar scattering coefficient measurement error.

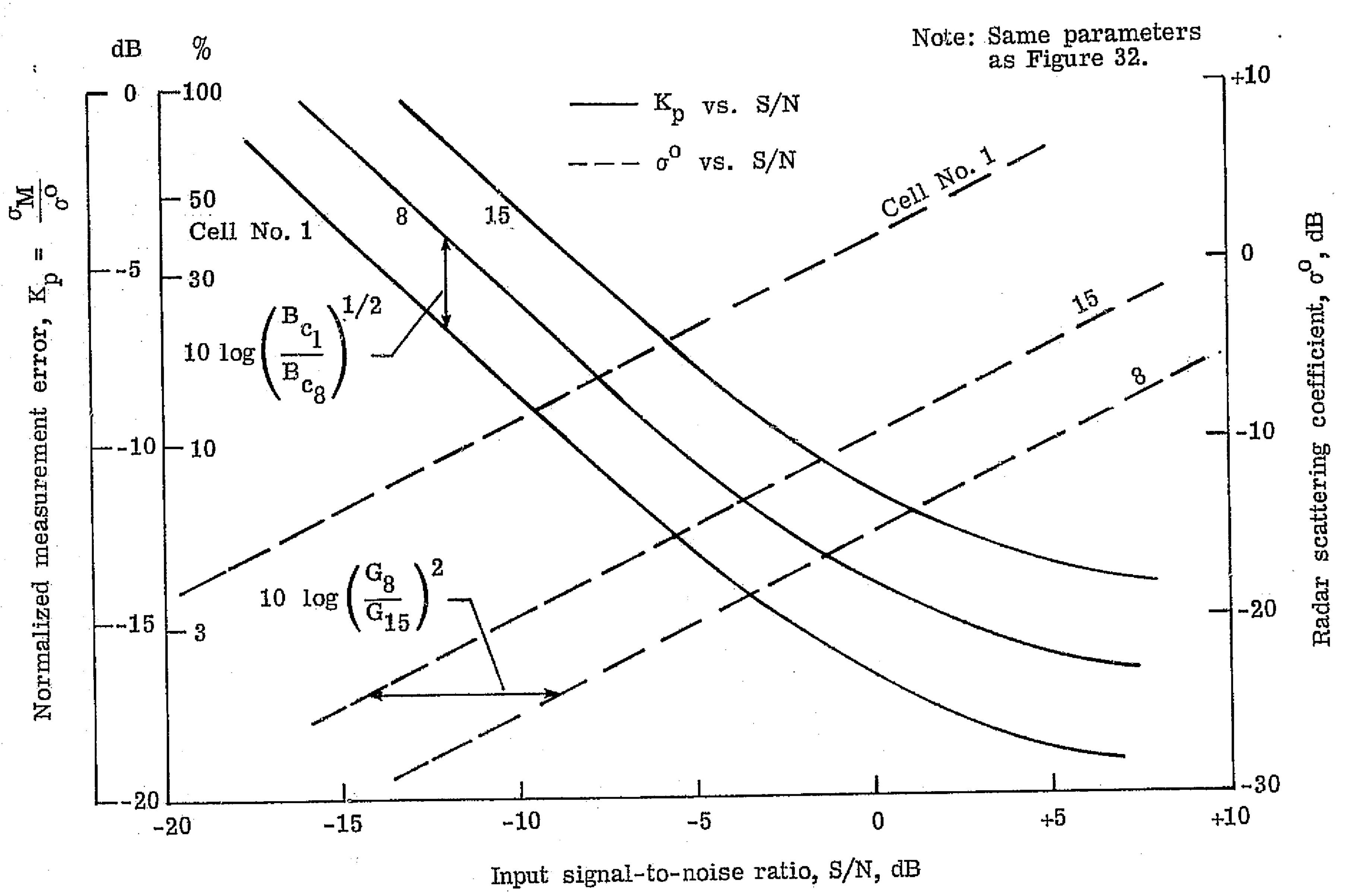

Figure 33.- Relationship of measurement error, K_p and scattering coefficient, σ^o to input signal-to-noise ratio, S/N.

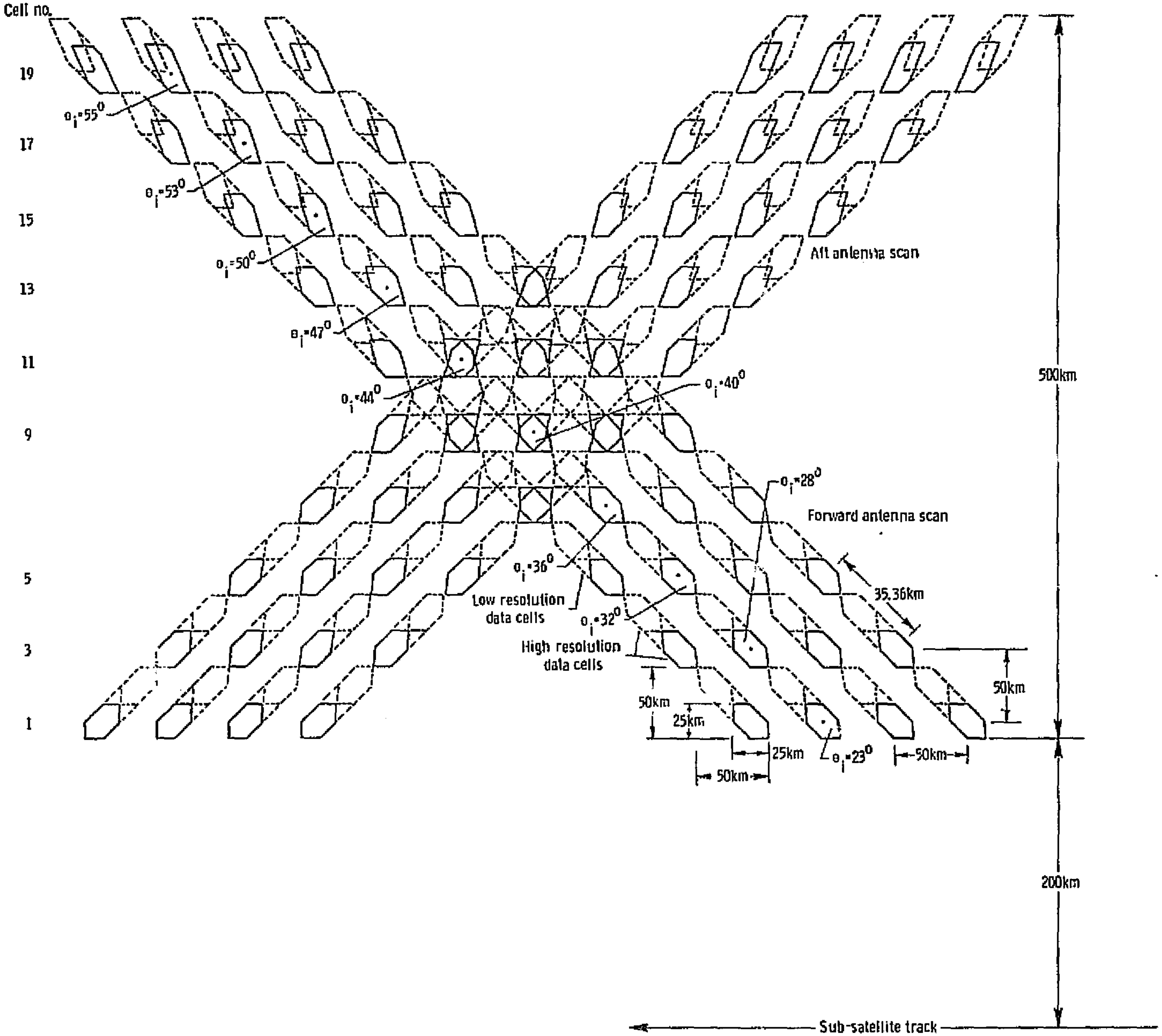

Figure 34.- Sample scan pattern of high resolution data cell illumination from forward and aft antenna-one polarization-mode 1.

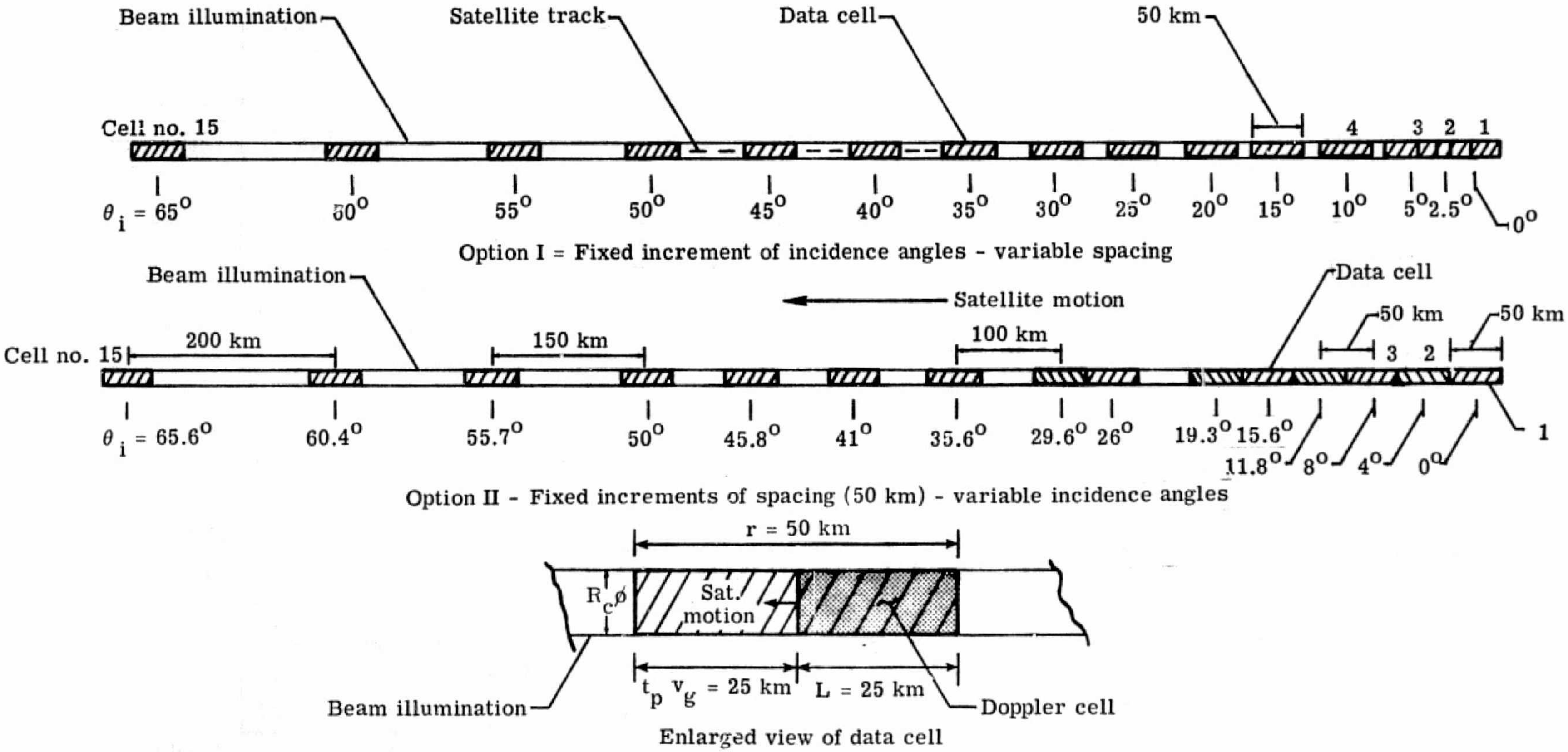

Figure 35.- Geometry of surface illumination for one polarization - Mode II.

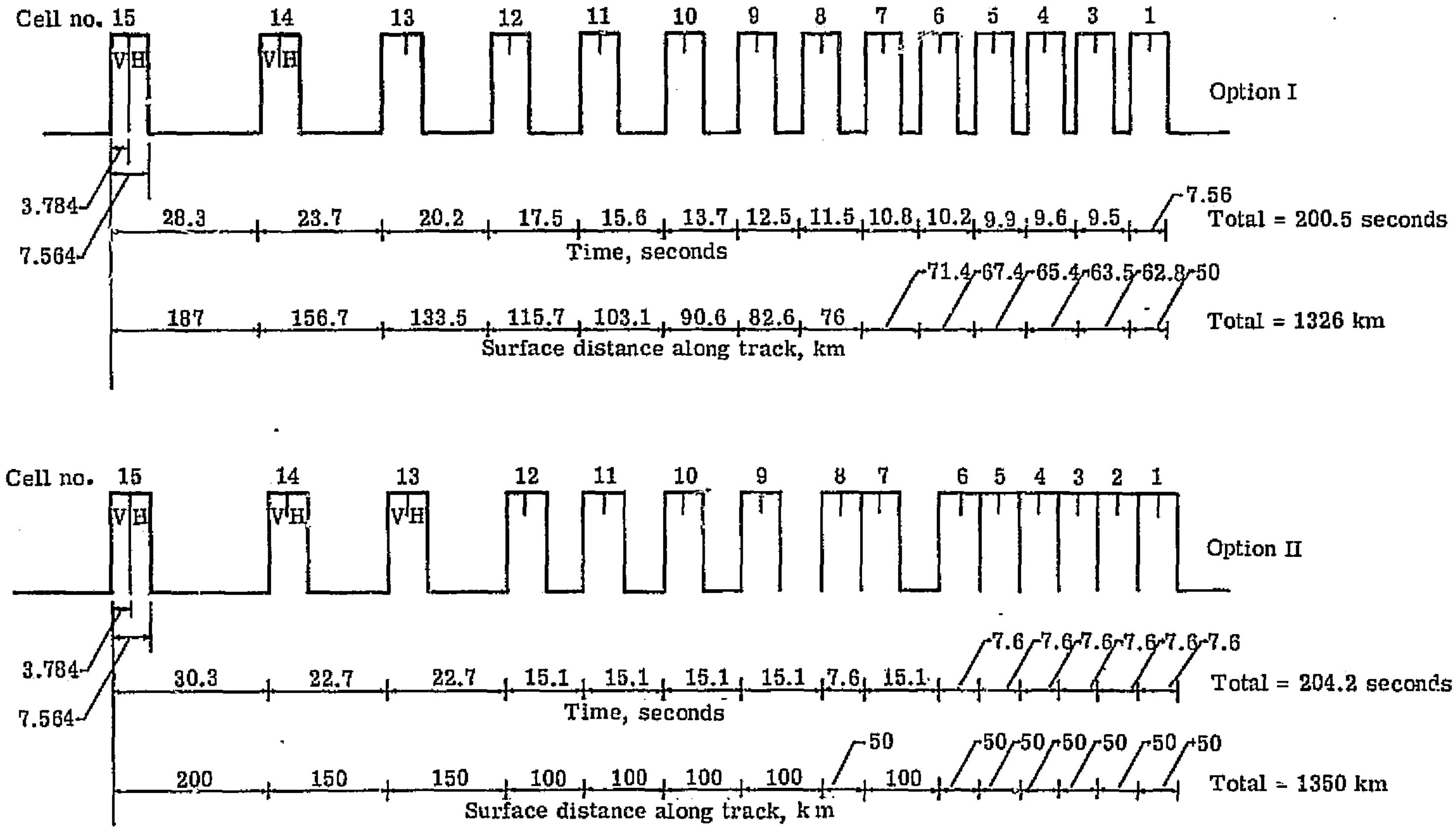

Note - V = Vertical polarization
H = Horizontal polarization

Figure 36.- Mode II measurement sequence - two options

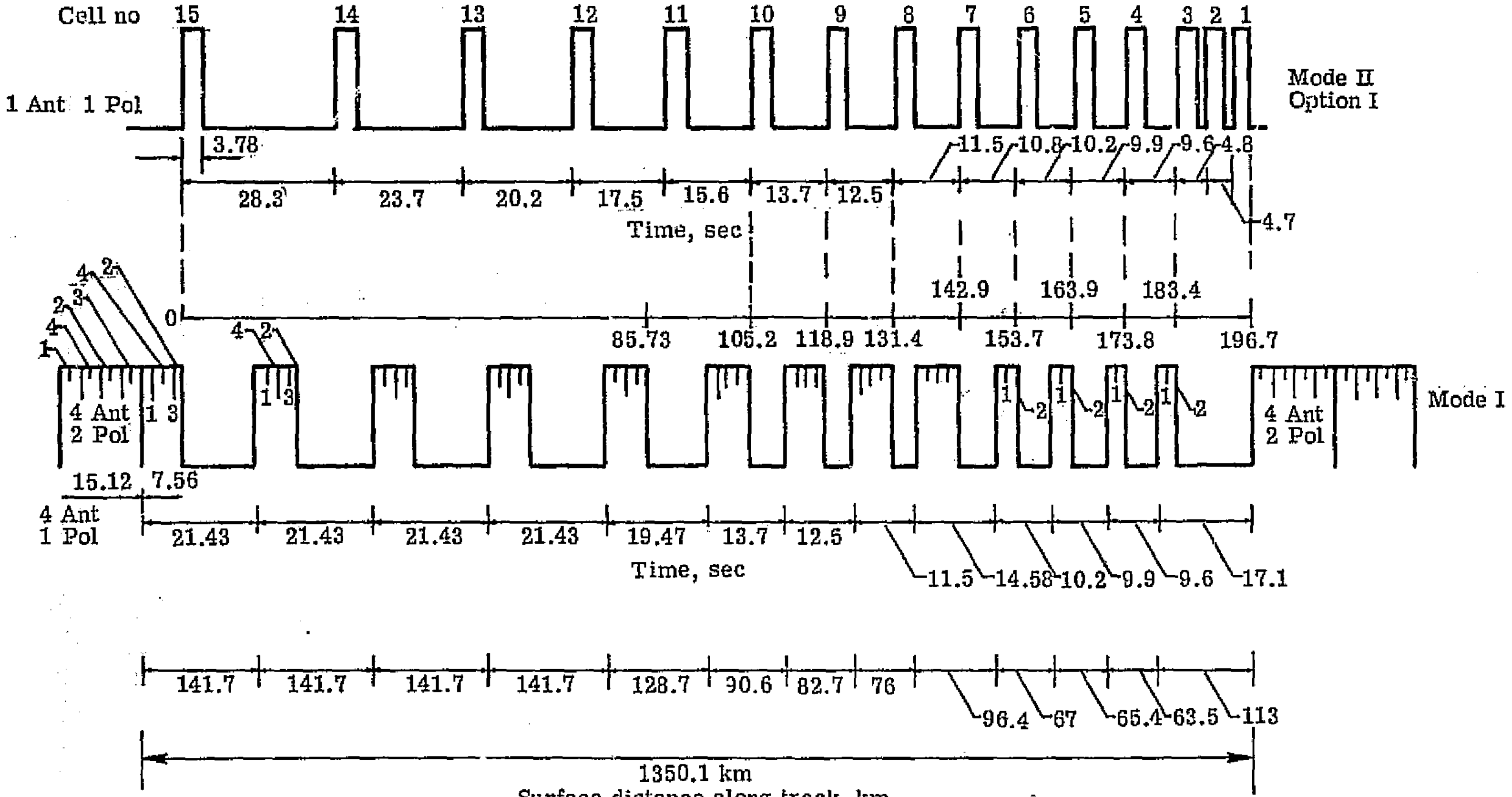

Figure 37.- Combined measurement sequence for Mode I and II using one polarization in Mode II.

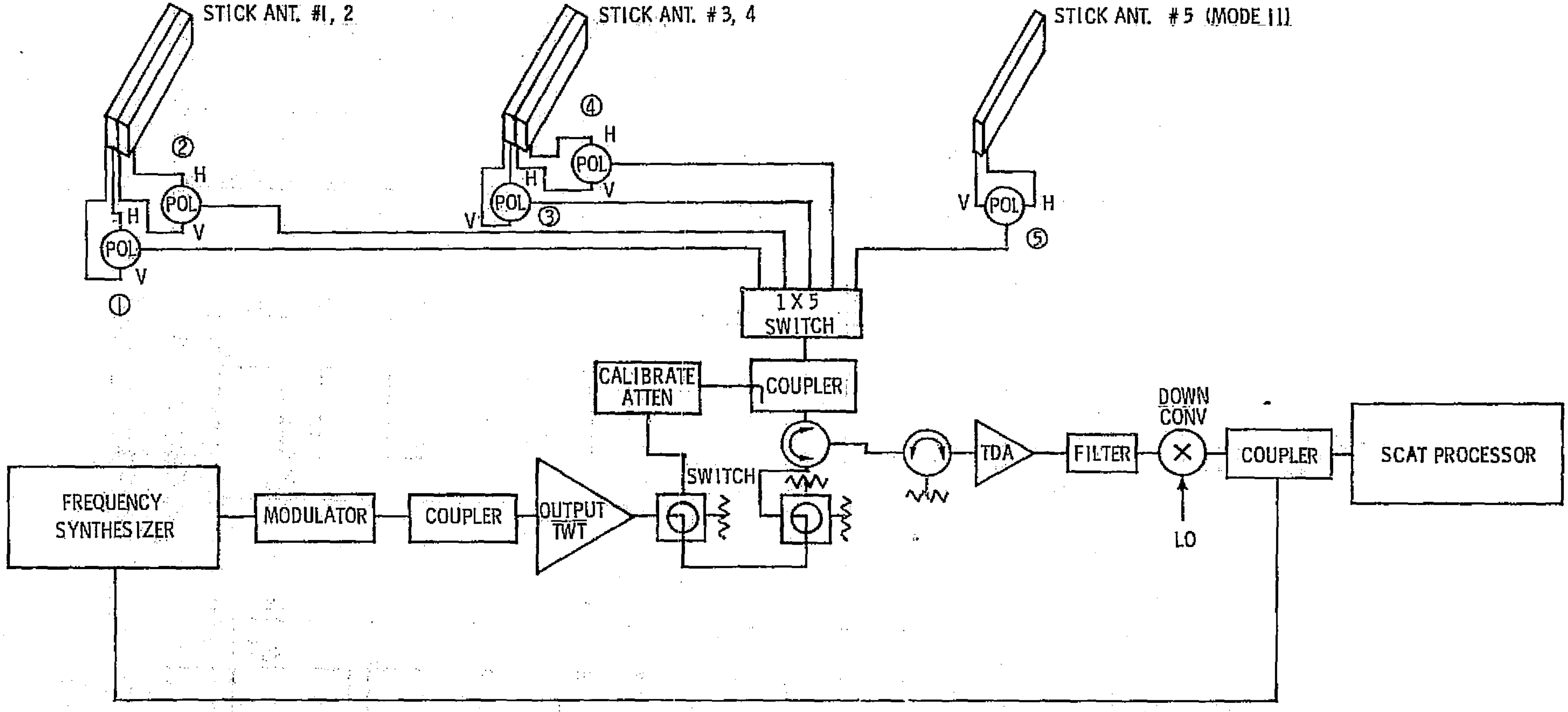

Figure 38.- Scatterometer block diagram.

APPENDIX 1

DERIVATION OF THE GEOMETRIC PARAMETER EQUATIONS

By E. M. Bracalente
Langley Research Center

This appendix includes a description and derivation of the various equations defining the geometric parameters involved in the scatterometer design. These parameters include angles and distances defining the location of a data cell, dimensions of a data cell, and the doppler frequencies and bandwidths which form a doppler cell.

Mode I

Figures A1-1 and A1-2 illustrate the side view and plan view geometry associated with the fan beam illumination (also see figures 22 and 23 in the main text). These figures should be referred to for the derivation of the design equations. From figure A1-1, using the law of sines, we have that

$$\sin \theta_i = \frac{R_A}{R} \sin \theta \qquad (1)$$

and

$$R_c = \frac{R \sin \gamma}{\sin \theta} \qquad (2)$$

Using equation (1) and the relationship

$$\theta_i = \theta + \gamma \qquad (3)$$

the following equation is obtained,

$$\tan \theta = \frac{R \sin \gamma}{R_A - R \cos \gamma} \qquad (4).$$

The ground range, R_g, from the sub-satellite point is determined by the relationship

PRECEDING PAGE BLANK NOT FILMED

$$R_g = \frac{\pi}{180} \gamma R \qquad (5).$$

Using these equations the location of each doppler cell with respect to the satellite can be obtained.

The data cell locations along each fan beam is established by the proper choice of filter frequencies and bandwidths. To determine these filters certain requirements must be established. These requirements include resolution (r), along-track and cross-track spacing between data cells (S_s), swath width, and the approximate range of incidence angles. An additional requirement is also imposed that two orthogonal data cell measurements must be made at the same surface of the earth. This is done using measurements from a forward and aft antenna which have azimuth angles that are 90^o apart (see figure A1-2).

The doppler filter frequencies, as shown a little later, are a function of the angle θ, which in turn is a function of the earth angle γ and ground range, R_g (see equations (4) and (5)). Since two orthogonal measurements are required in each data cell, a value of γ or R_g must be chosen so that the aft antenna measurement overlaps the forward antenna measurement after the spacecraft moves the required ground distance (S_c), (see figure A1-1). In this case, the value of ℓ_c (data cell spacing along the antenna beam) is chosen so that the cross-track spacing equals the along track spacing. In the following paragraph, the equations for the value of parameters S_c, ℓ_c, and γ that will satisfy these requirements are derived. The effects of earth rotation on the orthogonal measurement requirement and the doppler velocity are neglected here, but will be discussed in a separate section.

The along-track and cross-track spacing S_s form legs of an equilateral right triangle with the dimension $2\ell_c$ as the hypotenuse (for $S_s = 2r$). The ground spacing R_g to the same instantaneous doppler cell on the forward and aft antenna beam illumination form legs of an equilateral right triangle with the spacing S_c as the hypotenuse (see figure A1-2). To a first approximation assuming the earth is a plane surface,

$$\ell_c = \frac{\sqrt{2}\, S_s}{2} \qquad (6),$$

and

$$S_c = \sqrt{2}\, R_g = \sqrt{2}\, \frac{R\pi}{180}\, \gamma \qquad (7).$$

However, since these dimensions form a right spherical triangle on the surface of the earth, the following relationships from spherical trigonometry apply;

$$\cos(\overline{2\ell_c}) = \cos^2 \bar{S}_s \qquad (8)$$

and

$$\cos \bar{S}_c = \cos^2 \bar{R}_g \qquad (9),$$

where $(\overline{2\ell_c})$, $\bar{S}_s$, $\bar{S}_c$, and $\bar{R}_g$ are the earth center angles subtended by these respective dimensions. Note that $\bar{R}_g$ is the same as the earth center angle, γ, to the doppler cell. Re-arranging equations (8) and (9) and substituting γ in for $\bar{R}_g$, the equations defining ℓ_c and S_c are obtained:

$$\ell_c = \frac{\pi R}{360} \cos^{-1} \left[\cos \frac{180\, S_s}{\pi\, R}\right]^2 \qquad (10);$$

$$S_c = \frac{\pi R}{180} \cos^{-1} (\cos^2 \gamma) \qquad (11).$$

The value of S_c to the first data cell for an incidence angle of approximately 25° must be chosen so that proper overlap of the aft and forward data cell can occur. To do this S_c must satisfy the equation

$$S_c = n_1 S_s + S_s/2 \qquad (12),$$

where n_1 is an integer. The $S_s/2$ factor in equation (12) correspond to the distance traveled by the beam illumination during the scanning of the front antenna on each side of the S/C. The value of S_c required for an incidence angle of 25° is approximately 467 km (808 km altitude). A value of $n_1 = 4$ will give an S_c value of 450 km for $S_s = 100$ km, and a value of $n_1 = 9$ will give an S_c value of 475 km for $S_s = 50$ km. In both cases the incidence angle, θ_i, falls approximately at the required 25°. The value of S_c in equation (12) can be found (for a data cell at higher incidence angles) by increasing n_1 by the factor (n-1), where n = the data cell number. Once the correct value of S_c is found for cell number one, then proper overlap will occur (neglecting earth rotation effects) for all data cells when the spacing between doppler cells is placed at a distance ℓ_c. Note that only every other data cell is required to give equal along track and cross-track spacing if the spacing S_s is twice the required resolution. Substituting equation (12) into equation (11) and solving for γ, the equation for determining the value of γ_1 (earth center angle to cell number 1) is obtained as follows;

$$\gamma_1 = \cos^{-1}\left[\cos \frac{90}{\pi R} S_s(2n_1 + 1)\right]^{1/2} \qquad (13).$$

For $n_1 = 4$ this equation reduces to

$$\gamma_1 = \cos^{-1}\left[\cos \frac{810\ S_s}{\pi\ R}\right]^{1/2} \qquad (14),$$

and for $n_1 = 9$ to

$$\gamma_1 = \cos^{-1}\left[\cos \frac{1710\ S_s}{\pi\ R}\right]^{1/2} \qquad (15).$$

Equation (14) is used (for 808 km altitude) for S_s equal to approximately 100 km (equation 3 in the main text), and (15) for S_s equal to approximately 50 km.

The next step in the design of the scatterometer system is the determination of the doppler filter frequencies and bandwidths. Before this can be done the parameter L, which forms two sides of the Instantaneous Field of View (IFOV) or doppler cell, must be determined. Figure A1-3 shows an enlarged view of a resolution data cell. As seen in this figure the IFOV is formed by the dimension L and the constant doppler lines (isodops) cutting across the beamwidth illumination determined by $R_c\phi$, where R_c is the slant range from the satellite to the center of the IFOV and ϕ is the antenna 3 db beamwidth. The parameter L is determined by the doppler frequency spread or bandwidth between the two constant doppler lines, f_{D_u} and f_{D_ℓ}. The subscripts l and u stand for the lower and upper end of the IFOV. As pointed out in the text the idosops are hyperboloids on the surface of the earth (see figure 25 in the text). A line tangent to any point on this hyperbolic isodop will form an angle δ with a line perpendicular with the line of S/C flight (see figure A1-3). The angle δ increases as you proceed out along the beam illumination. Across the dimension $R_c\phi$ the isodop is assumed to be a straight line. The distance traveled by the IFOV during the measurement period is equal to $v_g t_p$. The parameter t_p is related to the scan spacing S_s, the satellite ground speed v_g, and the number of antennas, (No_A), and number of polarizations, (No_P), used in the measurements during one scan cycle. For the four antenna, two polarization case then,

$$t_p = \frac{S_s}{No_A \times No_P \times V_g} = \frac{S_s}{8\ v_g} \qquad (16).$$

The resolution data cell on the surface of the earth is determined by the area generated by the doppler cell resulting from satellite motion during the measurement period. The equivalent resolution cell is defined as the square whose dimension is the average of the dimensions of a rectangle within which the area generated by the moving doppler cell (IFOV) fits diagonally, as illustrated in figure A1-3.

From figure A1-3 the equation defining the parameter L can be derived as follows. The equivalent resolution, r, is defined as

$$r = \frac{a + b}{2} \qquad (17),$$

where

$$a = c + \sqrt{2}\, R_c \phi \tag{18}$$

and

$$b = c + v_g t_p \tag{19}$$.

Substituting equations (18) and (19) into (17) and solving for c we have,

$$c = \frac{2r - v_g t_p - \sqrt{2}\, R_c \phi}{2} \tag{20}$$.

From figure A1-3 we see that parameter $L = \sqrt{2}d$. Also from the figure we see that

$$d = c - e \tag{21}$$

where $e = f \sin \delta$ (22),

and (from the law of sines) $f = \dfrac{\sqrt{2}\, R_c \phi \sin 135^\circ}{\sin(135^\circ + \delta)} = \dfrac{R_c \phi}{\sin(135^\circ + \delta)}$ (23).

Combining equations (20), (21), (22), and (23), we obtain

$$d = \frac{2r - v_g t_p - \sqrt{2}\, R_c \phi}{2} - \frac{R_c \phi \sin \delta}{\sin(135^\circ + \delta)} \tag{24}$$,

from which we can write the equation defining L as

$$L = \sqrt{2}\, r - \frac{v_g t_p}{\sqrt{2}} - R_c \phi - \frac{\sqrt{2}\, R_c \phi \sin \delta}{\sin(135^\circ + \delta)} \tag{25}$$.

All parameters in equation (25) are known or can be determined from previous equations except for the angle δ. The range R_c used in this equation is the value calculated for the center of the IFOV (R_c varies slightly across the doppler cell from the f_{D_ℓ} to f_{D_u} isodops). Also, since the angle δ varies slightly across the doppler cell, the value of δ at the center of the cell is used. Before the equation defining δ is derived, the equation defining the doppler frequencies and bandwidths must be derived.

Figure A1-4 is a pictorial view of the antenna beam illumination along with appropriate velocity vectors. The earth velocity vector orientations are shown for the equator crossing for both the ascending and descending direction. The earth velocity vector will be neglected for this first derivative of the doppler frequency equation. A later section will cover the effects of earth rotation on the doppler frequency. By inspection we see that

$$v_1 = v_s \cos \phi' \qquad (26),$$

and

$$v_d = v_1 \sin \theta \qquad (27),$$

where v_s = the satellite velocity
v_1 = the component of satellite velocity in the plane of the fan beam
and v_d = the component of doppler velocity or range rate along the range line R_c .

The two-way doppler frequency f_D is found from the well known equation

$$f_D = \pm \frac{2 v_d f_t}{c} \qquad (28),$$

whe e f_t = the transmitting frequency,
and c = the speed of light.

Positive doppler frequencies occur on the two antennas pointed forward of the satellite and negative doppler frequencies on the antennas pointed aft. Combining equations (26), (27), and (28) the following equation results:

$$f_D = \pm \frac{2f_t}{c} v_s \cos \phi' \sin \theta \qquad (29).$$

Since the antennas are placed at 45° to the satellite velocity vector, equation (29) reduces to

$$f_D = \pm \frac{\sqrt{2}\, f_t}{c} v_s \sin\theta \tag{30}$$

To determine the doppler bandwidth, the doppler frequencies f_{D_ℓ} and f_{D_u} for the IFOV must be found. This is done by first determining R_{g_ℓ} and R_{g_u} from the equations

$$R_{g_1} = R_{g_n} - L/2 \tag{31}$$

and

$$R_{g_u} = R_{g_n} + L/2 \tag{32}$$

where R_{g_ℓ} and R_{g_u} are the surface distances from the subsatellite point to the upper and lower ends of the IFOV and R_{g_n} is the surface distance to the center of the IFOV for cell number n. R_{g_n} is determined from the equation

$$R_{g_n} = R_{g_1} + (n - 1)\ell_c \tag{33}$$

where R_{g_1} is determined by equations (13) and (5), ℓ_c is determined by (10), and n is the doppler cell number along the beam illumination. Using the values of R_{g_u} and R_{g_ℓ}, the angles θ_u and θ_ℓ can be determined using equations (4) and (5). The dopper bandwidth B_c is then found from

$$B_c = f_{D_u} - f_{D_\ell} \tag{34}$$

Using equation (30) this becomes

$$B_c = \frac{\sqrt{2}\, f_t\, v_s}{c} [\sin\theta_u - \sin\theta_\ell] \tag{35}$$

Having derived the doppler frequency equation we can now derive the equations needed to determine the value of δ. This can be done by solving for the angle ψ (OCA) in triangle AOC of figure A1-5, since by inspection

$\delta = 45^{o} - \psi$ (edge of beam illumination assumed parallel to beam centerline). It is assumed in this derivation that the lines OB and OC are coincident (this is not quite the case, but the deviation from coincidence is small and can be neglected.) Using an equation of the same form as equation (4) and triangle AOC, the equation for ψ is written as

$$\psi = \tan^{-1} \frac{R_{g_n} \sin \phi_g}{R_{g_x} - R_{g_n} \cos \phi_g} \tag{36}$$

To solve for the angle ψ the dimensions R_{g_x}, R_{g_n} and ϕ_g must be determined. R_{g_n} (ground range for cell number n) is determined from equation (33). ϕ_g is determined from the right triangle OAB by the relationship

$$\phi_g = \tan^{-1}\left[\frac{R_{c_n} \phi}{2 R_{g_n}}\right] \tag{37}$$

where R_{c_n} is found for cell n from equation (2), and ϕ is the antenna 3db beamwidth in radians. To determine R_{g_x}, the doppler frequency f_{D_n} for the center of cell n is first calculated. Since the doppler frequency is the same anywhere along line DC, the angle θ_x is found using equation (30);

$$\theta_x = \sin^{-1} \frac{c\, f_{D_n}}{2\, v_s f_t \cos \phi_x} \tag{38}$$

where $\phi_x = \phi' + \phi_g$ (see figure A1-5).

The dimension R_{g_x} is calculated using equations (1), (3) and (5) to obtain

$$R_{g_x} = R\left[\left(\sin^{-1} \frac{R_A \sin \theta_x}{R} - \theta_x\right) \frac{\pi}{180}\right] \tag{39}$$

Now solving for the angle ψ we can obtain the angle δ from

$$\delta = 45 - \psi \tag{40}$$

Mode II

Equations (1) through (5) are applicable for the mode II design. Figure 35 in the main text illustrates the geometry of the surface illumination for mode II. Also included in this figure is an enlarged view of the resolution data cell. The along track dimension of the resolution data cell is determined partly by the doppler bandwidth, which establishes the parameter L, and partly by the smear distance generated during the measurement period. The cross track dimension is formed by $R_c\phi$. Since the antenna beam for mode II is directed along the antenna flight line, the resolution data cell generated is long and narrow. The resolution in this case is defined by the sum of L and the distance $v_g t_p$ traveled during the measurement period, t_p. Any combination of doppler cell length (L) and measurement period (t_p) can be chosen to form the specified resolution length. As shown in appendix 2 it is desirable to maximize the product $B_c \tau_{SN}$, where B_c is the doppler bandwidth, and τ_{SN} is the net integration time for signal plus noise during each measurement period. B_c is a direct function of the parameter L, and τ_{SN} is a function of t_p. For a fixed resolution, r, there is optimum choice of L and t_p which will maximize $B_c \tau_{SN}$. The following derivation shows that this occurs when $t_p v_g = L$.

To determine the optimum choice of L and t_p, an equation for $B_c \tau_{SN}$ is written in terms of L and r. The derivative of this expression with respect to L is taken and set equal to zero. The resulting equation is then solved for L. This is shown as follows. By definition

$$r = L + t_p v_g \qquad (41),$$

or

$$t_p = \frac{r - L}{v_g} \qquad (42);$$

Also

$$\tau_{SN} = \frac{t_p}{T} \tau_P \qquad (43),$$

where T = the pulse repetition period of the transmitted rf pulse, and

τ_P = the pulse width of the transmitted rf pulse. Substituting (42) into (43) we have that

$$\tau_{SN} = \frac{(r - L)\tau_P}{v_g T} \qquad (44).$$

Since at any incidence angle the bandwidth B_c is linearly related to the dimension L, for small changes in L, the following proportionality can be written:

$$\frac{B_c}{B_{c_1}} = \frac{L}{L_1} \qquad (45),$$

or

$$B_c = B_{c_1} \frac{L}{L_1} \qquad (46).$$

The equation for $B_c\tau_{SN}$ is now written as

$$B_c\tau_{SN} = \frac{B_{c_1} \tau_p (r - L)L}{L_1 \; v_g \; T} \qquad (47).$$

Combining all constants and setting them equal to k, equation (47) is written as

$$B_c\tau_{SN} = k\ L\ r - k\ L^2 \qquad (48).$$

To maximize $B_c\tau_{SN}$, we take the derivative of equation (48) and set it equal to 0; thus,

$$\frac{d(B_c\tau_{SN})}{dL} = 0 = k\ r - 2\ k\ L \qquad (49)$$

from which

$$r = 2\ L \qquad (50).$$

Substituting this value of r into equation (41) gives the result

$$L = t_p\ v_g \tag{51}$$

Thus we see to optimize the mode II design for a fixed antenna gain and transmitter power, the measurement period and bandwidth must be chosen so the IFOV length L, equals the integration smear distance, $v_g t_p$.

Since the antenna beam is directed along the satellite direction of flight, the angle ϕ' in equation (29) is zero. Therefore the doppler equation used in mode II calculation becomes

$$f_D = \pm \frac{2\ f_t}{c}\ v_s \sin\theta \tag{52}$$

Similarly the equation for calculating the doppler bandwidth for ϕ' equal to zero degrees, is from equation (35)

$$B_c = \frac{2\ f_t\ v_s}{c}\left[\sin\theta_u - \sin\theta_\ell\right] \tag{53}$$

Earth Rotational Effects

In the final system design, the earth rotational surface velocity must be included along with the satellite velocity in determining the doppler filter frequencies and bandwidths. Figure A1-6 shows a plan view of the satellite track on the surface of the earth along with pictorial views of the beam illuminations at different parts of the orbit. As seen from this figure the orientation of the satellite velocity vector and the antenna beams in respect to the earth velocity vector does not remain the same throughout the orbit. At the peak north and south latitudes, the satellite velocity vector is 180° away from the earth velocity for the retrograde orbit. Throughout the remaining portions of the orbit the satellite velocity vector and antenna beams rotate $\pm 72^\circ$ from this position for a 108° inclined orbit. The 72° orientation occurs at the equator crossings, as shown in figure A1-6.

In the previous derivation of the doppler frequency equation (equation 30) the earth surface velocity was not included. In figure A1-4 the orientation of the earth velocity vector is shown, at the equator, for both the ascending (south to north travel) and descending (north to south travel) directions of the orbit. Note that the earth velocity is shown in the plane of the satellite translated from the doppler cell. Note also that since the projected antenna beams intercept the earth away from the sub-satellite point, the satellite and any particular doppler cell are not at the exact same latitude and longitude. This fact will be neglected in the following derivation of the doppler velocity equation that includes earth velocity. The effects of the latitude and longitude differences will be discussed later.

From equation (26) we have that $v_1 = v_s \cos \phi'$. The earth velocity component (v_2) in the plane of the antenna beam must be combined with v_1 to determine the total doppler velocity v_d. From figure A1-4 we see that for beams 2 and 4,

$$v_2 = v_e \cos \psi_A \text{ (ascending)} \tag{54}$$

and

$$v_2 = v_e \cos \psi_D \text{ (descending)} \tag{55}$$

where v_e = earth rotational surface velocity,
and ψ_A and ψ_D = the angle between the earth velocity and the plane of the antenna beam for the asecnding and descending directions respectively. The earth surface velocity is a maximum at the equator and decreases with increasing latitude, with a value of zero at the poles. The earth surface velocity at any latitude can be shown to be

$$v_e = V_e \cos \phi_L \tag{56}$$

where ϕ_L is the earth latitude angle, and V_e is the earth surface velocity (.465 km/s) at the equator. The doppler velocity v_d to each doppler cell is found from the vector sum of v_1 and v_2 multiplied by the $\sin \theta$. Combining equations (26), (54), (55) and (56) we have for antenna beams 2 and 4,

$$v_d = \pm[v_s \cos \phi' + V_e \cos \phi_L \cos \psi_A] \sin \theta \text{ (ascending)} \qquad (57),$$

and

$$v_d = \pm[v_s \cos \phi' - V_e \cos \phi_L \cos \psi_D] \sin \theta \text{ (descending)} \qquad (58),$$

where the positive value corresponds to the forward antenna (beam 4) and the negative value corresponds to the aft antenna (beam 2). Similarly, equations (57) and (58) also apply to beams 1 and 3 except that the signs in the brackets are reversed. Referring back to figure A1-4 we can see for $\phi' = 45°$, that angles

$$\psi_A = \omega_i - 45^\circ \qquad (59)$$

and

$$\psi_D = 135^\circ - \omega_i \qquad (60)$$

for beams 2 and 4. Similarly for beams 1 and 3,

$$\psi_A = 135^\circ - \omega_i \qquad (61)$$

and

$$\psi_D = \omega_i - 45^\circ \qquad (62).$$

The term ω_i, in these equations, is the angle between the earth's surface velocity and the negative satellite velocity. Equations (59) and (61) apply when v_e is in the 4th quadrant (ascending) and equations (60) and (62) apply when v_e is in the 3rd quadrant (descending), where quadrants are numbered counter-clockwise from beam number 1. As mentioned before, the angle ω_i varies ± 72° throughout the orbit. At any point in the orbit, the angle ω_i can be shown to be a function of the orbit inclination angle α_i and the latitude position (angle ϕ_L) of the satellite. The equation defining the angle ω_i, which can be derived by vector analysis, is given as

$$\omega_i = \cos^{-1}\left[\frac{\cos \alpha_i}{\cos \phi_L}\right] \qquad (63).$$

Combining equations (59) or (61) with (57) and equation (60) or (62) with (58), along with the proper sign choice inside the bracket, and for $\phi' = 45^{\circ}$, the following two equations result which are used to calculate the doppler - velocities on each antenna beam.

$$v_d = \pm[\frac{\sqrt{2}}{2} v_s + V_e \cos \phi_L \cos(\omega_i - 45^{\circ})]\sin \theta \qquad (64),$$

and

$$v_d = \pm[-\frac{\sqrt{2}}{2} v_s - V_e \cos \phi_L \cos(135^{\circ} - \omega_i)]\sin \theta \qquad (65),$$

where ω_i is found from equation (63). In the ascending portion of the orbit, equation (64) is used for beams 2 and 4, and equation (65) for beams 1 and 3. The equations are interchanged for the descending portion of the orbit. Substituting equations (64) or (65) into equation (28) results in the equation for doppler frequency. The equation for the bandwidth, B_c, is obtained by substituting in the resulting expression for f_D into equation (34).

Although a secondary effect in the overall doppler velocity equation, the difference in latitude and longitude location between each doppler cell and the satellite will have to be considered when determining the actual doppler frequency for each data cell (or location of data cell,given doppler frequency). Equations (64), and (65) will have to be modified to account for this effect. In these two equations,the latitude angle ϕ_{Ln} of the particular doppler cell must be used, rather than the latitude angle of the satellite. Also, the second term in the brackets of equations (64) and (65) must be multiplied by a cosine term, which is a function of the longitude difference between the satellite and the particular doppler cell. This correction can be seen by a study of figures A1-4 and A1-6. As seen in figure A1-4, the earth velocity translated from the sub-satellite point is in the same plane -- which is parallel to the surface of the earth -- as the satellite velocity vector. However, when translated from any particular doppler cell, the earth velocity vector will be rotated out of this plane, due to the earth curvature. This rotation occurs because the earth surface velocity vector is always perpendicular to a plane containing the surface point and the axis of rotation. It can be seen that the angle of rotation for the scatterometer case is the difference between longitudes of the satellite and the doppler cell. The second term in the brackets of equations (64) and (65) must be multiplied by the cosine of this angle. Hence, equations (64) and (65) can now be written as

$$V_d = \pm[\sqrt{2}/2\ v_s + V_e \cos \phi_{Ln} \cos \Delta\Omega_{Ln} \cos(\omega_i - 45^\circ)]\sin \theta \quad \text{(Mode I)} \qquad (66),$$

$$V_d = \pm[\sqrt{2}/2\ v_s - V_e \cos \phi_{Ln} \cos \Delta\Omega_{Ln} \cos(135^\circ - \omega_i)]\sin \theta \quad \text{(Mode I)} \qquad (67),$$

where $\Delta\Omega_{Ln}$ is the longitude difference between the sub-satellite point and a doppler cell n, and ϕ_{Ln} is the latitude of doppler cell n.

By similar analysis and by referring to figure A1-4, the equation for the total doppler velocity on doppler cells in Mode II can be written as,

$$V_d = \pm [v_s + V_e \cos \phi_{Ln} \cos \Delta\Omega_{Ln} \cos \omega_i]\sin \theta \quad \text{(Mode II)} \qquad (68).$$

The plus sign corresponds to the antenna directed forward of the satellite and the minus sign for the antenna directed aft of the satellite.

The term in the brackets of equations (66) and (67) is the component of doppler velocity in the plane of the antenna beam parallel to the surface of the earth. This is the velocity v_3 (ascending) shown in figure A1-4. As seen from equations (66) and (67), the absolute value of the velocity component v_3 will vary in opposite directions on each antenna beam throughout the orbit. The variation of this velocity component for each antenna beam is shown in figure A1-7 (effect of latitude and longitude difference neglected in this figure). As seen from this figure the mean of the absolute value of v_3 occurs at the northern and southern latitudes of 72°. At this point in the orbit the value of v_3 is the same on each beam (neglecting the differences that occur due to the difference in the latitude and longitude location of each doppler cell). The peak excursion from the mean value occurs at the equator. The doppler velocity component v_3 will vary approximately ±6% from the mean value (or total of 12%) throughout the orbit (see figure A1-7). The result of this variation will be to shift the location of the data cells in and out along each beam, since only one bank of fixed doppler filters will be provided in the spacecraft. The mean value of velocity v_3 will be used to calculate the doppler filter frequencies and bandwidths. An additional variation of less then 1% on the outer doppler cells and less than .1% on the inner cells will occur, due to the effect of the latitude and longitude difference between the satellite and the doppler cells.

The variation of the velocity v_3 could be made small (within the variation caused by the latitude and longitude differences) by rotating the spacecraft or the antennas by a small amount around the yaw axis, as a function of spacecraft latitude. The effect of this yawing is to compensate for the variable earth velocity vector by varying the component of satellite velocity which contributes to the total doppler velocity. The amount of spacecraft rotation required at each latitude can be found by re-writting the terms in the brackets of equations (64) and (65) as

$$v_3 = \pm [v_s \cos(45 \mp \Delta) + V_e \cos \phi_L \cos(\omega_i - 45^\circ \pm \Delta)] \tag{69}$$

and

$$v_3 = \pm [v_s \cos(45 \pm \Delta) - V_e \cos \phi_L \cos(135^\circ \mp \Delta - \omega_i)] \tag{70}$$

Setting them equal to each other, and solving for the term Δ - where Δ is the amount the S/C or antennas are rotated - in terms of ϕ_L, ω_i, and the satellite and earth velocities, the following equation for Δ results:

$$\tan \Delta = \pm \frac{\cos \phi_L \sin \omega_i}{v_s/V_e + \cos \phi_L \cos \omega_i} \tag{71}$$

The positive sign is used in the descending portion of the orbit and the negative sign in the ascending portion. Solutions for Δ in equation (71), at various latitudes throughout the orbit, show that a maximum rotation requirement of approximately $\pm 3.3^\circ$ occurs at the equator. The value of rotation required decreases with increasing latitude. Zero rotation is required at the northern and southern extremities of the orbit. Substituting the value of Δ into equations (69) and (70) for each latitude shows that less than .2%

variation in the velocity v_3 occurs throughout the complete orbit.

As pointed out in the main text, the orthogonal measurement capability of the scatterometer system is greatly affected by the earth rotation. The orthogonal measurements on a particular surface of the earth are provided by the forward and aft antennas. However, between these measurements, the aft beam illumination must move the distance S_c, the instantaneous surface distance between the forward and aft doppler cell locations. For the baseline design this distance is 450 km for cell number 1 and 1850 km for cell number 15 (see figure 29). For the ground speed of 6.61 km/s, an elapse time of 68 seconds will occur between the orthogonal measurements of data cells number 1 and 280 seconds for data cells number 15. At the equator, during this elapse time period, the surface area measured by the front antenna for cells number 1 and 15 will move 31 and 128 km respectively due to earth rotation. (The remaining data cell measurements will have moved an amount between these two extremes). As the spacecraft travels north or south from the equator the amount of surface movement decreases since the earth surface velocity is decreasing. Figure A1-8 illustrates this effect for various data cells at different latitudes. In this figure the solid and dotted squares represent the location of the aft and forward antenna data cells, respectively, for a given orthogonal measurement pair. The arrows drawn between the aft and forward measurement cells represent the direction and magnitude of movement caused by earth rotation.

The surface distance, S_m, separating the orthogonal measurements for any set of data cells is found from the equation

$$S_m = \frac{S_{cn}}{v_g} V_e \cos \phi_{Ln} \qquad (72).$$

The spacing, S_{cn}, for each data cell is found from equation (11). The angular direction of movement ϕ_m of the front antenna data cell, measured from the satellite subtrack, is approximately

$$\phi_m = \pm (180^\circ - \omega_i) \pm \Delta\Omega_{Ln} \qquad (73).$$

The positive signs are used during the descending portion of the orbit, with counter-clockwise rotation positive, looking down on the earth. Pages 45 and 46 of the main text discuss the effect of nonoverlap of the orthogonal measurements, and recommends a possible solution to this problem.

Before the doppler velocities from equations (66) and (67) can be calculated, the equations for the latitude of the doppler cell (ϕ_{Ln}) and the longitude difference ($\Delta\Omega_{Ln}$) between the satellite and doppler cell must be determined. The equations for these parameters are derived using figures A1-9 and A1-10. The equations for the latitude and longitude differences at the equator are shown in figure A1-9. They are determined from spherical trigonometric relationships for right spherical triangles. For small γ_n ($<15^\circ$), the equations in figure A1-9 can be simplified to the following equations:

Beams 1 and 3

$$\Delta\Omega_{Ln} = |\gamma_n \sin(\omega_i \mp 45^\circ)| \tag{74}$$

$$\Delta\phi_{Ln} = |\gamma_n \cos(\omega_i \mp 45^\circ)| \tag{75}$$

Beams 2 and 4

$$\Delta\Omega_{Ln} = |\gamma_n \cos(\omega_i \mp 45^\circ)| \tag{76}$$

$$\Delta\phi_{Ln} = |\gamma_n \sin(\omega_i \mp 45^\circ)| \tag{77}$$

where $\Delta\Omega_{Ln}$ and $\Delta\phi_{Ln}$ are the longitude and latitude differences, respectively. The minus sign inside the brackets is used for the ascending portion of the orbit and the plus sign for the descending portion. These equations are exact only at the equator. However, for small γ_n angles the latitude of a doppler cell (ϕ_{Ln}) can be approximated by the equation

$$\phi_{Ln} = \phi_L \pm \Delta\phi_{Ln} \tag{78}$$

where $\Delta\phi_{Ln}$ is found using equations (75) and (77). Also it can be shown that $\Delta\Omega_{Ln}$ can be approximated at any longitude by dividing equations (74) and (76) by the $\cos \phi_{Ln}$. The longitude angle, Ω_{Ln}, of a doppler cell is found from

$$\Omega_{Ln} = \Omega_L \pm \Delta\Omega_{Ln} \tag{79}$$

Note, that only the magnitude of $\Delta\phi_{Ln}$ and $\Delta\Omega_{Ln}$, found from their defining equations, should be used in equations (73), (78), and (79). The choice of sign used in equations (78) and (79) is a function of the relative location of the satellite and the doppler cell with respect to the equator and the zero meridian, respectively.

For the larger incidence angles (outer doppler cells) at the higher latitudes the exact equations defining ϕ_{Ln} and $\Delta\Omega_{Ln}$ may be required to determine the doppler cell locations with sufficient accuracy. The exact equations defining ϕ_{Ln} and $\Delta\Omega_{Ln}$ are found from figure A1-10. Using the shaded spherical triangle in figure A1-10 and the law of cosines for sides

$$\phi_{Ln} = \sin^{-1}[\sin \phi_L \cos \gamma_n + \cos \phi_L \sin \gamma_n \cos \alpha] \tag{80}$$

and using the law of sines

$$\Delta\Omega_{Ln} = \sin^{-1}\left[\frac{\sin \alpha \sin \gamma_n}{\cos \phi_{Ln}}\right] \tag{81}$$

where, in the northern hemisphere, α is the angle measured from north to the antenna beam center (measured from south in the southern hemisphere). The angle α is a function of the angle ω_i (angle between the satellite and earth velocity vectors). The equation defining α is found from one of the following equations:

$$\alpha = \omega_i \pm 45° \tag{82}$$

$$\alpha = 135° \pm \omega_i \tag{83}$$

$$\alpha = 225° - \omega_i \tag{84}$$

where the equation choice is based on the hemisphere location of the satellite and the direction of the orbit (descending or ascending). Table A1-2 lists the equation choice for each antenna beam for all portions of the orbit.

Table A1-1 summarizes the equations which have been developed for use in designing the scatterometer. As noted before, the doppler frequency at a specific incidence angle varies throughout the orbit. The mean doppler frequency occurs at the maximum northern and southern latitudes of the satellite orbit, as seen in figure A1-7. However, since the location of an antenna beam changes latitude position with respect to the satellite at the maximum satellite latitudes (see figure A1-6), the mean doppler frequency at any particular incidence angle will be slightly different at these two latitudes extremes. Therefore, for each incidence angle, the doppler frequencies and bandwidths are determined by the average of the mean value calculated at the maximum northern and southern latitudes. This procedure is used in section II of table A1-1 for determining the doppler filter frequencies.

Table A1-2 lists the pertinent equations used for determining the doppler cell location and the parameter L (for use in eq. (5) of the main text), given the doppler filter frequencies and bandwidths. Equation (6) of table A1-2, which determines the angle γ_n, is a transcendental equation which must be evaluated by a digital computer in an iterative process. Three additional equations similar to equation (6) can be written for beams 1 and 3 in the ascending orbit and for beams 2 and 4 in the ascending and descending orbit. The exact equations for the latitude angle, ϕ_{Ln}, and the longitude difference angle, $\Delta\Omega_{Ln}$, are listed in table A1-2. The approximate equation for these parameters (78, 74, 76) could be used for the smaller incidence angles at the lower latitudes, thus simplifying to some extent equation (6), of table A1-2.

TABLE A1-1 SCATTEROMETER DESIGN EQUATIONS

Equation number in text

I. Geometric Equation of Doppler Cell Location

1. $\theta_i = \sin^{-1} \frac{R_A}{R} \sin \theta$ (1)

2. $R_c = \frac{R \sin \gamma}{\sin \theta}$ (2)

3. $\theta = \tan^{-1} [\frac{R \sin \gamma}{R_A - R \cos \gamma}]$ (4)

4. $R_g = \gamma R$, γ in radians (5)

5. $\ell_c = \frac{\pi R}{360} \cos^{-1}[\cos \frac{180 S_s}{\pi R}]^2$ (10)

6. $R_{g_n} = R_{g_1} + (n - 1)\ell_c$ (33)

7. $\gamma_1 = \cos^{-1}[\cos \frac{90}{\pi R} S_s (2n_1 + 1)]^{1/2}$ (13)

8. $n_1 = S_c/S_s - 1/2$, n_1 is nearest whole number to satisfy this equation (12)

9. $S_c = \frac{\pi R}{180} \cos^{-1}(\cos^2 \gamma)$, for $\theta_i = 25^\circ$ (11)

II. Equations for Determining Doppler Filter Frequencies

1. $f_{D_n} = \frac{f_{D_n}(N) + f_{D_n}(S)}{2}$

where $f_{D_n}(N)$ = Doppler frequency for cell n at maximum northern lat.

and $f_{D_n}(S)$ = Doppler frequency for cell n at maximum southern lat.

2. $f_{D_n} = \pm \frac{\sqrt{2} f_t}{c} [v_s + V_e \cos \phi_{Ln} \cos \Delta\Omega_{Ln}] \sin \theta$, Mode I ϕ_L = max. (28), (66) or (67)

TABLE A1-1 (continued)

3. $\phi_{Ln} = \sin^{-1}[\sin \phi_L \cos \gamma_n \pm \frac{\sqrt{2}}{2} \cos \phi_L \sin \gamma_n]$, ϕ_L = maximum (80),(82),(83)
   + maximum northern latitude
   − maximum southern latitude

4. $\Delta\Omega_{Ln} = \sin^{-1}[\frac{\sqrt{2} \sin \gamma_n}{2 \cos \phi_{Ln}}]$, ϕ_L = maximum (81)

5. $f_{L_n} = \pm \frac{2 f_t}{C} [v_s + V_e \cos \phi_{Ln} \cos \Delta\Omega_{Ln} \cos \omega_i] \sin \theta$, Mode II (68)

See Table A1-II for equations defining, ϕ_{Ln}, $\Delta\Omega_{Ln}$, and ω_i for equation (5).

III. Equations for Calculating Parameter L

1. $t_p = \frac{S_s}{N_{OA} \times N_{OP} \times v_g} = \frac{S_s}{8 v_g}$, for 4 antennas, 2 polarizations (16)

2. $\phi_g = \tan^{-1} [\frac{R_{c_n} \phi}{2 R_{g_n}}]$

3. $\theta_x = \sin^{-1} \frac{C f_{D_n}}{2 f_t [v_s \cos \phi_x + \frac{\sqrt{2}}{2} V_e \cos \phi_{Ln} \cos \Delta\Omega_{Ln}]}$ ϕ_L = maximum, $\phi_x = \phi' + \phi_g$ (28), (27) (66)

Note: Use the average values of ϕ_{Ln} and $\Delta\Omega_{Ln}$ calculated for the maximum northern and southern latitudes, use equations II-3 and II-4 of this table.

4. $R_{g_x} = R[(\sin^{-1} \frac{R_A \sin \theta_x}{R} - \theta_x) \frac{\pi}{180}]$ (38)

5. $\psi = \tan^{-1} \frac{R_{g_n} \sin \phi_g}{R_{g_x} - R_{g_n} \cos \phi_g}$ (39)

TABLE A1-1 (concluded).

6. $\delta = 45 - \psi$ (40)

7. $$L = \sqrt{2}\, r - \frac{v_g t_p}{\sqrt{2}} - R_c\phi - \frac{\sqrt{2}\, R_c \phi \sin \delta}{\sin(135 + \delta)}$$ (25)

IV. Equations for Calculating Doppler Bandwidth, B_c

1. $R_{g_\ell} = R_{g_n} - L/2$ (31)

2. $R_{g_u} = R_{g_n} + L/2$ (32)

3. $R_{g_n} = R_{g_1} + (n - 1)\ell_c$ (33)

4. $$\theta_\ell = \tan^{-1}\left[\frac{R \sin \frac{R_{g_\ell}}{R} \frac{\pi}{180}}{R_A - R \cos \frac{R_{g_\ell}}{R} \frac{\pi}{180}}\right]$$ (4), (5), (31)

5. $$\theta_u = \tan^{-1}\left[\frac{R \sin \frac{R_{g_u}}{R} \frac{\pi}{180}}{R_A - R \cos \frac{R_{g_u}}{R} \frac{\pi}{180}}\right]$$ (4), (5), (32)

6. $$B_c = f_{D_u} - f_{D_\ell} = \frac{\sqrt{2}\, f_t}{c} [v_s + V_e \cos \phi_{Ln} \cos \Delta\Omega_{Ln}][\sin \theta_u - \sin \theta_\ell),$$

$$\phi_L = \text{max.}$$ (28), (66)

Note: Use the average values of ϕ_{Ln} and $\Delta\Omega_{Ln}$ calculated for the maximum northern and southern latitudes, use equations II-3 and II-4 of this table.

TABLE A1-2 EQUATIONS FOR LOCATING DOPPLER CELLS

Equation number in text

1. $|f_{D_n}| = \frac{2\ f_t}{C} [\frac{\sqrt{2}}{2} v_s + V_e \cos \phi_{Ln} \cos \Delta\Omega_L \cos(\omega_i - 45^\circ)]\sin \theta_n$ (66), (28)

Ascending - Beams 2 and 4

Descending - Beams 1 and 3

2. $|f_{D_n}| = \frac{2\ f_t}{C} [\frac{\sqrt{2}}{2} v_s - V_e \cos \phi_{Ln} \cos \Delta\Omega_L \cos(135^\circ - \omega_i)]\sin \theta_n$ (67), (28)

Ascending - Beams 1 and 3

Descending - Beams 2 and 4

3. $\omega_i = \cos^{-1}[\frac{\cos \alpha_i}{\cos \phi_L}]$ (63)

4. $\phi_{Ln} = \sin^{-1}[\sin \phi_L \cos \gamma_n + \cos \phi_L \sin \gamma_n \cos \alpha]$ (80)

5. $\Delta\Omega_{Ln} = \sin^{-1}[\frac{\sin \alpha \sin \gamma_n}{\cos \phi_{Ln}}]$ (81)

α Determined as Follows

Northern Hemisphere	Southern Hemisphere
Beam 1 $\alpha = \omega_i \pm 45^\circ - \begin{array}{l} + \text{Desc.} \\ - \text{Asc.} \end{array}$	Beam 1 $\alpha = 225^\circ - \omega_i$ - ASC, $\omega_i \geq 45^\circ$ $\alpha = 135^\circ + \omega_i$ - ASC, $\omega_i < 45^\circ$ $\alpha = 135^\circ - \omega_i$ - DESC
Beam 2 $\alpha = \omega_i \pm 45^\circ - \begin{array}{l} + \text{Asc.} \\ - \text{Desc.} \end{array}$	Beam 2 $\alpha = 135^\circ - \omega_i$ - ASC $\alpha = 225^\circ - \omega_i$ - DESC, $\omega_i \geq 45^\circ$ $\alpha = 135^\circ + \omega_i$ - DESC, $\omega_i < 45^\circ$
Beam 3 $\alpha = 135^\circ - \omega_i$ - DESC $\alpha = 225^\circ - \omega_i$ - ASC, $\omega_i \geq 45^\circ$ $\alpha = 135^\circ + \omega_i$ - ASC, $\omega_i < 45^\circ$	

TABLE A1-2 (concluded)

Beam 4 $\alpha = 135^\circ - \omega_i$ - ASC.

$\alpha = 225^\circ - \omega_i$ - DESC, $\omega_i \geq 45^\circ$

$\alpha = 135^\circ + \omega_i$ - DESC, $\omega_i < 45^\circ$

<u>Mode II</u> $\alpha = 90^\circ - \omega_i$ - ASC

$\alpha = 90^\circ + \omega_i$ - DESC

Beam 3 $\alpha = \omega_i \pm 45^\circ$ + Desc. / - Asc.

Beam 4 $\alpha = \omega_i \pm 45^\circ$ + Asc. / - Desc.

<u>Mode II</u> $\alpha = 90^\circ + \omega_i$ - ASC

$\alpha = 90^\circ - \omega_i$ - DESC

6. $$\frac{C\, f_{D_n}}{2\, f_t} = \sin\left[\tan^{-1}\left(\frac{R \sin \gamma_n}{R_A - R \cos \gamma_n}\right)\right]\left\{\frac{\sqrt{2}}{2} v_s + V_e \cos[\sin^{-1}(\sin \phi_L \cos \gamma_n + \cos \phi_L \sin \gamma_n \cos \alpha)] \times \cos\left[\sin^{-1}\left(\frac{\sin \alpha \sin \gamma_n}{\cos[\sin^{-1}(\sin \phi_L \cos \gamma_n + \cos \phi_L \sin \gamma_n \cos \alpha)]}\right)\right] \times \cos(\omega_i - 45)\right\}$$

Equation 6 is formed from equations 1, 4 and 5 of this table, and $\theta_n = \tan^{-1}\left[\frac{R \sin \gamma_n}{R_A - R \cos \gamma_n}\right]$ - equation I-3 of table A1-1. Equation 6 is used for beams 1 and 3 in the descending orbit. Similar equations can be written for beams 1 and 3 in the ascending orbits and for beams 2 and 4 in the ascending and descending orbit. ω_i is found from equation 3 of this table. α is chosen from the group of equations on the previous page of this table.

The parameters θ_i, R_{c_n} and R_{g_n} can be found from equations I-1, I-2, and I-4 respectively of table A1-1.

7. $\Omega_{Ln} = \Omega_L \pm \Delta\Omega_{Ln}$

8. $L = 2\gamma_u R - 2 R_{g_n}$, γ_u in radians (Equation 32)

9. $\gamma_u = \sin^{-1}(R_A/R \sin \theta_u) - \theta_u$ (equations 1 and 3)

10. θ_u is found from equations 1 or 2 of this table where $|f_{D_N}|$ is replaced with f_{D_u}

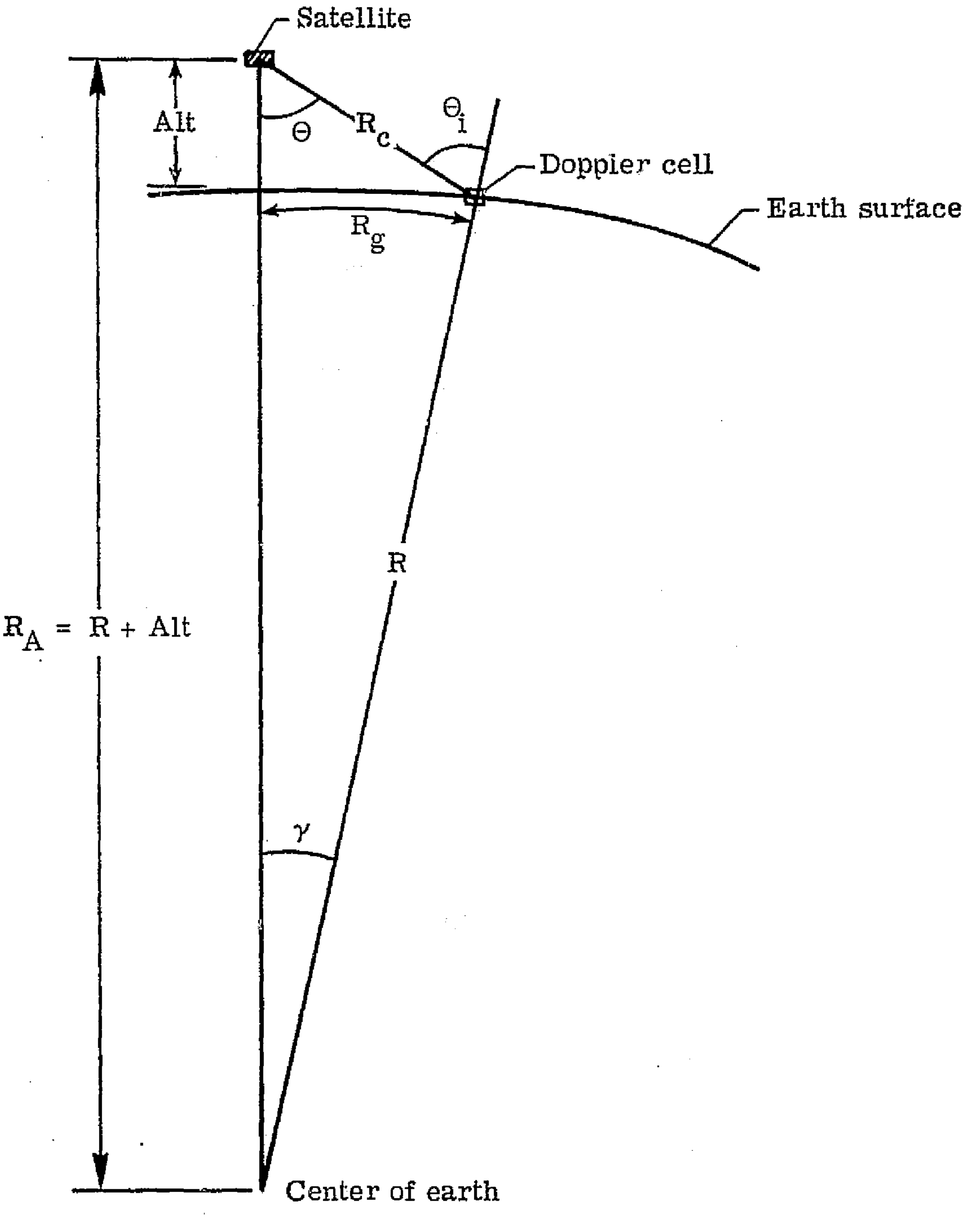

Figure A1-1.- Side view geometry.

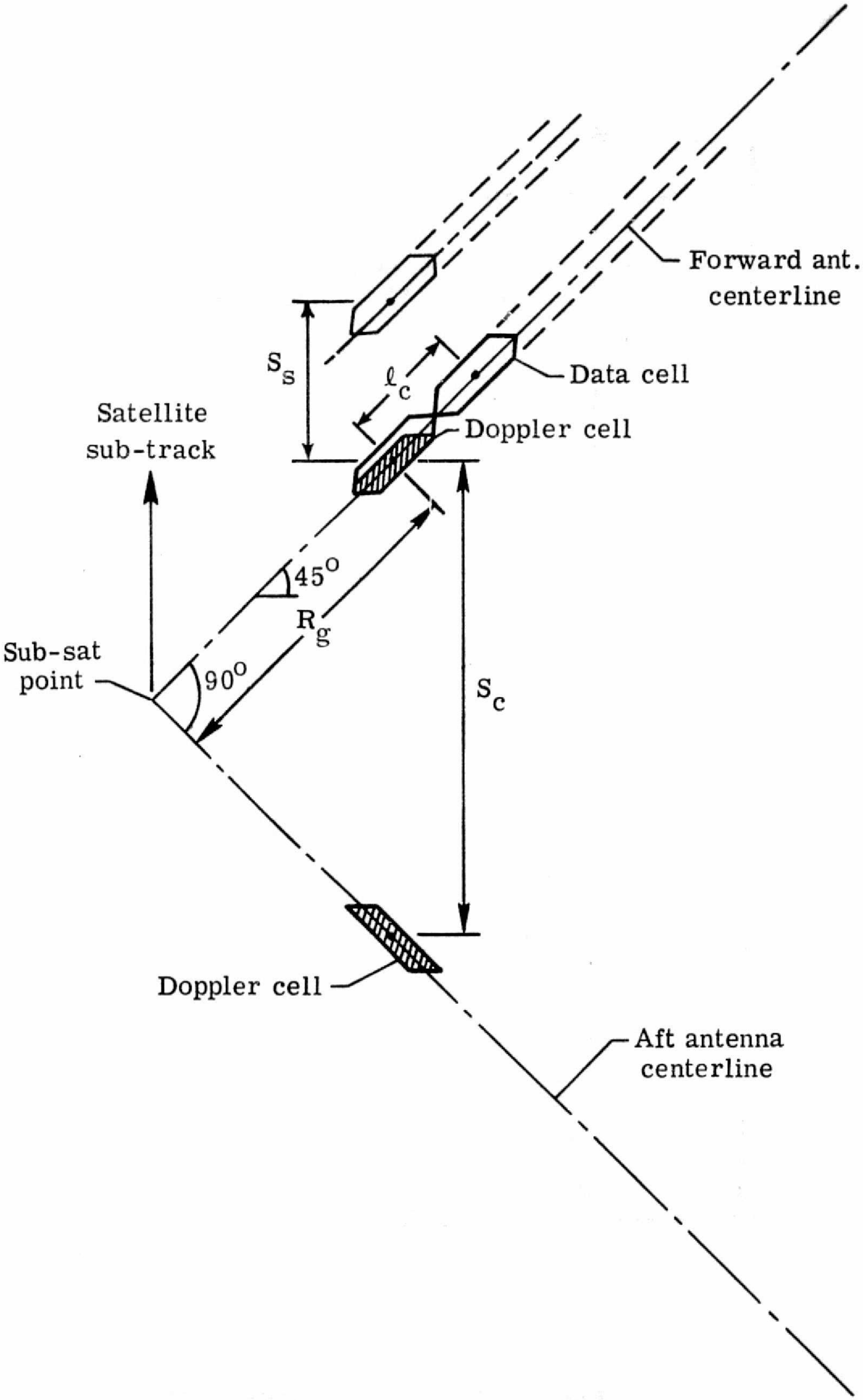

Figure A1-2.- Plan view geometry.

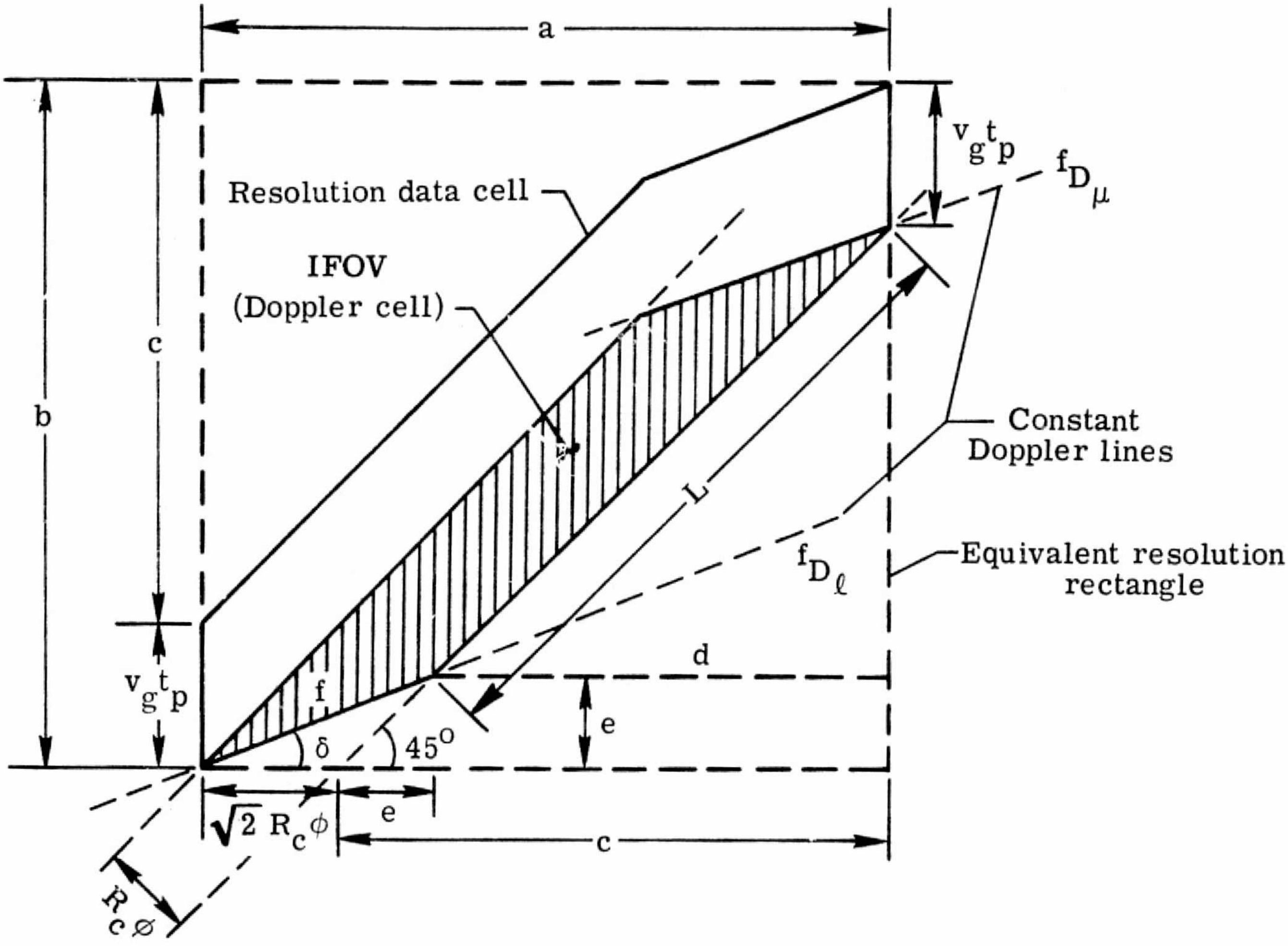

Figure A1-3.- Enlarged view of one resolution data cell.

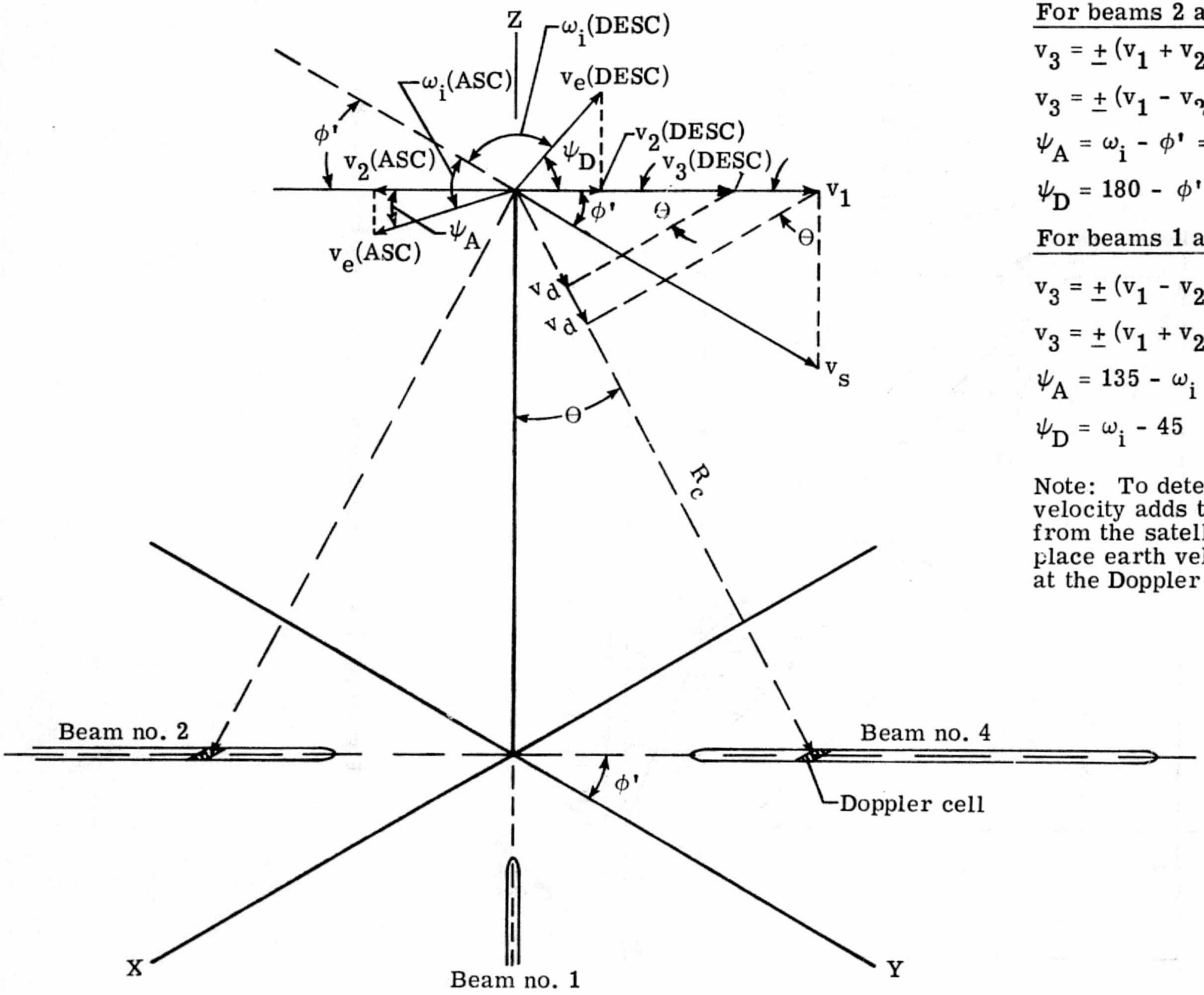

For beams 2 and 4

$v_3 = \pm (v_1 + v_2)$(ASC)

$v_3 = \pm (v_1 - v_2)$(DESC)

$\psi_A = \omega_i - \phi' = \omega_i - 45^\circ$

$\psi_D = 180 - \phi' - \omega_i = 135 - \omega_i$

For beams 1 and 3

$v_3 = \pm (v_1 - v_2)$(ASC)

$v_3 = \pm (v_1 + v_2)$(DESC)

$\psi_A = 135 - \omega_i$

$\psi_D = \omega_i - 45$

Note: To determine if earth velocity adds to or subtracts from the satellite velocity, place earth velocity vector at the Doppler cell

Figure A1-4.- Pictorial view of antenna beam illumination showing satellite and earth velocity relationship at the equator.

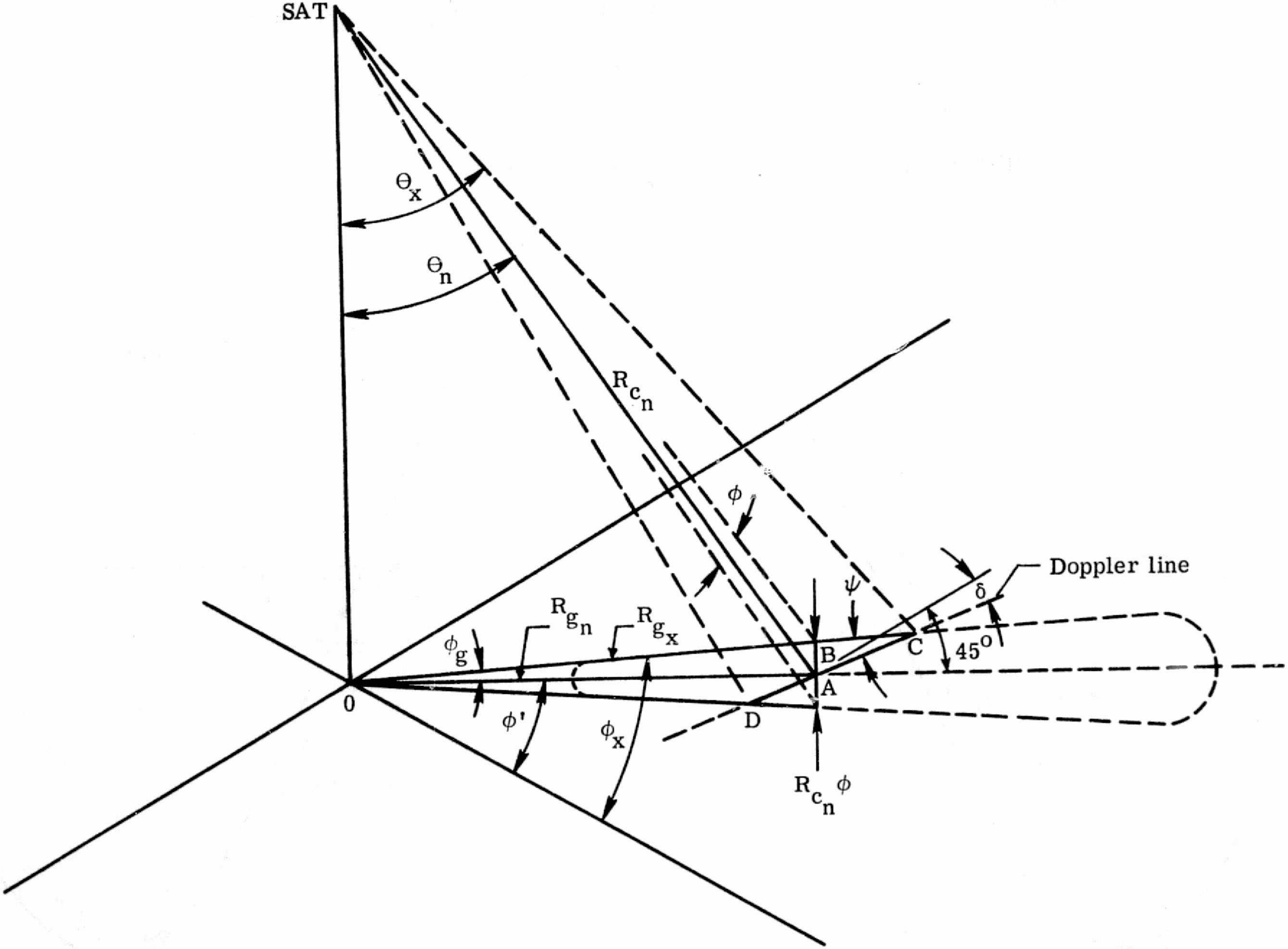

Figure A1-5.- Exaggerated view of beam illumination for deriving the angle δ.

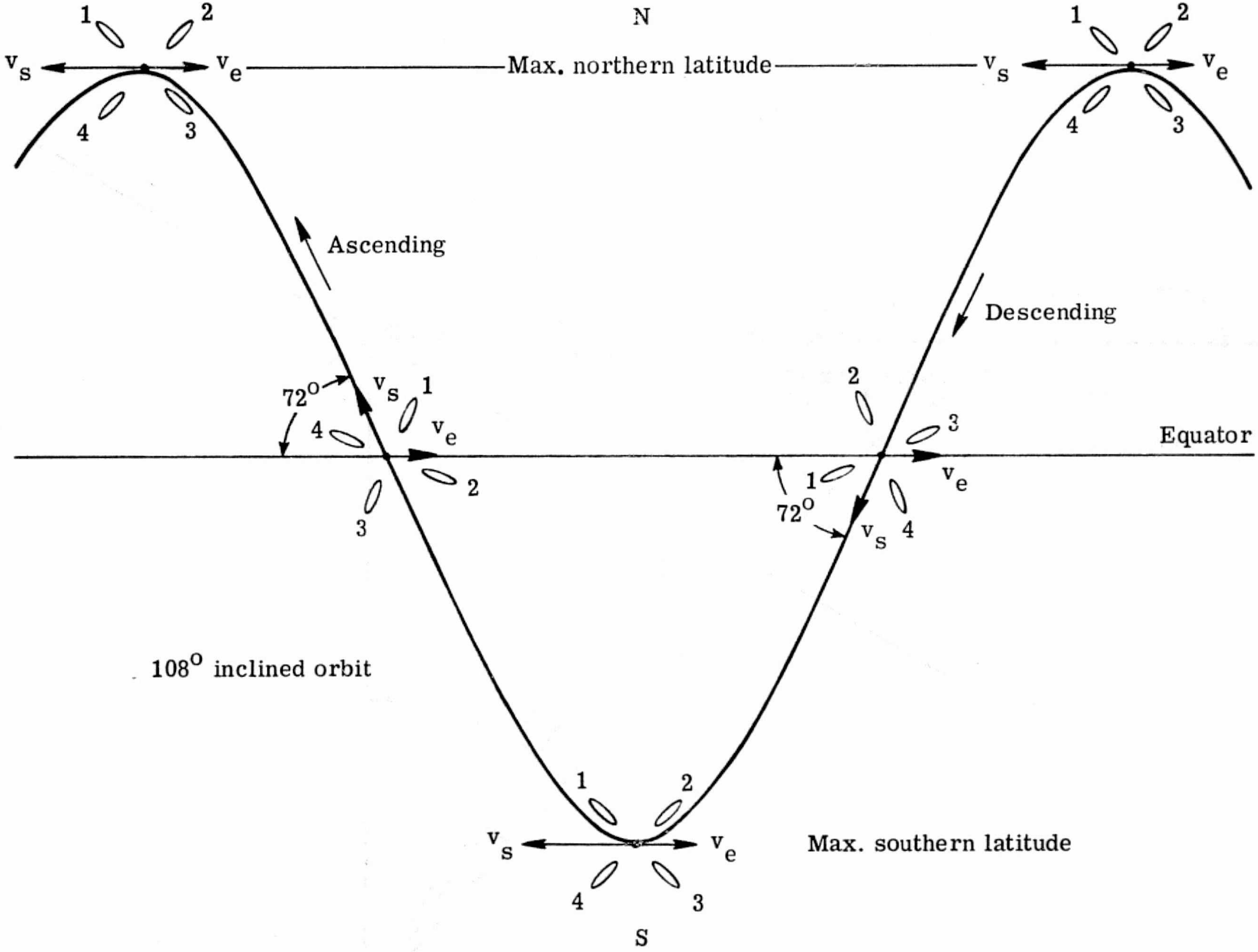

Figure A1-6.- Plan view of satellite track showing pictorial views of the beam illuminations.

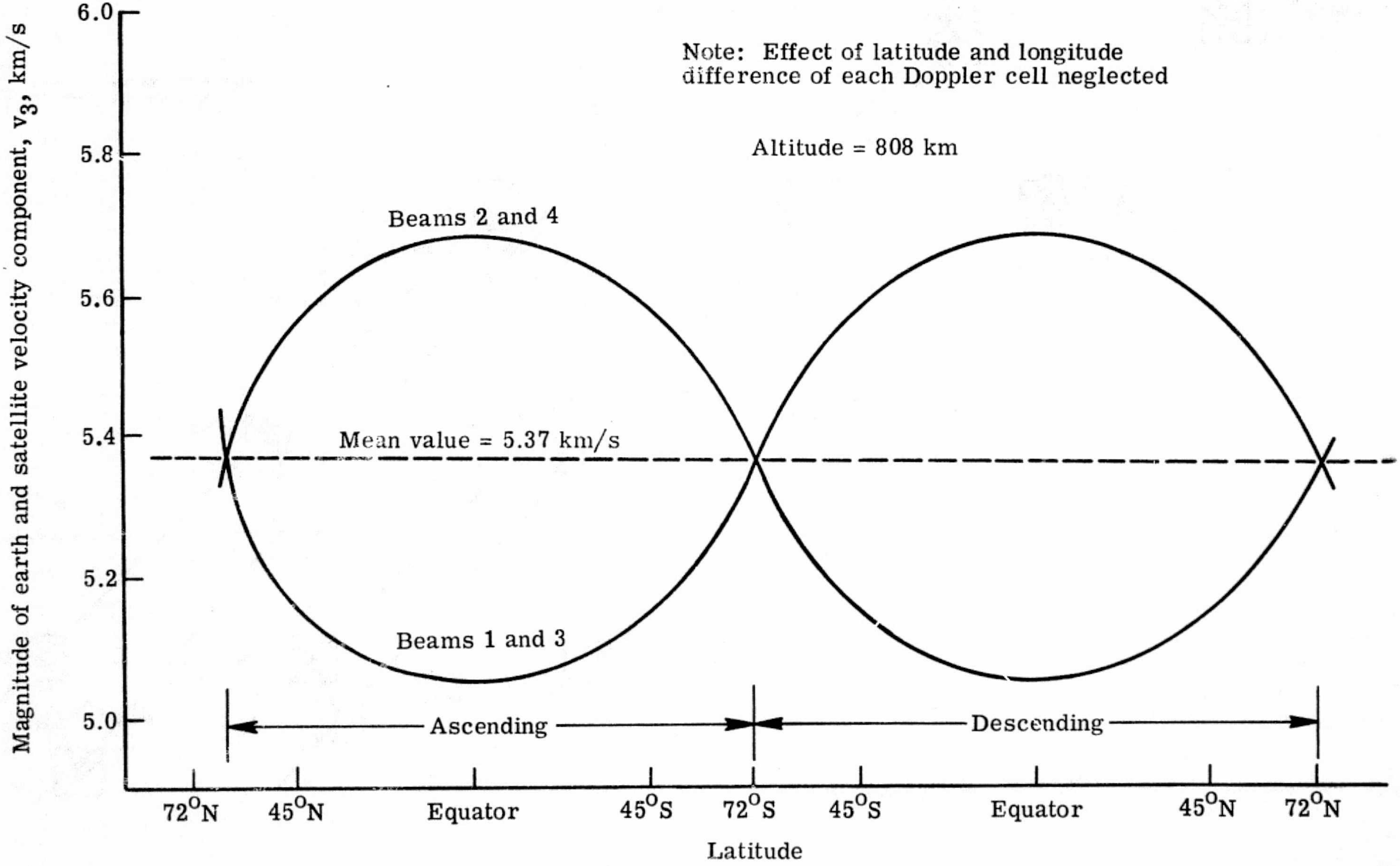

Figure A1-7.- Variation of velocity component, v_3, throughout the orbit.

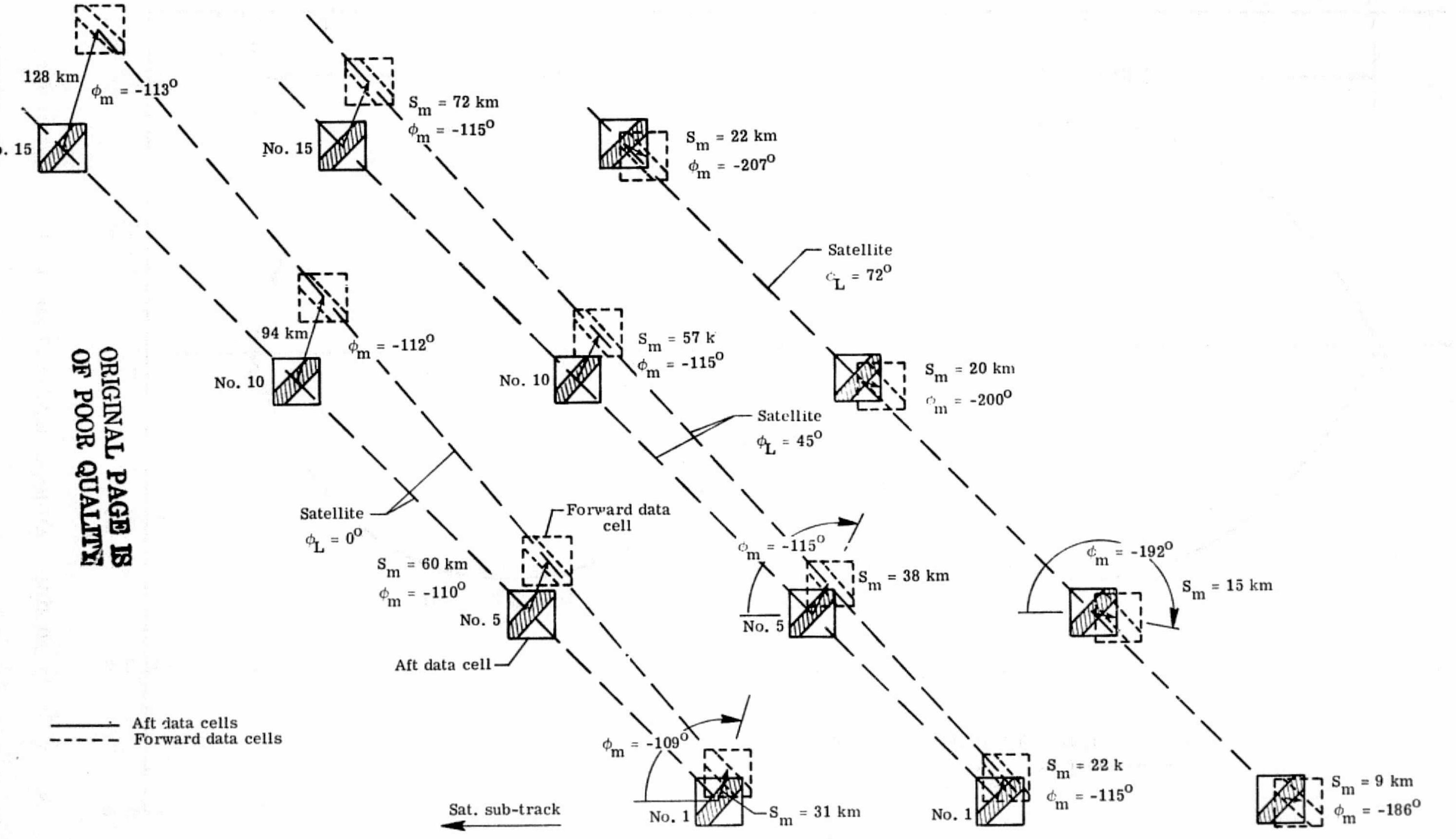

Figure A1-8.- Relative locations of forward and aft data cells (beams 1 and 2) when orthogonal measurement is made – for three satellite latitude locations, ascending portion of orbit.

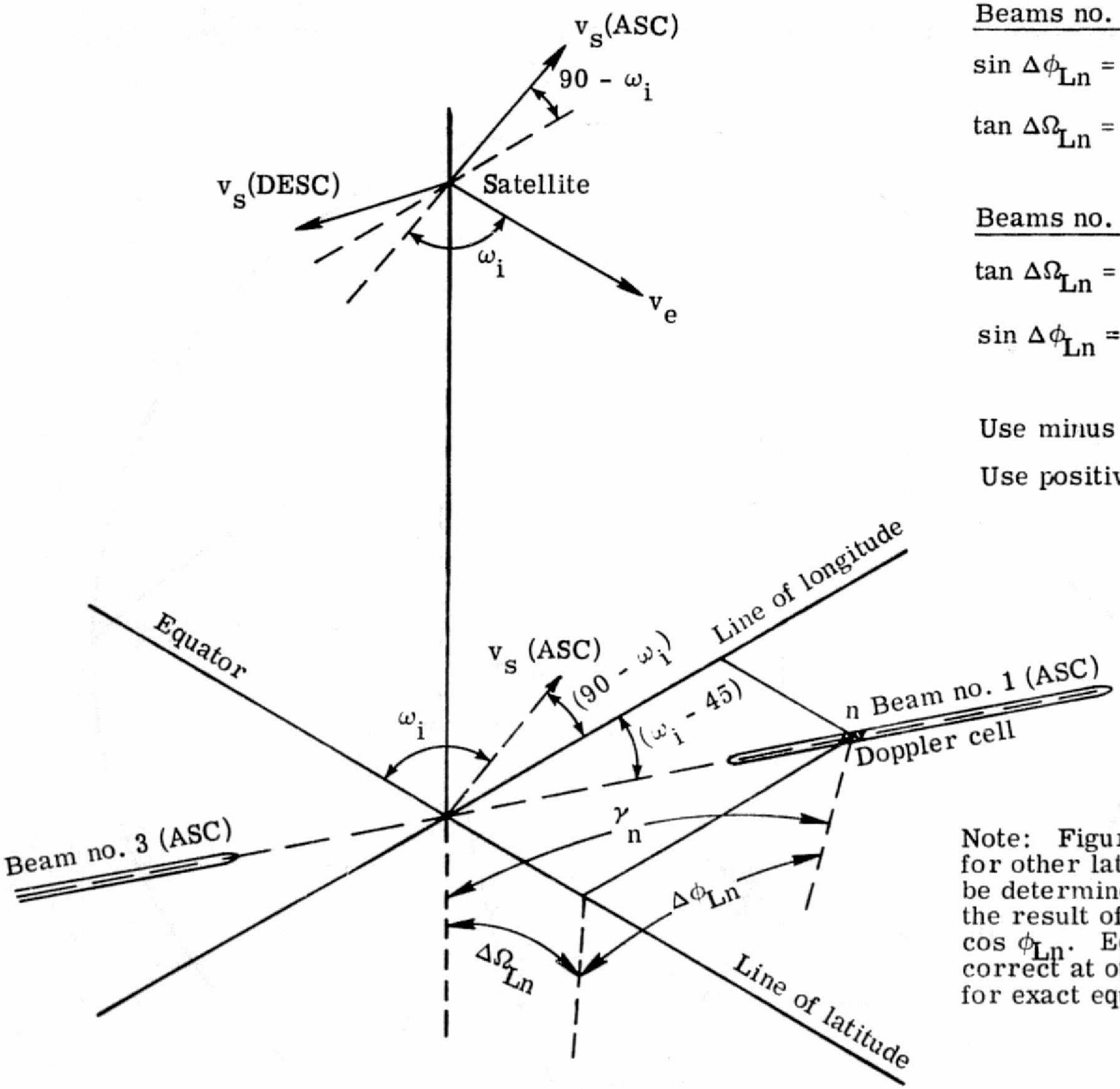

Beams no. 1 and 3

$$\sin \Delta\phi_{Ln} = \sin \gamma_n \cdot \cos(\omega_i \mp 45) \qquad (1)$$

$$\tan \Delta\Omega_{Ln} = \tan \gamma_n \cdot \sin(\omega_i \mp 45) \qquad (2)$$

Beams no. 2 and 4

$$\tan \Delta\Omega_{Ln} = \tan \gamma_n \cdot \cos(\omega_i \mp 45) \qquad (3)$$

$$\sin \Delta\phi_{Ln} = \sin \gamma_n \cdot \sin(\omega_i \mp 45) \qquad (4)$$

Use minus sign for ascending orbit

Use positive sign for descending orbit

Note: Figure drawn for equator crossing - for other latitudes the value of $\Delta\Omega_{Ln}$ can be determined approximately by dividing the result of equations (2) and (3) by $\cos \phi_{Ln}$. Equations (1) and (4) approximately correct at other latitudes. See figure A1-10 for exact equations for $\Delta\Omega_{Ln}$ and ϕ_{Ln}.

Figure A1-9.- Calculation of latitude and longitude difference.

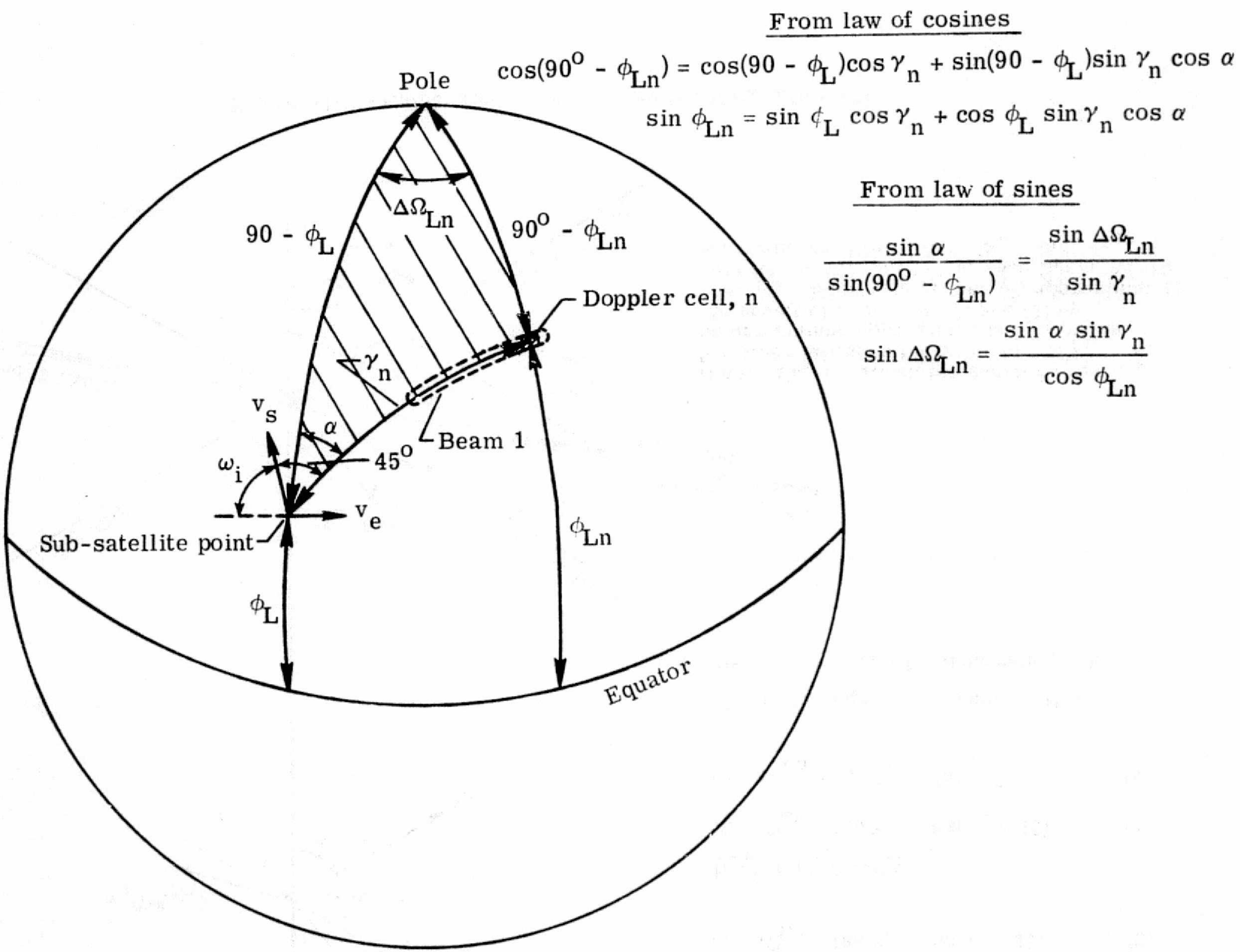

From law of cosines

$$\cos(90^o - \phi_{Ln}) = \cos(90 - \phi_L)\cos\gamma_n + \sin(90 - \phi_L)\sin\gamma_n \cos\alpha$$

$$\sin\phi_{Ln} = \sin\phi_L \cos\gamma_n + \cos\phi_L \sin\gamma_n \cos\alpha$$

From law of sines

$$\frac{\sin\alpha}{\sin(90^o - \phi_{Ln})} = \frac{\sin\Delta\Omega_{Ln}}{\sin\gamma_n}$$

$$\sin\Delta\Omega_{Ln} = \frac{\sin\alpha \sin\gamma_n}{\cos\phi_{Ln}}$$

Figure A1-10.- Spherical triangle used to find latitude (ϕ_{Ln}) and delta longitude ($\Delta\Omega_{Ln}$) of Doppler cell.

APPENDIX 2

DERIVATION OF LINK AND MEASUREMENT ACCURACY EQUATIONS

By E. M. Bracalente

Langley Research Center

Link Equations

The equation (equation (5) in the main text) which determines the value of the radar return signal power can be derived as follows. The power density, P_d, existing on the earth's surface at a doppler cell is

$$P_d = \frac{P_t\ G}{4\ \pi\ R_c^2} \tag{1}$$

where P_t is the transmitter power, G is the antenna gain to the center of the doppler cell and R_c is the slant range from the satellite to the doppler cell. Since the transmitted pulse length is relatively long, the antenna beam is completely filled with the signal. Therefore, the total power radiated back toward the spacecraft from a doppler cell is

$$P_d\ A_c\ \sigma^o = \frac{P_t\ G\ A_c\ \sigma^o}{4\ \pi\ R_c^2} \tag{2}$$

where A_c is the doppler cell area on the surface of the earth and σ^o is the normalized radar scattering coefficient. The power density at the spacecraft is equal to equation (2) divided by $4\pi R_c^2$. The total power at the receiver input is then equal to the product of this power density, the antenna's effective collecting aperture, and any additional system losses, i.e.,

$$P_R = \frac{P_t\ G}{4\ \pi\ R_c^2}\ A_c\ \sigma^o\ \left(\frac{G\lambda^2}{4\ \pi}\right)\ \frac{L_s}{4\ \pi\ R_c^2} \tag{3}$$

where

$\frac{G\lambda^2}{4\pi}$ = antenna effective collecting aperture,

L_s = miscellaneous system losses (ie., two way atmospheric, receiver, and transmitter losses),

$A_c = R_c \phi L$ = doppler cell area,

$G = G_o(\frac{G}{G_o})$ = antenna gain to the center of the doppler cell,

$G_o = \frac{4\pi \; \varepsilon}{\phi\beta}$ = peak antenna gain,

ϕ = 3dB beamwidth across beam,

β = 3dB beamwidth along fan beam,

L = Doppler cell length,

ε = overall antenna efficiency.

Substituting these relationships into equation (3) and rearranging, the following equation for the received power is obtained,

$$P_R = \frac{P_t (G/G_o)^2 \; \sigma^o \; \lambda^2 \; \varepsilon^2 \; L \; L_s}{4\pi \; R_c^3 \; \phi \; \beta^2} \qquad (4).$$

The received signal-to-noise ratio from a doppler cell is,

$$S/N = \frac{P_R}{K \; T_s \; B_c} \qquad (5),$$

where T_s is the system noise temperature and B_c is the I.F. bandwidth which equals the doppler spread bandwidth across one doppler cell. The system noise temperature, T_s, can be referred to either the input to the rf preamplifier or at the antenna terminals. Either place is correct, but if T_s is referred to the preamplifier input, the loss factor L_R must be included in the link equation. If T_s is referred to the antenna terminals, the factor L_R is not included in the link equation. Figure A2-1 shows the derivation of the equations for both of these cases.

<u>Derivation of the parameter K_p</u>

As shown in figure A2-2, a gated integrator is used to average the output of a square law detector over a number of return radar pulses. This measurement $\hat{P}_{SN}$ is an estimate of the mean return signal plus noise power. Next, a measurement of the antenna and receiver mean noise power $\hat{P}_N$ is made by integrating the square law detector output in the absence of the radar return pulse. $\hat{P}_R$ is obtained from these quantities by

$$\hat{P}_R = \hat{P}_{SN} - \hat{P}_N \qquad (6).$$

If $\hat{P}_{SN}$ and $\hat{P}_N$ are assumed to be independent, then the standard deviation σ_M of $\hat{P}_R$ is

$$\sigma_M = [\sigma_{SN}^2 + \sigma_N^2]^{1/2} \qquad (7)$$

where $\sigma_{SN}^2 = (\text{Var } \hat{P}_{SN})$ = the variance of the measurement of signal plus noise, and

$\sigma_N^2 = (\text{Var } \hat{P}_N)$ = the variance of the measurement of noise only.

Referring to figure A2-2, the equations for the variances σ_{SN}^2 and σ_N^2 can be determined as follows. Davenport and Root[33] shows that a Gaussian signal uniformly distributed over a bandwidth B_c, has a triangular spectrum at the output of a square law detector and low pass filter. As illustrated in figure A2-2, the peak value of this distribution is $P_D^2 B_c$, where P_D is the one sided power spectral density of the signal in the bandwidth B_c. The distribution decreases linearly to zero at a frequency of $\pm B_c$, from this peak. The mean value of the signal is equal to $P_D B_c$.

The radar return signal is assumed to be a Gaussian random process uniformly distributed over the bandwidth B_c. The power density for this signal is P_R/B_c. The power density of the antenna and receiver noise, which is also uniformly distributed and Gaussian, is KT_s, where K is Boltzman's constant. For signal plus noise, then,

$$P_D = KT_s + P_R/B_c, \qquad (8)$$

and for noise only,

$$P_D = KT_s \qquad (9).$$

The spectrum at the output of the gated integrator is shown in figure A2-2. It has a $(\sin x/x)^2$ distribution. The variance, σ^2, at the output of the integrator is equal to the integral of the $(\sin x/x)^2$ function times the input spectrum, i.e.,

$$\sigma^2 = 2 \int_0^{B_c} S_N(f) H(f) df \qquad (10)$$

where $S_N(f)$ is the spectrum input to the integrator,

$$S_N(f) = P_D^2(B_c - f), \text{ (see figure A2-2)} \qquad (11)$$

and $H(f)$ is the power transfer function of the gated or running mean integrator,

$$H(f) = \frac{\sin^2 (f\tau)}{(f\tau)^2} \qquad (12),$$

where τ is the total integration time. Substituting equations (8), (11), and (12) into (10), the variance σ^2_{SN} for signal plus noise is

$$\sigma^2_{SN} = 2(KT_s + P_R/B_c)^2 \, B_c^2 \int_0^{B_c} \left(\frac{1}{B_c} - \frac{f}{B_c^2}\right) \frac{\sin^2(\pi\tau_{SN} f)}{(\pi\tau_{SN} f)^2} df \qquad (13).$$

For $B_c \tau_{SN} > 100$, equation (13) reduces to

$$\sigma^2_{SN} = (KT_s + P_R/B_c)^2 \, B_c^2 \frac{1}{B_c \tau_{SN}} \qquad (14)$$

$$= [(KT_s B_c)^2 + 2KT_s B_c P_R + P_R^2] \frac{1}{B_c \tau_{SN}} \qquad (15).$$

The mean noise power P_N, is $P_D B_c$ (i.e., $KT_s B_c$), and the mean signal plus noise power P_{SN}, is $KT_s B_c + P_R$. The mean signal power is $P_{SN} - P_N = P_R$. Using the symbol N for the mean noise power, $KT_s B_c$, and the symbol S for the mean signal power, P_R equation (15) becomes

$$\sigma^2_{SN} = (N^2 + 2NS + S^2) \frac{1}{B_c \tau_{SN}} \qquad (16).$$

In terms of the N/S ratio, equation (16) can be written as

$$\sigma_{SN}^2 = S^2[(N/S)^2 + 2\ N/S + 1]\ \frac{1}{B_c\tau_{SN}} \qquad (17).$$

Similarly the equation for the variance of the noise σ_N^2, is

$$\sigma_N^2 = N^2\ (\frac{1}{B_c\tau_N}) \qquad (18).$$

In terms of N/S this equation becomes

$$\sigma_N^2 = S^2[(N/S)^2\ \frac{1}{B_c\tau_N}] \qquad (19).$$

Equations (16) and (18) can be found in another way by defining the transfer function of the integrator by its equivalent bandwidth. As shown in figure A2-2, the equivalent bandwidth of the integrator is $1/\tau$. For $B_c\tau > 100$ the power density $P_D B_c$ of the input signal to the integrator can be assumed constant across this equivalent bandwidth. The output power of the integrator (i.e. the variance of the signal σ^2) is $P_D^2 B_c/\tau$. Substituting in the signal plus noise power density for P_D, equation (16) is obtained, and substituting in the noise power density for P_D, equation (18) is obtained.

The standard deviation of the measurement $\hat{P}_R$, can now be obtained by substituting equations (17) and (19) into equation (7); thus,

$$\sigma_M = S[\frac{1}{B_c\tau_{SN}}\ (N^2/S^2 + 2\ N/S + 1) + \frac{1}{B_c\tau_N}\ \frac{N^2}{S^2}]^{1/2} \qquad (20).$$

Dividing through by S we have the normalizing factor, K_p, which gives the standard deviation of the estimate of P_R as a proportion of the true value of P_R. That is,

$$K_p = \frac{\sigma_M}{S} = [\frac{1}{B_c\tau_{SN}}\ (\frac{N^2}{S^2} + 2\ N/S + 1) + \frac{1}{B_c\tau_N}\ \frac{N^2}{S^2}]^{1/2} \qquad (21).$$

The integration time τ_N, will be some multiple of τ_{SN} so that the term $K_t = \tau_N/\tau_{SN}$ can be introduced in equation (21); i.e.,

$$K_P^2 = \frac{1}{B_c \tau_{SN}} \left(1 + 2\ N/S + \frac{N^2}{S^2}\left[1 + \frac{1}{K_t}\right]\right) \tag{22}$$

In general, as the integration time for noise τ_N is made longer, the standard deviation of the measurement will become smaller. The total integration time for the signal plus noise is a function of the transmitted pulse period τ_P, pulse repetition period T, and the measurement period t_p, and the noise measurement is performed during the off period between transmission pulses (see figure 27). The signal plus noise integration period τ_{SN}, will become smaller as τ_N is increased, thus increasing the standard deviation of the measurement. There is, however, an optimum choice of K_t which will minimize the required S/N (maximum N/S) for any given measurement accuracy, K_p. By solving equation (22) for N/S, i.e.,

$$N/S = K_p (B\tau_{SN})^{1/2} \left(\frac{K_t}{K_t + 1}\right)^{1/2} - \frac{K_t}{K_t + 1} \tag{23}$$

and substituting in the equation for τ_{SN} (from figure 27)

$$\tau_{SN} = \frac{t_P\ \tau_P}{\frac{2R_{cmax}}{c} + K_t(\tau_P + 1) + t_m} \tag{24}$$

the value of K_t which gives the maximum N/S can be determined. The conventional means of determining the optimum value of K_t -- i.e., setting the derivative of equation (23) equal to zero and solving for K_t -- results in a high order equation that is difficult to solve. A simpler approach, to determining an optimum value of K_t, is through a graphical plot of the numerical evaluation of equation (23). Using a K_p of .5, and the baseline design values for the various times in equation (24), and the bandwidths for doppler cells 1, 5, and 10, the graphs shown in figure A2-3 were determined. From these curves we see that the peak N/S occurs at a K_t of approximately 1.75. Also, the values of N/S are relatively constant for K_t values from

1 to 3. As a result a K_t value of 2 was used in the baseline design.

Processing Multiple Data Cells to Obtain Improved Measurement Accuracy

It may be desirable to improve the measurement accuracy at the expense of resolution by averaging the measurements from multiple data cells. For example, this may be done in the high resolution design by averaging two adjacent 25 km resolution data cells to obtain a 50 km resolution measurement that has a standard deviation less than those for the 25 km cells. This is shown as follows. Let

$$K_{p1} = \frac{\sigma_{M1}}{\sigma_1^o} \tag{25}$$

and

$$K_{p2} = \frac{\sigma_{M2}}{\sigma_2^o} \tag{26}$$

be the normalized standard deviation of two adjacent cells. The errors σ_{M1} and σ_{M2} can be assumed to be independent. The average measurement of σ^o for the two adjacent cells is defined as,

$$\sigma_a^o = \frac{\sigma_1^o + \sigma_2^o}{2} \tag{27}$$

The standard deviation on this measurement will be

$$\sigma_{Ma} = 1/2\ (\sigma_{M1}^2 + \sigma_{M2}^2)^{1/2} \tag{28}$$

Substituting from equations (25) and (26), equation (28) becomes

$$\sigma_{Ma} = 1/2[(K_{P1}\sigma_1^o)^2 + (K_{P2}\sigma_2^o)^2]^{1/2} \tag{29}$$

The normalized standard deviation, K_{pa}, will be

$$K_{Pa} = \frac{\sigma_{Ma}}{\sigma_a^o} \tag{30}$$

$$= \frac{[(K_{P1}\sigma_1^o)^2 + (K_{P2}\sigma_2^o)^2]^{1/2}}{\sigma_1^o + \sigma_2^o} \tag{31}$$

Assuming $\sigma_1^o = \sigma_2^o$ (which is generally valid),

$$K_{pa} = 1/2\ (K_{p1}^2 + K_{p2}^2)^{1/2} \tag{32}$$

If $K_{p1} = K_{p2} = K_p$, then

$$K_{pa} = \frac{K_p}{\sqrt{2}} \tag{33}$$

For averaging a multiple number of data cell measurements, equation (32) can be written as

$$K_{pa} = 1/n\ (K_{p1}^2 + K_{p2}^2 + K_{p3}^2 + \ldots K_{pn}^2)^{1/2} \tag{34}$$

If all the K_p's in equation (34) are equal, which would generally be the case for measurements from contiguous data cells at a constant incidence angle, then equation (34) becomes

$$K_{pa} = \frac{K_p}{\sqrt{n}} \tag{35}$$

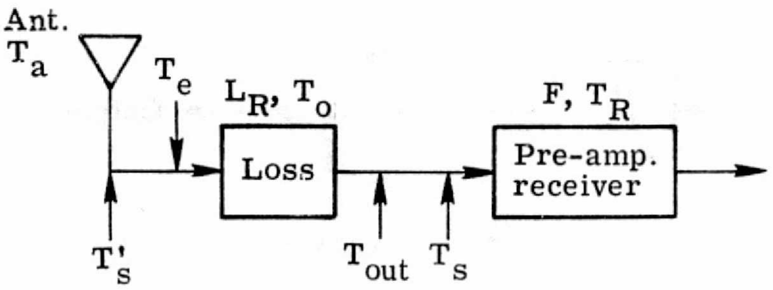

T_a = ant. noise temp.

T_o = amb. temp. of loss

L_R = loss factor = $\frac{\text{input}}{\text{output}}$

T_R = pre-amp-rec input noise temp.

F = pre-amp-rec noise figure

T_s = system noise temp. referred to pre-amp input

T'_s = system noise temp. referred to ant. terminals

Case I - Equation for T_s

$$T_s = T_{out} + T_R \quad (1)$$

$$T_{out} = \frac{T_a}{L_R} + (1 - \frac{1}{L_R})\, T_o \quad (2)$$

– Output noise temp. of a loss with input termination having noise temp., T_a - see ref. 32

$$T_R = T_o(F - 1)$$

$$T_s = \frac{T_a}{L_R} + (1 - \frac{1}{L_R})T_o + T_o(F - 1) \quad (4)$$

$$T_s = \frac{T_a}{L_R} + \frac{T_o}{L_R}(L_R F - 1) \quad (5)$$

– Loss L_R must be included in link calculation

Case II - Equation for T'_s

$$T'_s = T_a + T_e \quad (6)$$

$$T_e = (L_R - 1)T_o + L_R T_R \quad (7)$$

– Input noise temp. to loss cascaded with amplifier - see ref. 32

$$T'_s = T_A + (L_R - 1)T_o + L_R T_R \quad (8)$$

since $T_R = T_o(F - 1)$

Then $T'_s = T_a + T_o(L_R F - 1)$

– Loss L_R not included in link calculation

Figure A2-1.- Derivation of system noise temperature equation.

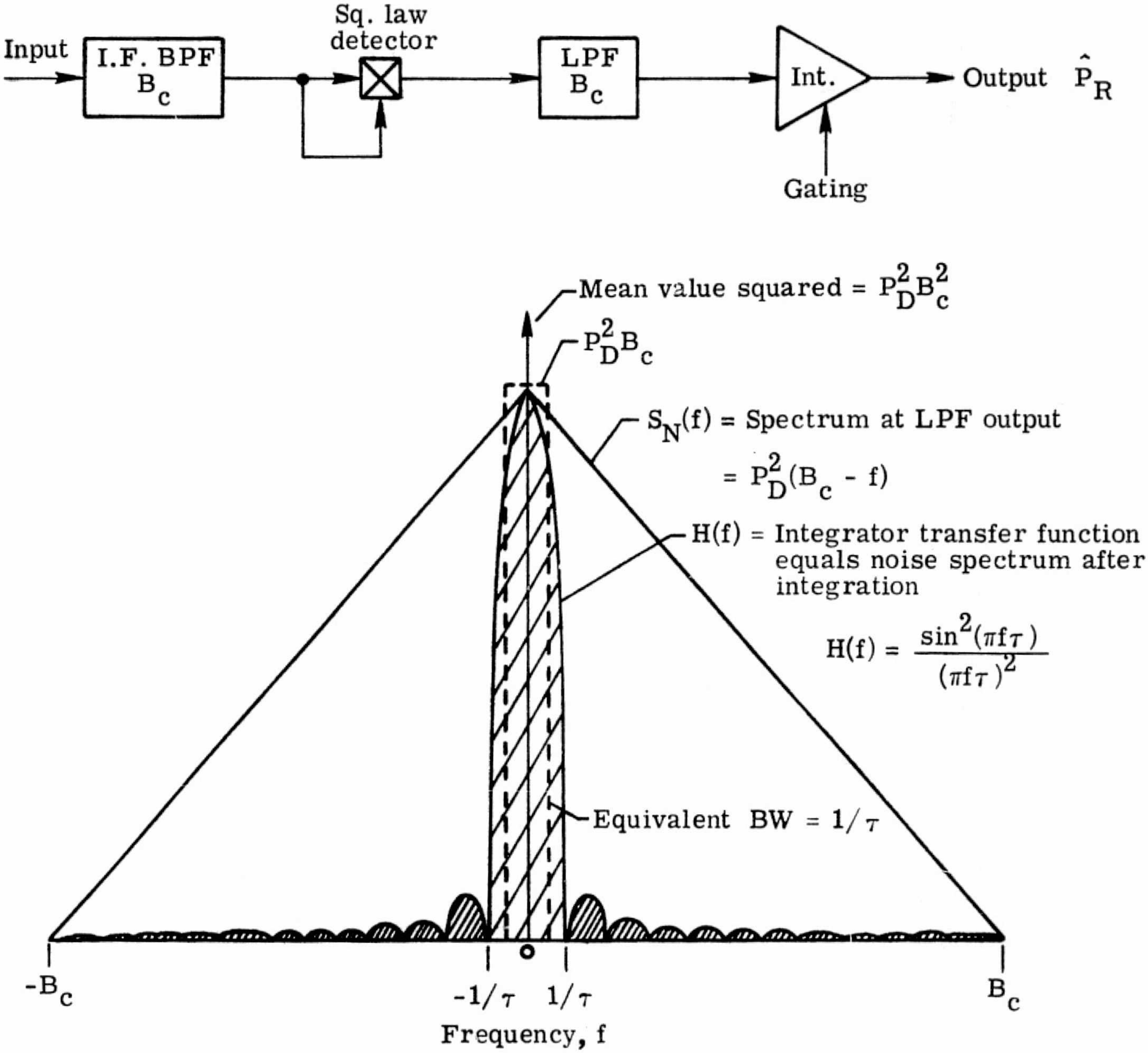

Radar return signal and receiver noise assumed as Gaussian signals, uniformly distributed in I.F. BW B_c

For signal plus noise $\quad P_D = KT_s + P_R/B_c$

For noise only $\quad P_D = KT_s$

$$\hat{P}_R = \hat{P}_{SN} - \hat{P}_N = KT_sB_c + P_R - KTB_c = P_R$$

Figure A2-2.- Spectrum at output of square law detector and gated integrator.

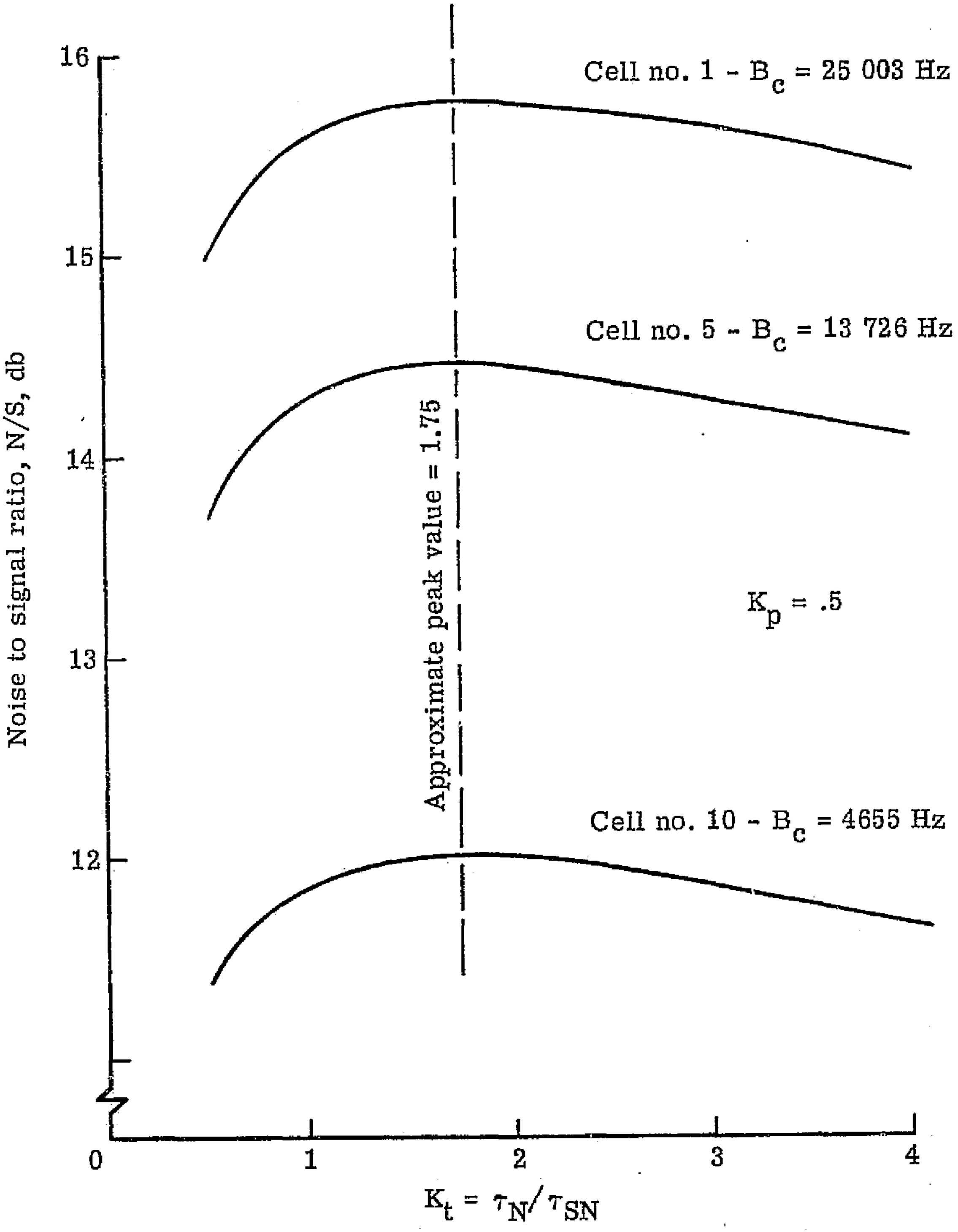

Figure A2-3.- N/S requirement as a function of τ_N/τ_{SN} ratio.

APPENDIX 3

FAN BEAM ANTENNA

By Dr. M. C. Bailey
Langley Research Center

This appendix presents the configuration and characteristics of a fan beam antenna, with application to the SeaSat A Satellite Scatterometer.

DISCUSSION

The basic antenna configuration is illustrated in figure A3-1. It consists of an array of pyramidal horns which are corrugated on two sides in order to produce equal beamwidths in the plane transverse to the array (ref. A3-1). For Mode I operation, the transverse dimension of the horn aperture (5.6 cm at 13.9 GHz) is chosen so as to produce a 25° half-power beamwidth. The array would have to be about 2.7 meters long (107 horns) at 13.9 GHz in order to obtain a 0.5° half-power beamwidth in the longitudinal plane with −30 dB sidelobes.

The horn array elements are coupled to a square feed waveguide through centered crossed slots. When the feed waveguide is excited by orthogonally polarized waves (through a waveguide orthomode coupler), the two arms of the cross slot provide the isolation and excitation for the radiating horn dual polarization. The tapered array illumination (for sidelobe reduction) is achieved by varying the slot size (slot-to-waveguide coupling (ref. A3-2)) along the feed waveguide.

The computed radiation pattern in the transverse (yz) plane for the array of figure A3-1 is shown in figure A3-2 for the aperture electric field polarized along the x-axis (longitudinal to the array). This pattern is that of an H-plane flared horn (ref. A3-3) since the corrugations only affect the electric field which is polarized normal to the corrugated surface. With proper design of the corrugations (ref. A3-4), the yz-plane pattern for the other polarization should be very similar.

The array pattern in the longitudinal (xy) plane is determined primarily by the number of elements (N_{el}), the horn spacing (d), the phase difference between adjacent elements (Δ), the element excitation distribution (C_n), and the element pattern ($F(\Phi)$) as

$$E(\Phi) = F(\Phi) \sum_{n=1}^{N_{el}} C_n \exp(j(n-1)\ (\Delta - 2\pi d/\lambda \sin \Phi)) \tag{1}$$

where Φ is the angle measured off the z-axis and λ is the free space wavelength.

The radiation pattern is a maximum when the phase difference between the far-field signals of adjacent elements is an integral number of wavelengths, i.e.,

$$(\Delta - 2\pi d/\lambda \sin \Phi_m) = 2\pi m \qquad m = 0, \pm 1, \pm 2, \ldots \tag{2}$$

where Φ_m is the direction of the corresponding field maximum.

In a slotted waveguide array, the phase difference between adjacent elements is determined by the slot spacing (s) and the guide wavelength (λ_g), i.e.,

$$\Delta = 2\pi s/\lambda_g. \tag{3}$$

Since the slot spacing is equal to the horn spacing (s = d), substituting (3) into (2) and rearranging gives

$$\sin \Phi_m = \lambda/\lambda_g - m\lambda/d. \tag{4}$$

There may be more than one value of m which will yield real values for Φ_m, corresponding to different beam maxima or "grating lobes." The position of the m = 0 lobe is independent of the element spacing as seen from (4) with m = 0, i.e.,

$$\sin \Phi_o = \lambda/\lambda_g. \tag{5}$$

However, within the normal bandwidth of rectangular or square waveguide ($0.5 \leq \lambda/\lambda_g \leq 0.866$), the beam direction for the $m = 0$ lobe is restricted to the range of 30° to 60° from broadside. A broadside beam can be obtained, however, by selecting a slot spacing such that $\sin \Phi_m = 0$ for one of the other lobes. Then (4) gives, for a broadside beam,

$$d = m\lambda_g . \tag{6}$$

Thus, by choosing a slot spacing equal to the guide wavelength of the feed waveguide, the peak of the $m = 1$ lobe will be in the desired direction. This is the criterion used for the design of the feed waveguide dimension and slot spacing of the array in figure 1. The value of λ/λ_g was chosen so as to separate the $m = 0$ lobe as far as practical ($\Phi_o = 59^\circ$) from the broadside beam.

The xz-plane pattern for the array configuration of figure A3-1 with 107 elements and with a -30 dB Taylor distribution (ref. A3-5) is shown in figure A3-3. This pattern was computed from (1) with $\Delta = 2\pi$ and $d = 1.165\lambda$. In addition to the $m = 0$ and $m = 1$ lobes, the $m = 2$ lobe is also present at an angle of 59° from broadside, toward the feed end of the array. The level of the lobes at 59° from broadside are determined by the horn element pattern at the corresponding angle. These lobes will be about -9 dB for the electric field polarized transverse to the array, and about -16 dB (or lower) for the orthogonal polarization.

A rough estimate indicates that the return signal due to the "grating lobes" at 59° from broadside may be sufficiently reduced by the longer path length and smaller radar scattering cross-section of the surface so as not to cause any significant interference problem at an altitude of 808 km.

An alternate configuration is illustrated in figure A3-4 in which the array of corrugated horns of figure A3-1 have been replaced by a corrugated trough. The radiation patterns should be very similar to those of the array of corrugated horns; however, the cost of fabricating a 2 to 3 meter long antenna may be appreciably reduced by selecting the corrugated trough design.

For Mode II operation, which requires a $1/2^\circ \times 40^\circ$ beamwidth, the basic antenna configuration can be modified by cutting off the horn elements (or the trough for the alternate configuration) such that the transverse aperture dimension is 3.95 centimeters instead of 5.6 centimeters. The tapered length then becomes 5.2 centimeters instead of 11.0 centimeters. These dimensions are illustrated on figure A3-4 for the corrugated trough antenna.

REFERENCES

A3-1. R. Lawrie and L. Peters, Jr.; "Modifications of Horn Antennas for Low Sidelobe Levels." IEEE Trans. Ant. and Prop., September 1966.

A3-2. M. J. Ehrlich; "Slot-Antenna Arrays." Antenna Engineering Handbook, Henry Jasik, editor, 1961.

A3-3. W. C. Jakes, Jr.; "Horn Antennas." Antenna Engineering Handbook, Henry Jasik, editor, 1961.

A3-4. C. A. Mentzer and L. Peters, Jr.; "A Parametric Study of Cut-Off Corrugated Surface Properties." NASA CR-2317, October 1973.

A3-5. R. C. Hansen; Microwave Scanning Antennas. Vol. I, Academic Press, 1964.

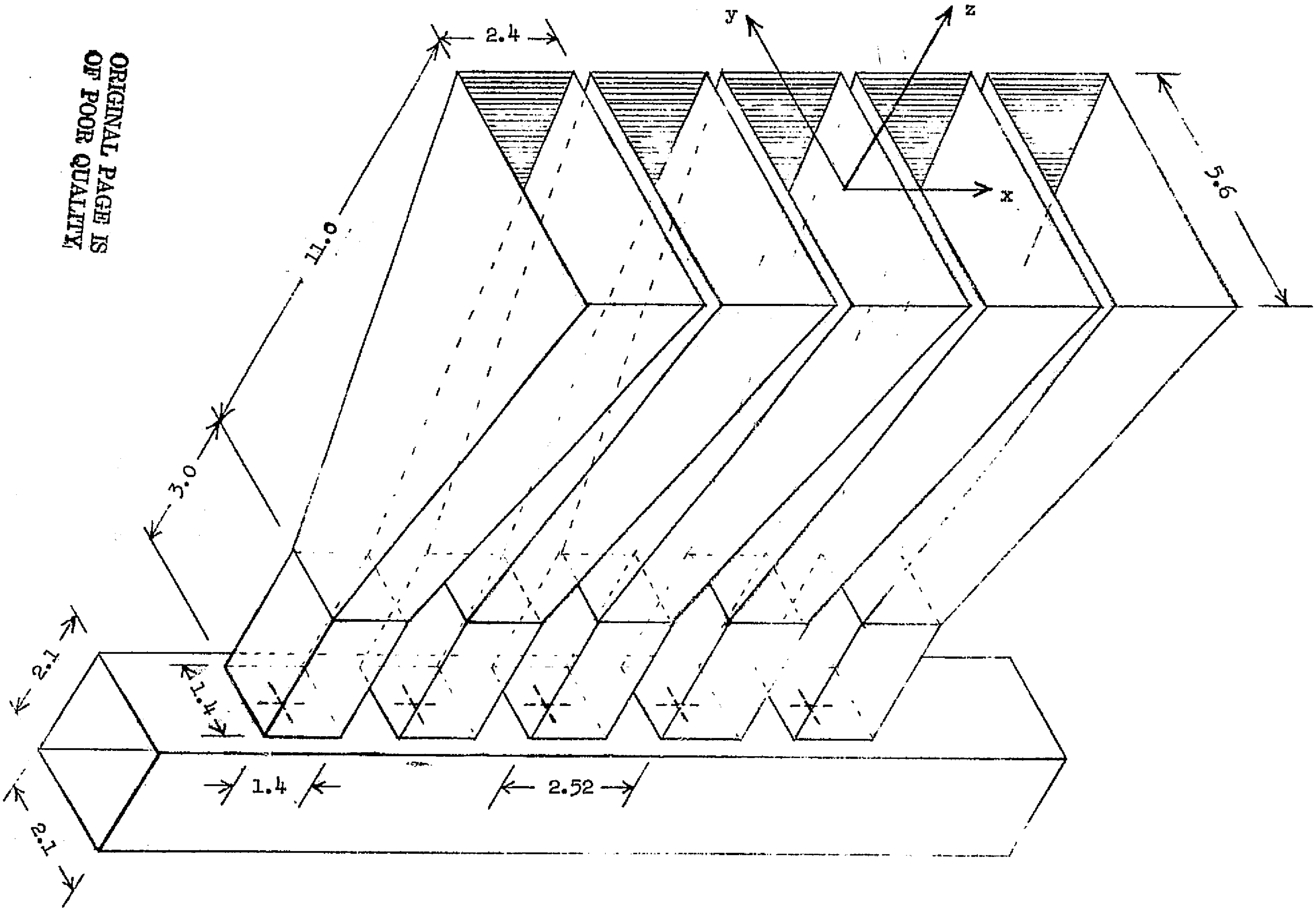

Figure A3-1. Corrugated pyramidal horn array. (dimensions in centimeters at 13.9 GHz)

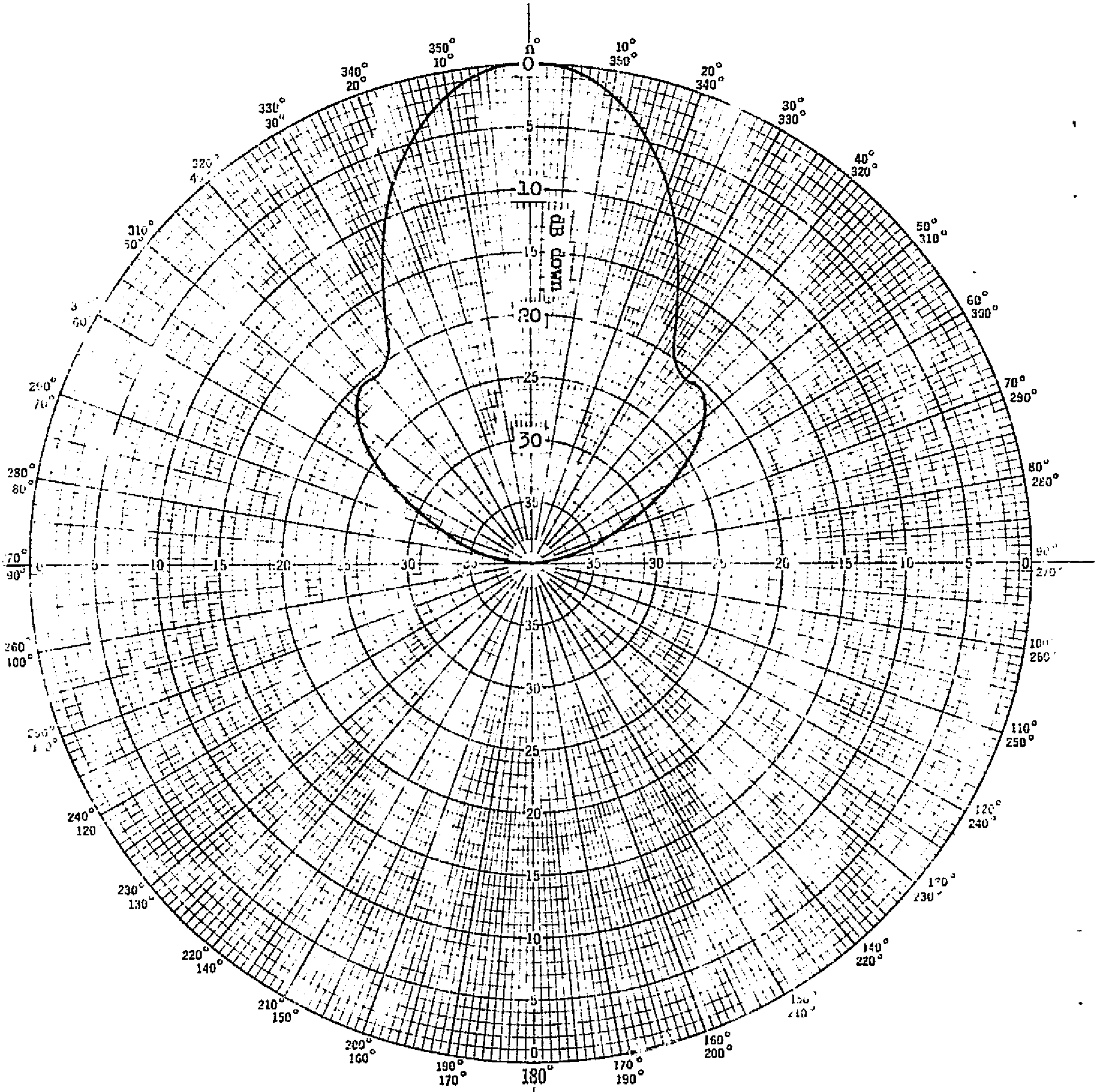

Figure A3-2. yz-plane radiation pattern of pyramidal horn array. (polarization in x-direction)

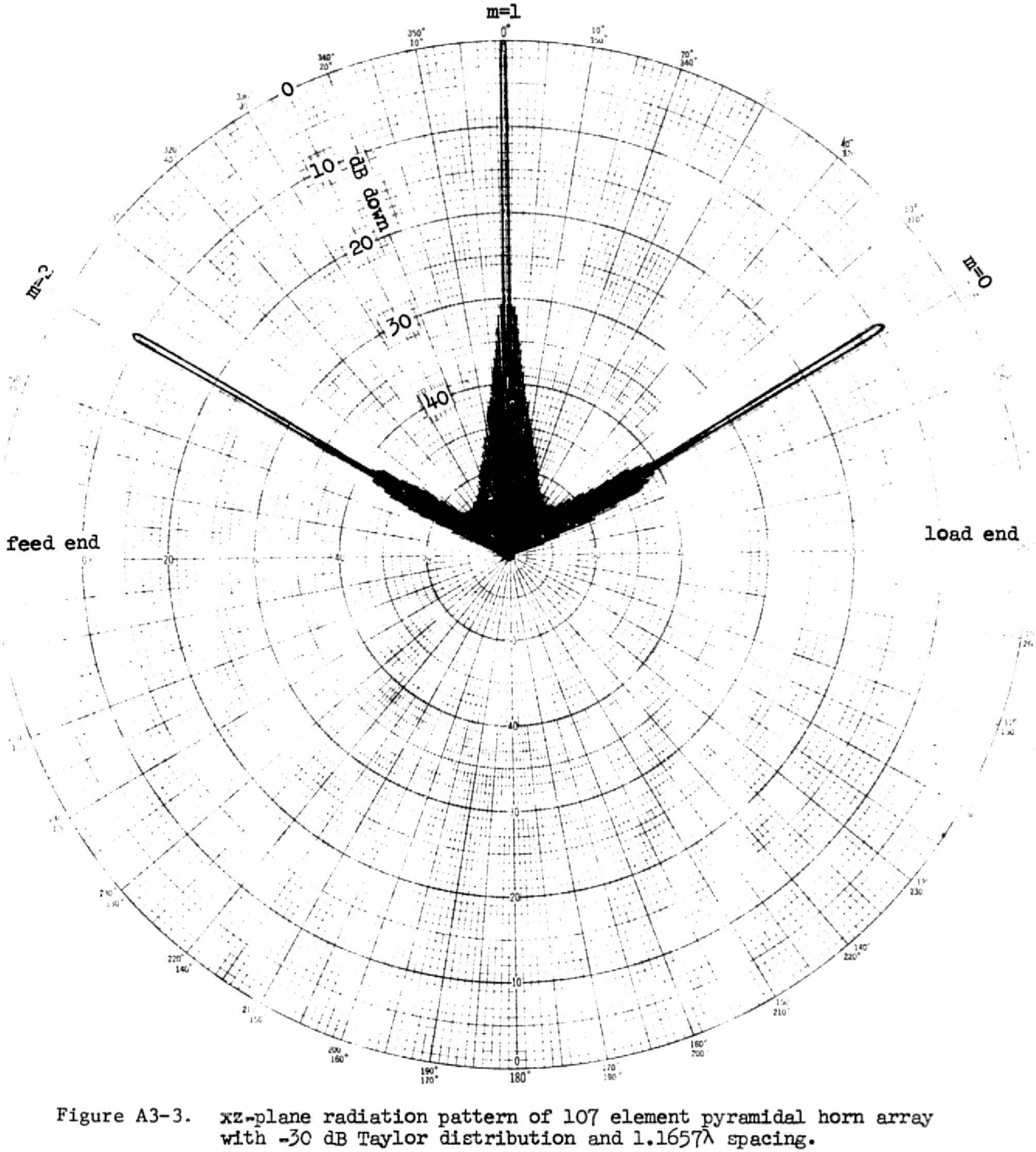

Figure A3-3. xz-plane radiation pattern of 107 element pyramidal horn array with -30 dB Taylor distribution and 1.1657λ spacing. (polarization in y-direction)

ORIGINAL PAGE IS
OF POOR QUALITY

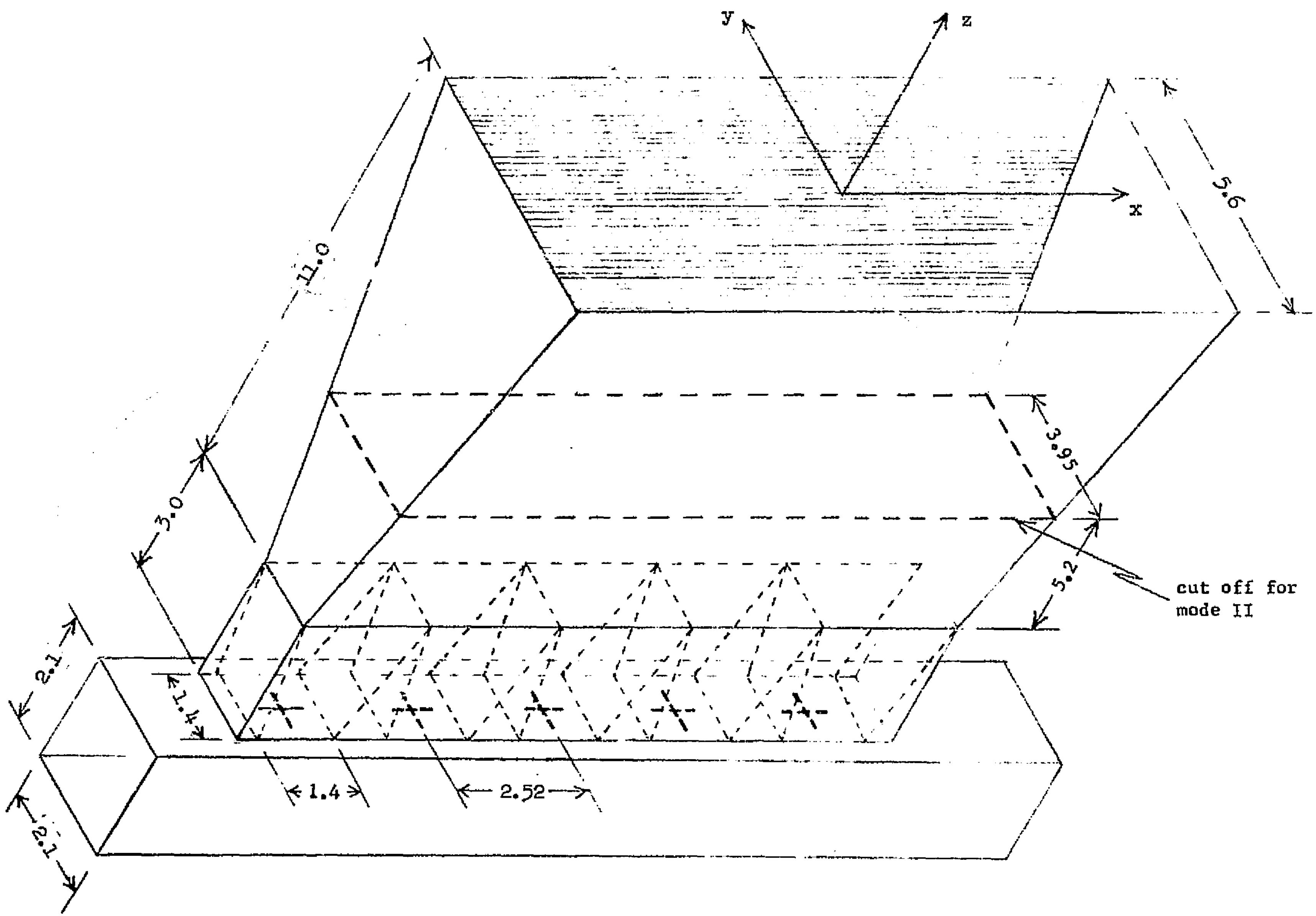

Figure A3-4. Corrugated trough antenna (dimensions in centimeters at 13.9 GHz)